

Index 35726 X
ISSN 0867-888X

POLISH
ACADEMY
OF SCIENCES
INSTITUTE
OF FUNDAMENTAL
TECHNOLOGICAL
RESEARCH

NATIONAL
ENGINEERING
SCHOOL
OF METZ

ENGINEERING TRANSACTIONS

ROZPRAWY INŻYNIERSKIE - TRAITE d'INGENIERIE



QUARTERLY
VOLUME 60
ISSUE 2

WARSZAWA - METZ 2012



Faster online
<http://et.ippt.pan.pl>

Contents of issue 2 vol. LX

- 101 M. DAIMARUYA, H. KOBAYASHI, *Impact behaviour of the Japanese sword*
- 113 T.J. BURNS, S.P. MATES, R.L. RHORER, E.P. WHITENTON, D. BASAK, *Modelling the peak cutting temperature during high-speed machining of AISI 1045 steel*
- 125 J. OSTROWSKA-MACIEJEWSKA, R.B. PECHERSKI, P. SZEPTYŃSKI, *Limit condition for anisotropic materials with asymmetric elastic range*
- 139 H.A. ATTIA, M.A.M. ABDEEN, *Velocity and temperature distributions between parallel porous plates with the Hall effect and variable properties under exponential decaying pressure gradient*
- 155 S. WOLNY, S. BADURA, *Stress analysis in structural components of the Koepe pulley in hoisting installations*
- 171 M. NISHIDA, H. ICHIHARA, H. WATANABE, N. FUKUDA, H. ITO, *Effect of dialkyl peroxide blending on tensile properties of PLA/PBAT polymer alloys*

ENGINEERING TRANSACTIONS **Founded 1952** **Appears since 1953**

Copyright ©2012 by Institute of Fundamental Technological Research
Polish Academy of Sciences, Warsaw, Poland

Aims and Scope

ENGINEERING TRANSACTIONS promotes research and practise in engineering science and provides a forum for interdisciplinary publications combining mechanics with material science, electronics (mechatronics), medical science and biotechnologies (biomechanics), environmental science, photonics, information technologies and other engineering applications. The Journal publishes original papers covering a broad area of research activities including experimental and hybrid techniques as well as analytical and numerical approaches. Engineering Transactions is a quarterly issued journal for researchers in academic and industrial communities.

INTERNATIONAL COMMITTEE

S. A. ASTAPCIK (<i>Byelorussia</i>)	P. PERZYNA (<i>Poland</i>)
A. CARPINTERI (<i>Italy</i>)	L. TOTH (<i>France</i>)
G. DOBMANN (<i>Germany</i>)	Z. WESOŁOWSKI (<i>Poland</i>)
T. IWAMOTO (<i>Japan</i>)	P. WOOD (<i>U.K.</i>)
A. N. KOUNADIS (<i>Greece</i>)	G. VOYIADJIS (<i>USA</i>)
J. LIN (<i>U.K.</i>)	R. ZAERA (<i>Spain</i>)
T. ŁODYGOWSKI (<i>Poland</i>)	

EDITORIAL COMMITTEE

R. PEÇHERSKI – Editor	A. RUSINEK – Co Editor
Z. AZARI	K. KOWALCZYK-GAJEWSKA
P. CHEVRIER	Z. KOWALEWSKI
B. GAMBIN	P. LIPIŃSKI
J. HOLNICKI-SZULC	K. KRIEGEL – assistant of the Co Editor

ENIM, 1 route d'Ars Laquenexy
57078 Metz Cedex 03
Phone: +33 3 87344266, E-mail: relinter@enim.fr

J. ŻYCHOWICZ-POKULNIEWICZ – secretary

Address of the Editorial Office:
Engineering Transactions
Institute of Fundamental Technological Research
Pawińskiego 5B, PL 02-106 Warsaw, Poland

Phone: (48-22) 826 12 81 ext. 206, Fax: (48-22) 826 98 15, E-mail: engtrans@ippt.pan.pl

Abstracted/indexed in:

Applied Mechanics Reviews, Current Mathematical Publications, Elsevier, EMBASE, Engineering Village, Inspec, Mathematical Reviews, MathSci, Reaxys, Scopus, Zentralblatt für Mathematik.

<http://et.ippt.pan.pl/>

Address of the Editorial Office:

Engineering Transactions
Institute of Fundamental Technological Research
Pawińskiego 5B
PL 02-106 Warsaw, Poland
Phone: (48-22) 826 12 81 ext. 206, Fax: (48-22) 826 98 15
E-mail: engtrans@ippt.pan.pl

SUBSCRIPTIONS

**Subscription orders for all journals edited by Institute of Fundamental Technological Research (IPPT) may be sent directly to the Publisher:
Institute of Fundamental Technological Research
e-mail: subscribe@ippt.pan.pl**

Please transfer the subscription fee to our bank account:
Payee: IPPT PAN
Bank: Pekao S.A. IV O/Warszawa
Account number 05124010531111000004426875.

WARUNKI PRENUMERATY

**Prenumeratę na wszystkie czasopisma wydawane przez Instytut Podstawowych Problemów Techniki PAN przyjmuje Dział Wydawnictw IPPT.
Bieżące numery Engineering Transactions można nabyć bezpośrednio w Redakcji:
ul. Pawińskiego 5B, 02-106 Warszawa
Tel.: (48-22) 826 60 22; Fax: (48-22) 826 98 15
e-mail: subscribe@ippt.pan.pl**

We would like to convey the words of appreciation and acknowledgement to Professor Pierre Padilla, who as the director of the National Engineering School of Metz – ENIM together with the director of the Institute of Fundamental Technological Research of the Polish Academy of Sciences in Warsaw, Professor Andrzej Nowicki signed agreement about the joint publishing since 2011 of the Quarterly Journal *ENGINEERING TRANSACTIONS (ROZPRAWY INŻYNIERSKIE – TRAITÉ d'INGENIERIE)*. We hardly observed that in February 2012 he is reaching the retirement age. We wish Professor Pierre Padilla good health and all happiness and do hope that we can still count on his advice and help in keeping our Quarterly founded in 1952 on a new path of its development. We consider this to be a milestone strengthening of the international position of the journal aiming at the publishing market of the European Research Area. We shall always remember that we owe this in great degree to the open mind, high spirit and persistence of Pierre Padilla.

Editorial Committee

Impact Behaviour of the Japanese Sword

Masashi DAIMARUYA¹⁾, Hidetoshi KOBAYASHI²⁾

¹⁾ *Muroran Institute of Technology*
27-1 Mizumoto, Hokkaido, 050-8585, Japan
e-mail: masashi@mmm.muroran-it.ac.jp

²⁾ *Graduate School of Engineering Science*
Osaka University
1-3 Machkaneyama, Toyonaka, Osaka, 560-8531, Japan
e-mail: hkoba@me.es.osaka-u.ac.jp

The Japanese sword is a weapon peculiar to Japan. The present study is concerned with the joint between *tohshin* (blade) and *tsuka* (hilt) of the Japanese sword. Only one *mekugi-take* (retaining peg made of bamboo) with about 5mm in diameter holds the tang in the hilt. However a slender *mekugi* might not be broken, even in the case of violent sword-fighting. This fact has been historically demonstrated in many battles by Japanese swords. In this study it is examined theoretically and experimentally from the viewpoint of impact engineering why a *mekugi* used in *Tachi* and *Katana* may not be broken. As a result, it is found that such a strong force as breaking a *mekugi-take* does not act on it, because of the location of *mekugi-ana* (a hole for *mekugi*) in the tang, which has been made in the Japanese sword by following the traditional code of sword-smiths.

Key words: impact force, impact response, Japanese sword, *Tachi*, joint of blade and hilt, *mekugi-ana*.

1. INTRODUCTION

The Japanese sword is a weapon peculiar to Japan. What we call the *Nip-pontoh* (the Japanese sword) includes various forms of blades such as *Ken*, *Naginata* and *Yari* in addition to the more common *Tachi*, *Katana*, *Wakizashi* and *Tantoh*. These swords except *Ken* and *Yari* are single-edged weapons for slashing, cutting and stabbing. The Japanese sword must fulfill the three functional requirements of not breaking, not bending and cutting well, as well as being an aesthetic work of craftsmanship. The *sugata* and *sori* (graceful shape and curve), the changes in the *jihada* (blade surface) and *hamon* (temper patterns) of the Japanese sword make it a work of art. In the past, the Japanese sword was valued for its utility as a weapon, but nowadays it is an artwork of typical traditional crafts in Japan [1–5].

The Japanese sword is interesting not only from the viewpoint of traditional crafts of arts, but also from the aspect of modern science and technology because the way of making and its functionality in weapon are really consistent with science [6–8]. The present study is concerned with the joint between *tohshin* (blade) and *tsuka* (hilt) of the sword. Only one *mekugi-take* (retaining peg made of bamboo) with about 5 mm in diameter holds the tang in the hilt. However the slender *mekugi* might not be broken, even in the case of severe sword-fighting. This fact has been historically demonstrated in many battles by Japanese swords.

So far we have examined it with models of the Japanese sword [9, 10]. In this study, it is investigated with an actual *Tachi* theoretically and experimentally from the viewpoint of impact engineering why a *mekugi* used in Japanese swords may not be broken even in the violent sword-fighting.

2. TACHI AND KATANA IN THE JAPANESE SWORD

There are *Tachi*, *Katana*, *Wakizashi*, *Tantoh*, *Ken*, *Naginata* and *Yari* in the Japanese sword. Classification of the blade in the Japanese sword is depicted in Fig. 1. From the Heian period (11th century) through the early part of the Muromachi period (14th century), *Tachi* was worn slung from the waist with edge-side downwards. *Tachi* usually have a high curvature (*sori*), and the length of blade is more than 60.6 cm (2 *syaku*), usually 65–80 cm. Here, *syaku* is an old Japanese unit to measure length. *Katana* came into widespread use in the middle of the Muromachi period (15th century) and was in use until the very end of the Edo period (19th century). *Katana* is 60.6 cm long or more, but usually somewhat shorter than *Tachi*. In contrast to *Tachi*, *Katana* is worn thrust edge upwards through the belt. Swords in length between 30.3 cm (1 *syaku*) and

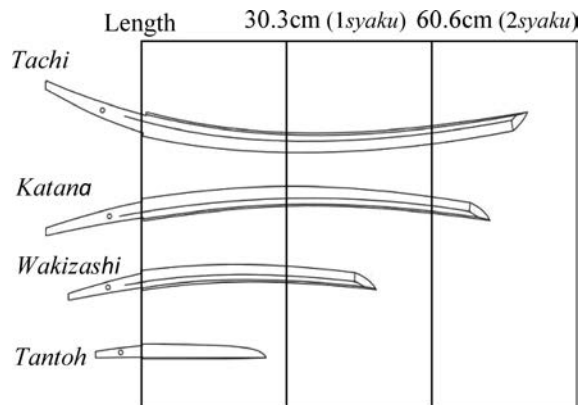


FIG. 1. Classification of the Japanese sword.

60.6 cm are called *Wakizashi*, and was worn on the waist like *Katana*. During the Edo period, a *wakizashi* was worn with a *katana* as a *dai-sho* (a pair of large and small swords). Swords shorter than 30.3 cm are called *Tantoh*.

It is said that the curved and ridged blade familiar to us as *shinogi-zukuri tachi* came into existence in the middle of the Heian period (11th century). The cross section of *shinogi-zukuri* blade is illustrated in Fig. 2. A bar of core steel (*shingane*) with low carbon content wrapped by hard skin steel (*kawagane* and *hagane*) with high carbon content goes through the forging process. This process is called *tsukurikomi*, and the combination of two or three kinds of different steels with different carbon content produces the characteristic of the Japanese sword. Thus such a combination of different kinds of steel results in the nonuniform distribution of carbon in the cross section and this duplex structure gives the sword high strength, toughness and ductility. After rough shaping, the sword is transferred to the final process of quenching or hardening (*yakiire*). Before *yakiire*, a kind of clay (*yakiba-tsuchi*) is coated on the surface of the blade to control the heat transfer intensity. The coated clay is thick on the ridge while thin on the edge part. During the quenching process, the regions near the cutting edge are transformed from unstable austenite to martensite, while other regions remain pearlite and ferrite structure. Consequently, temper patterns (*hamon*) appear at the border of those parts, and the graceful curved shape peculiar to the Japanese sword is generated at the same time.

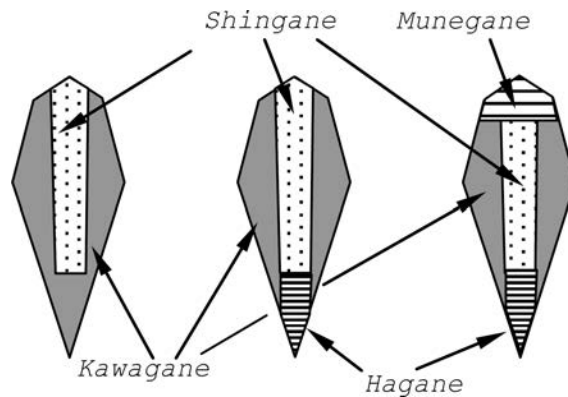


FIG. 2. Tukurikomi: a) *Koubuse*, b) *Honsannmai*, c) *Shihouzume*.

The traditional mounting of the Japanese sword for practical use is called *koshirae*. *Koshirae* consist of a lacquered wooden scabbard, a wrapped and braided hilt, sword guard and other decorative metal fittings. Figure 3 shows a dismantled Japanese sword of *koshirae*. Only one *mekugi-take* (retaining peg made of bamboo) with about 5 mm in diameter holds the tang in the hilt, therefore the Japanese sword with *koshirae* is easily dismantled by merely pulled out



FIG. 3. Parts of the Japanese sword.

a *mekugi-take*. Considering that the swords were used in the battle of violent sword-fighting, this simply traditional technique is astonishing from the viewpoint of assembly technology.

3. IMPACT BEHAVIOUR OF TACHI BLADE

Figure 4 shows a *tachi* used in the present study: a) a *tachi* with *koshirae*, b) dismantled parts, and c) a *tachi* blade. The blade is 700 mm (*2syaku 3zunn*) long with 19.5 mm (*7bu*) of curvature (*sori*). For the sake of safety in experiments, the sharp edge of the blade is dulled such as the thickness of edge end approximately 0.2 mm. Main dimensions of the *tachi* blade are shown in Fig. 5.

FIG. 4. *Tachi* used for impact experiment and numerical simulation.

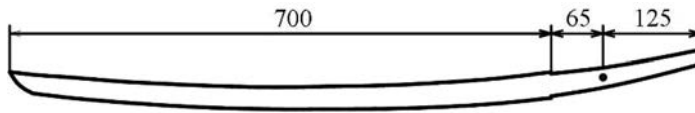


FIG. 5. Dimensions of *Tachi* blade.

In the actual sword-fighting the sword is supposed to be subjected to various impact forces at different positions of the blade. The schematic of experiments performed in this study is shown in Fig. 6. A *tachi* blade hung vertically by cotton string from a frame is subjected to an impact force by a copper striking bar (1000 mm in length and 10 mm in diameter). The impact force incident to the sword and the variation of displacement with time at each location along the axis of a blade are measured.

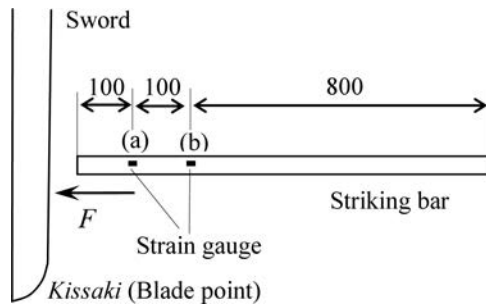


FIG. 6. *Tachi* blade subjected to impact force by a striking bar.

The incident forces measured in experiments are shown in Fig. 7 by solid and broken curves, which were obtained by impacting the striker with an impact velocity of 2.6 m/s to the position of 100 mm and 350 mm from *kissaki* (blade

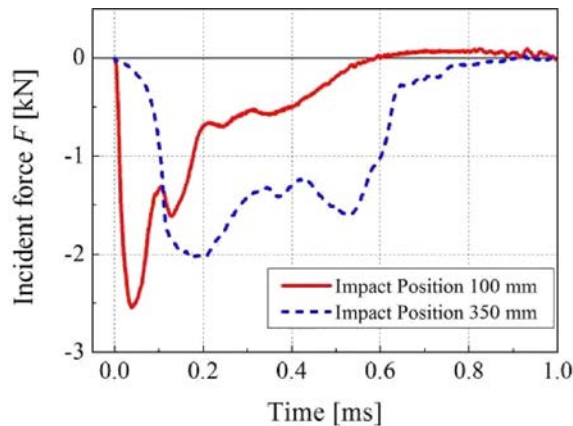


FIG. 7. Incident forces into *Tachi* blade.

point) of the blade, respectively. The diagrams of force vs. time were given by a measuring method using two strain gauges, which makes it possible to eliminate the effect of reflect waves from the opposite free end of a striker [11]. The waves of two incident forces are different from each other due to the impacted position.

On the other hand, the fluctuation of displacement with time at each location along the axis of the blade was measured by making use of a CCD laser displacement sensor (KEYENCE, LK-G155). Figure 8a and b show the variations

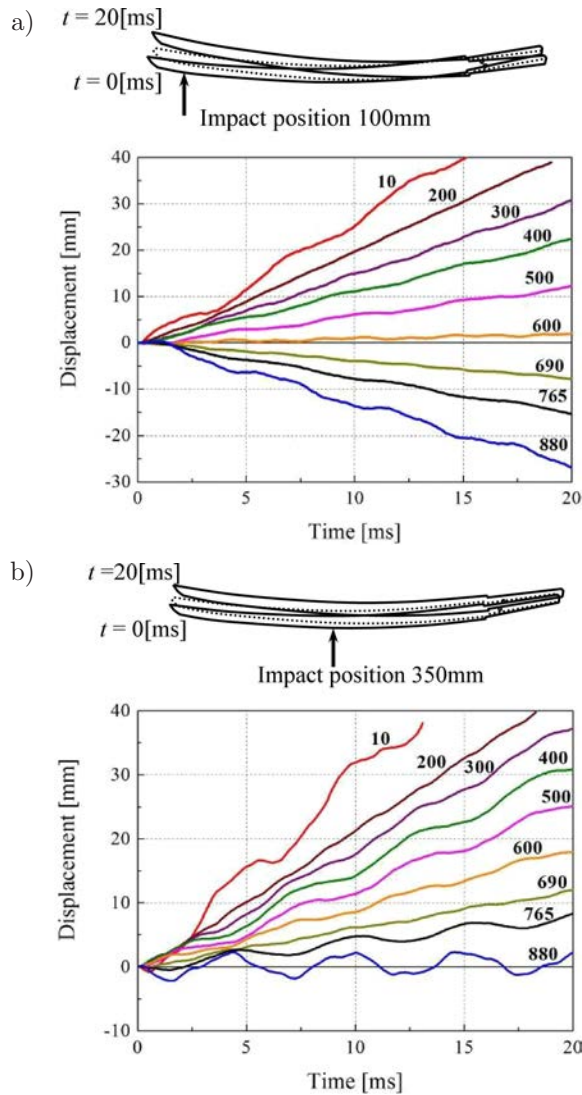


FIG. 8. Variation of displacement with time at each location: a) impact position of 100 mm from *Kissaki*, b) impact position of 350 mm from *Kissaki*.

of the displacement with time, including the rigid body displacement, when the impact forces shown in Fig. 7 were applied on each position of 100 mm and 350 mm from *kissaki* of the blade, respectively. The numerical value on each curve indicates a distance from *kissaki*. In addition the whole movement of the blade is illustrated above the figures.

By taking off the rigid body displacements from those displacement curves, the oscillation curves were obtained. Figure 9a and b show the oscillation of the displacement at the location of 10 mm, 765 mm, and 880 mm from *kissaki*, which correspond to the vicinity of *kissaki*, the location of *mekugi-ana*, and the vicinity of *nakago-jiri* (the end of the tang), respectively. In both cases of the impacted positions of 100 mm and 350 mm, the displacement amplitude at the

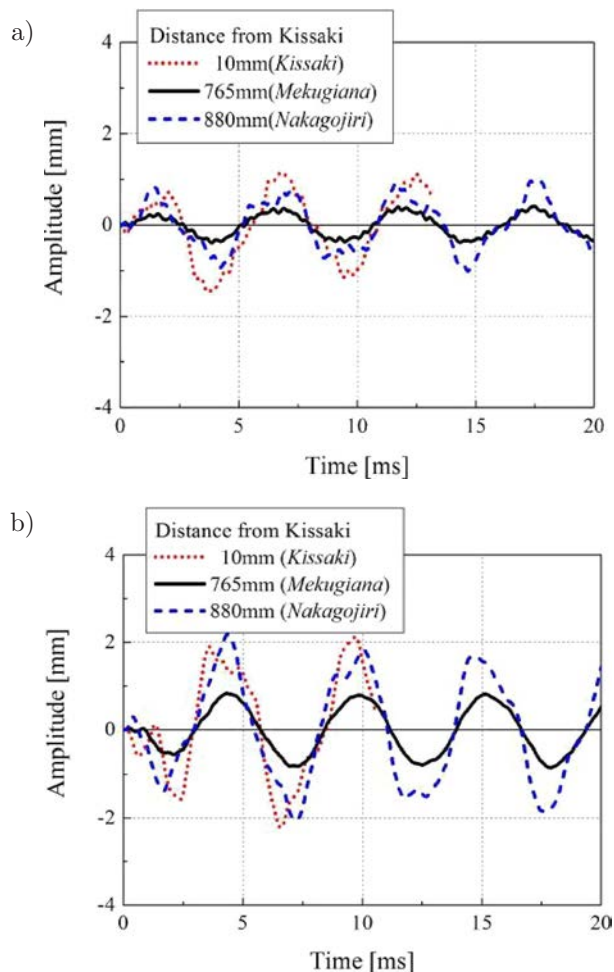


FIG. 9. Oscillation of displacement at each position: a) impact position of 100 mm from *Kissaki*, b) impact position of 350 mm from *Kissaki*.

location of *mekugi-ana* becomes small compared to one at other locations. The amplitude at each location of the blade is presented in Fig. 10 for both cases of the impacted positions of 100 mm and 350 mm. It can be seen that the distribution of the displacement amplitude along the axis of a blade is similar in spite of the differences of the impact position and the incident force. The amplitude at the vicinity of *kissaki* and *nakago-jiri* is large, but it becomes comparatively small at the neighborhood of *machi* (notch on the boundary between the blade and the tang).

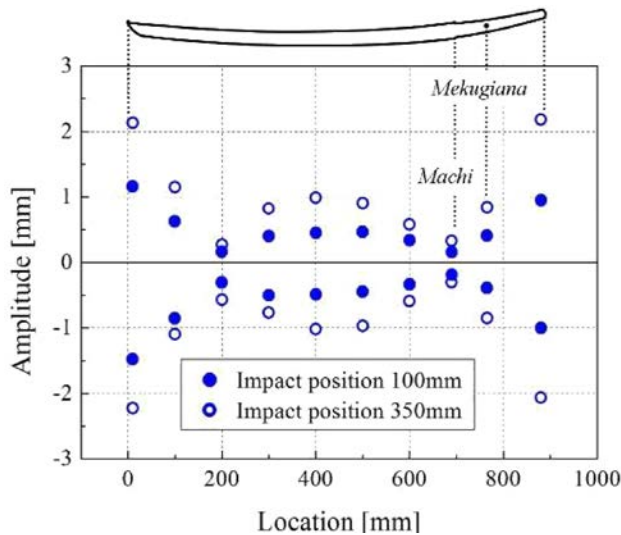


FIG. 10. Distribution of amplitudes for impact positions of 100 mm and 350 mm from *Kissaki*.

Numerical simulations were also carried out, based on the incident forces given in Fig. 7. As was stated previously, the structure of a sword blade is heterogeneous and composite. However, the velocity of elastic stress waves is determined only by elastic modulus E , density ρ and Poisson's ratio ν , and the difference in these elastic values of ferric materials is small. Therefore, a series of numerical simulations for a sword model made of a single material with $E = 206$ GPa, $\rho = 7.85 \cdot 10^3$ kg/m³ and $\nu = 0.29$, were carried out by using a code of LS-DYNA.

A three-dimensional finite element mesh division of the sword is represented in Fig. 11, where the division is made for a half-part in the width direction due to symmetry. Figures 11a and 11b respectively denote the whole region and the enlarged part near the blade tip (*Kissaki*) and the tang (*Nakago*). The total number of the elements used in the model is 8,916, and that of the nodes is 12,600.

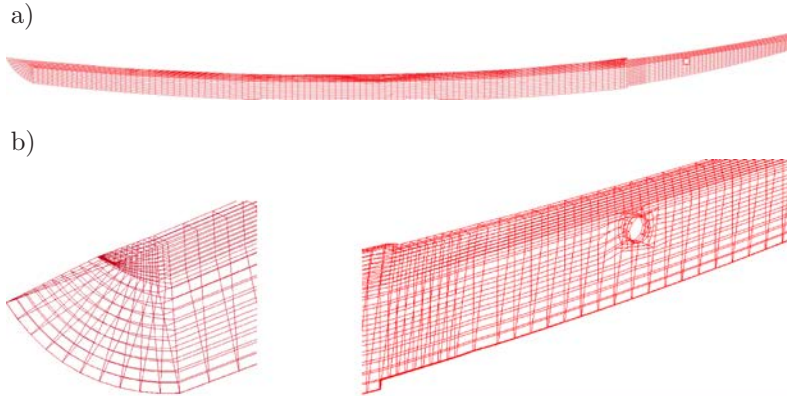


FIG. 11. Finite element division of the sword: a) whole region, b) near the blade tip and *Mekugi-ana* in the tang.

Figure 12 shows the comparison between the experimental results (circles) and the numerical results (curves) concerning the displacement amplitude at each location of a *tachi* blade. The numerical results show good agreement with the experimental ones.

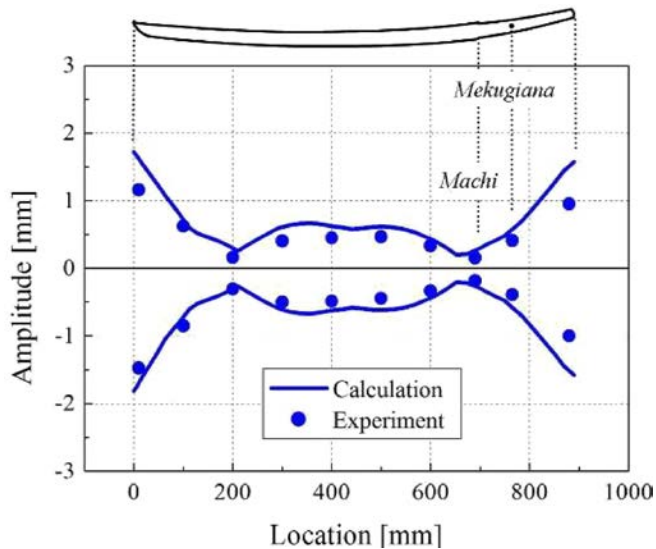


FIG. 12. Comparison between the measured and simulated amplitudes (impact position of 100 mm).

If a *mekugi-take* is not easily broken even in the severe sword-fighting, it seems reasonable that the amplitude would have a certain minimum value just at the location of *mekugi-ana*. However, as seen in Figs. 10 and 12, the minimum

amplitude is at the neighborhood of *machi*. This may be by reason of only a blade, that is, a *tachi* without *koshirae*. Therefore in order to inspect the effect of *koshirae* such as *tsuka* (hilt), *tsuba* (sword guard) and other metal fittings on the displacement amplitudes, a *tachi* with *koshirae* was also examined in the same manner.

4. TACHI WITH KOSHIRAE

Figure 13 shows a *tachi* with *koshirae*, which is the traditional mounting of the Japanese sword for practical use, and consist of a lacquered wooden scabbard, a wrapped and braided hilt, a sword guard and other metal fittings such as a *habaki* and a pair of *seppa*.

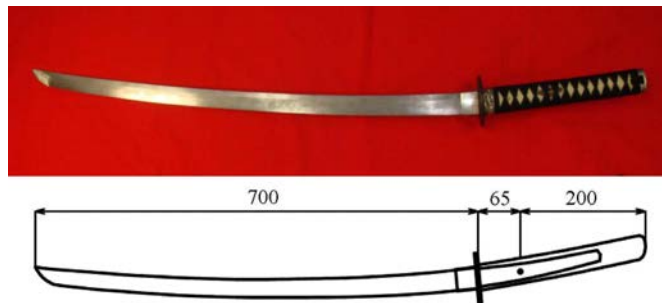


FIG. 13. *Tachi* with *koshirae*, and dimensions.

Figure 14a shows the variation of the displacement with time at each location of a *tachi* with *koshirae*, which is subjected to an impact force at the position of 10 cm from *kissaki* by a striker bar. The numerical value on each curve indicates a distance from *kissaki*. Then by subtracting the rigid body displacement from those displacement curves, the oscillation curves at the locations of *kissaki*, *mekugiana* and *tsuka-gashira* (the end of the hilt) of the *tachi* with *koshirae* were obtained as shown in Fig. 14b.

Based on those results, the distribution of the amplitude at each location of the *tachi* with *koshirae* was obtained as shown by solid circles in Fig. 15. In order to compare the case of the *tachi* blade to the case of the *tachi* with *koshirae*, the results on the blade presented in Fig. 10 are plotted by open circles in addition. It can be seen that the displacement amplitude for the *tachi* with *koshirae* becomes to the minimum just at the location of a *mekugi-ana*, while the minimum amplitude for the case of only a blade stands at the vicinity of *machi*.

The position of a *mekugi-ana* (a hole for *mekugi*) has been determined by following the individual traditional code of sword-smiths in the Gokaden (the five traditions of sword making) and their schools. It is found from the present study, in which a Bizen style blade was employed, that such strong forces as

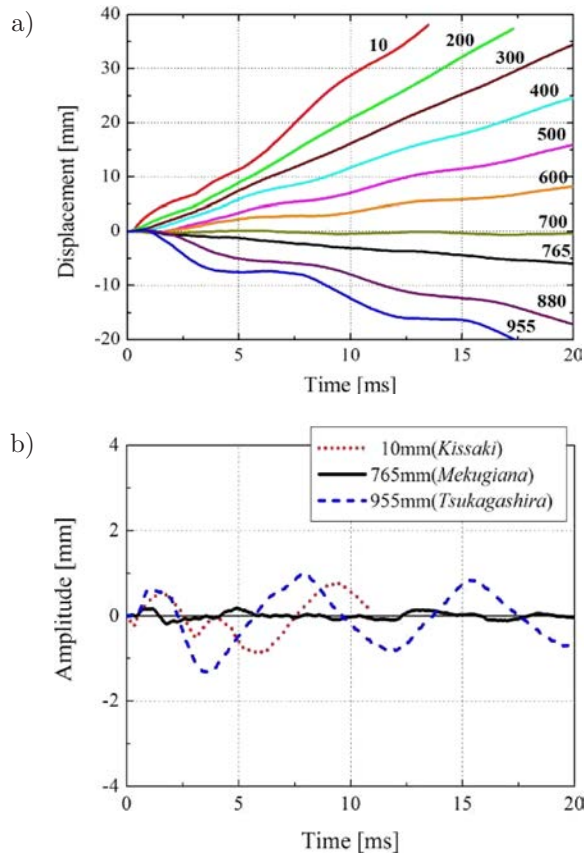


FIG. 14. Impact responses of *Tachi* with *koshirae*: a) variation of displacement with time at each location, b) oscillation of displacement.

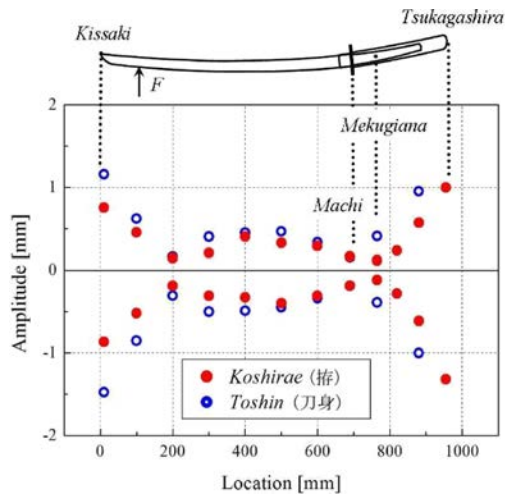


FIG. 15. Comparison of amplitudes for *Toshin* (*tachi* blade) and *Tachi* with *koshirae*.

breaking a *mekugi-take* would not act on it in the Japanese sword made by the traditional code of sword-smiths.

5. CONCLUDING REMARKS

In this study it is examined with an actual *tachi* from the viewpoint of impact engineering why a *mekugi* used in Japanese swords may not be broken even in the violent sword-fighting. As a result, it is found in the *tachi* with *koshirae* (practical mounting) that such a strong force as breaking a *mekugi-take* would not act on it, by reason of the location of *mekugi-ana* (a hole for *mekugi*) in the tang, which has been made in the Japanese sword by following the traditional code of sword-smiths.

REFERENCES

1. SATO K., *The Japanese Sword – A Comprehensive guide*, Kodansha International, Tokyo, 1983.
2. KAPP L., KAPP H., YOSHIHARA Y., *The Craft of the Japanese Sword*, Kodansha International, Tokyo, 1987.
3. SUZUKI T., *Traditional Technology of Making Japanese Swords* [in Japanese], Rikougakusya, 1994.
4. DODD B., The Making of Old Japanese Swords, *Journal of Mechanical Working Technology*, **2**, 75–84, 1978.
5. The Society for Preservation of Japanese Art Swords; <http://www.touken.or.jp/>
6. FUJIWARA H., HANABUSA T., TANAKA K., *Scientific research of Japanese sword – its curvature (sori) and residual stresses*, Proc. 3rd Inter. Conf. Residual Stresses, **2**, 1537–1542, 1991.
7. INOUE T., UEHARA T., NAKANO Y., *Metallo-Thermo-Mechanical Simulation of Quenching and Tempering of Japanese Sword*, Proc. of 5th Inter. Symposium on Plasticity and its Current Applications, July 17–21, 1995, Sakai-Osaka, pp. 697–700.
8. INOUE T., *The Japanese Sword – Materials, Forging and Simulation of Quenching* [in Japanese], *Materia Japan*, **35**, 2, 174–178, 1996.
9. DAIMARUYA M., *Impact Response of the Japanese Sword Model* [in Japanese], *Inspection Engineering*, **11**, 5, 12–16, 2006.
10. DAIMARUYA M., KOBAYASHI H., FUJIKI H., *Impact Response of a Model of the Japanese Sword with Sori* [in Japanese], Proc. of 2006 Annual Meeting of JSME/MMD, pp. 149–150, 2006.
11. DAIMARUYA M., KOBAYASHI H. BUSTAMI S., CHIBA M., *Impact Tensile Strength and Fracture of Plaster Material*, *J. Japan Soc. Str. Fracture Mats.*, **30**, 1, 1–24, 1996.

Received January 31, 2011; revised version December 14, 2011.

Modelling the Peak Cutting Temperature During High-Speed Machining of AISI 1045 Steel

Timothy J. BURNS¹⁾, Steven P. MATES²⁾, Richard L. RHORER³⁾,
Eric P. WHITENTON³⁾, Debasis BASAK⁴⁾

National Institute of Standards and Technology

¹⁾ *Information Technology Laboratory*

²⁾ *Material Measurement Laboratory*

³⁾ *Engineering Laboratory*

100 Bureau Drive, Gaithersburg, Maryland 20899, USA
e-mail: timothy.burns@nist.gov

⁴⁾ *Orbital Sciences Corporation*

21839 Atlantic Blvd., Dulles, Virginia 20166, USA

This paper presents new experimental data on AISI 1045 steel from the NIST pulse-heated Kolsky Bar Laboratory. The material is shown to exhibit a stiffer response to compressive loading when it has been rapidly preheated, than it does when it has been heated using a slower preheating method, to a testing temperature that is below the eutectoid temperature. It is argued, using a simple model for heat generation in the workpiece and the tool during machining, due to Tlustý, that this work has important implications for the modelling of high-speed machining operations. Based on the experimental data, a modification is recommended of the well-known Johnson-Cook constitutive model of Jaspers and Dautzenberg for this material, in order to achieve improved predictions of the peak cutting temperature in machining.

Key words: high-speed machining, thermal modelling, AISI 1045 steel, Kolsky bar.

1. INTRODUCTION

High-speed machining processes can cause extremely rapid plastic deformation and heating of the work material. If this material is a carbon steel, a small region of thickness on the order of 10 μm is deformed plastically in the primary shear zone, to a strain on the order of 100%, at a strain rate on the order of 10,000 s^{-1} , on a time interval on the order of 10 μs . Subsequently, the material is subjected to additional large plastic strain in the secondary shear zone for a time on the order of 1 ms. During this small cutting time, the work material undergoes a change in temperature on the order of magnitude

of 1000°C. Thus, a heating rate on the order of one million degrees Celsius per second is not uncommon for iron-carbon alloys of interest in manufacturing (see, e.g., [13]). Under such extreme conditions, there can be insufficient time for thermally-activated processes, such as solid-solid phase transformations, dislocation annealing, and grain growth, to produce changes in the microstructure of the material that occur on significantly longer time scales; see e.g., [11]. This means that unique non-equilibrium superheated microstructural states can be present during high-speed machining operations, with the result that the material flow stress can differ significantly from that which is measured under equilibrium high-temperature conditions. This poses a major challenge for modelling the constitutive response of these materials for use in finite-element simulations of rapid machining operations; see, e.g., [5]. The focus of this paper is on the measurement and modelling of the constitutive response of AISI 1045 steel, for use in the study of high-speed machining operations, and in particular, for finite-element analysis (FEA) simulations of these processes, because this approach is gaining wide use among both academic researchers and manufacturers.

In the thesis of JASPERS [8], a systematic effort was made, for a number of metals of interest in manufacturing, first to identify the conditions of the workpiece material during a high-speed metal cutting operation, and second to develop material testing methods that could reproduce these conditions as closely as possible. A result of this work was the publication of what is arguably the most often used constitutive model for AISI 1045 steel [9], a five-parameter phenomenological JOHNSON-COOK model [10]. In the same paper, a six-parameter Zerilli-Armstrong model for the material was also published. Even though Jaspers concluded that this model provided a better fit to the experimental data than did the Johnson-Cook model, and even though the Zerilli-Armstrong model is better motivated from a scientific point of view, this model is mathematically more complicated than the Johnson-Cook model, and it is harder to fit experimentally. As a result, it is less widely available and less widely used in FEA simulations of machining processes. For these reasons, and for reasons that will become clear in what follows, attention in this paper will be focused on the Johnson-Cook model for AISI 1045,

$$(1.1) \quad \bar{\sigma}(\bar{\epsilon}, \dot{\bar{\epsilon}}, T) = (A + B\bar{\epsilon}^n) (1 + C \ln \dot{\bar{\epsilon}}) (1 - T^{*m}),$$

where the effective true stress is expressed as a simple product of functions of the effective true strain, strain rate, and temperature, respectively. The homologous temperature T^* is given by the nondimensional formula $T^* = (T - T_r)/(T_f - T_r)$, where T is the temperature of the material in degrees Celsius, $T_r = 20^\circ\text{C}$ is the reference temperature, and $T_f = 1490^\circ\text{C}$ is the melting temperature of the

material. The parameters that were determined in [8, 9] for AISI 1045 are as follows:

$$(1.2) \quad \begin{aligned} A &= 553.1 \text{ MPa}, & B &= 600.8 \text{ MPa}, & C &= 0.0134, \\ n &= 0.234, & m &= 1.0. \end{aligned}$$

In this paper, new experimental data are presented on AISI 1045 steel from the NIST pulse-heated Kolsky Bar Laboratory [12]. It is shown that, when the material has been preheated to a temperature that is below the eutectoid temperature (723°C), it exhibits a stiffer response to compressive loading when it has been rapidly preheated, i.e., heated to a uniform temperature in a few seconds, than it does when it has been preheated using a slower method, as was done in the thesis work of JASPERS [8]. It is argued, using a simple model for heat generation in machining due to TLUSTY [13], that this work has important implications for the modelling of high-speed machining operations. Based upon this work, a modification is recommended of the well-known Johnson-Cook constitutive model of JASPERS and DAUTZENBERG [9] for this material, in order to achieve improved predictions of the peak cutting temperature in finite-element analysis simulations of high-speed metal cutting operations.

In the next section, a brief review is given of some thermal imaging data that were taken during continuous chip formation in some steady-state orthogonal cutting experiments. Following this, a brief discussion is provided of Tlusty's model. The fourth section presents some relevant NIST pulse-heated Kolsky bar data to provide a possible explanation for why the Jaspers and Dautzenberg models underpredicted the temperature in the machining simulations. The final section uses these data to discuss a possible modification of the Johnson-Cook model for application to high-speed machining processes, along with some discussion and conclusions.

2. REVIEW OF ANALYTICAL AND EXPERIMENTAL TOOL-CHIP INTERFACE TEMPERATURE RESULTS

In a series of steady-state orthogonal cutting experiments on AISI 1045 steel that were performed at NIST [6], the temperature field along the tool-chip interface was measured under conditions of continuous chip formation. In four sets of these experiments, all of the cutting parameters were kept the same, except for the uncut chip thickness; see Table 1. Assuming conditions of plane strain and material incompressibility, the chip velocity was calculated, and then the net thermal flux Φ that exited a control volume surrounding the cutting region was estimated for each of the four sets of experiments. Assuming the net thermal energy flux was equal to the total mechanical power led to an estimate for the specific cutting energy K_s in the system,

$$(2.1) \quad \Phi = F_c v_c = K_s h b v_c.$$

Here, F_c is the cutting force, $v_c = 3.7$ m/s is the cutting speed, and $b = 1.5$ mm is the chip width. For the four different uncut chip thicknesses, $h = 23$ mm, $h = 31$ mm, $h = 40$ mm, and $h = 48$ mm, it was found that the specific cutting energy was nearly constant, with $K_s \approx 2400$ N/mm².

Table 1. Data from four sets of orthogonal cutting experiments; h and h_c are, respectively, the uncut and cut chip thicknesses, b is the chip width, and v_c is the cutting speed.

No	h [μm]	h_c [μm]	b [mm]	v_c [m/s]
1	48	160	1.5	3.7
2	40	145	1.5	3.7
3	31	125	1.5	3.7
4	23	100	1.5	3.7

In the same study, a transient advection-diffusion model for the temperature distribution in orthogonal metal cutting, which was originally developed by BOOTHROYD [2], and subsequently improved upon by TLUSTY [13], was used to calculate the temperature field in the chip and in the tool for the same four sets of orthogonal cutting parameters, using a finite-difference numerical method. The stress in this model is determined directly from the specific cutting energy, and it does not depend upon the temperature. The model allowed for heat transport into both the tool material and uncut workpiece material. While these comparatively simple finite-difference calculations did not accurately reproduce the temperature contours measured in the cutting experiments, they gave remarkably good predictions of the peak temperature along the tool-chip interface; see Fig. 1.

In a subsequent study [7], the commercial finite-element software package ABAQUS [1] was used to model the temperature in these experiments. Using both the Johnson-Cook and the Zerilli-Armstrong material response models for AISI 1045 that had been developed specifically for computer simulations of metal-cutting operations by Jaspers (see [9]), it was found that the simulations underpredicted the peak tool-chip interface temperature by hundreds of degrees Celsius; see Fig. 2.

The comparisons of the finite-difference and finite-element analysis results with the experimental data support the hypothesis that there is insufficient time for thermal softening mechanisms to have much effect on the work material in the cutting region during high-speed machining, so that the material has a stiffer response than is predicted using standard constitutive models. In the present study, suggestions are made as to how to modify the Johnson-Cook constitutive model to achieve improved temperature predictions.

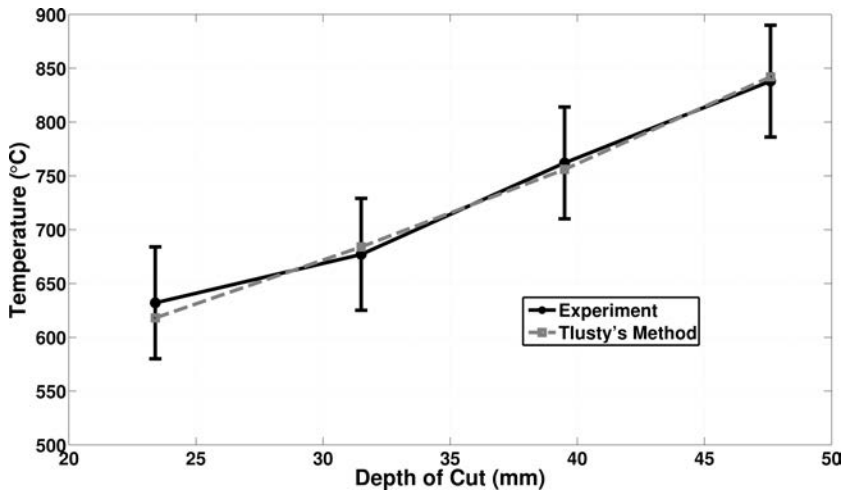


FIG. 1. Experimentally measured peak tool-chip interface temperatures compared with predictions of these temperatures using Tlusty's method; error bars denote an overall uncertainty (2σ) of $\pm 52^\circ\text{C}$ in the data [6].

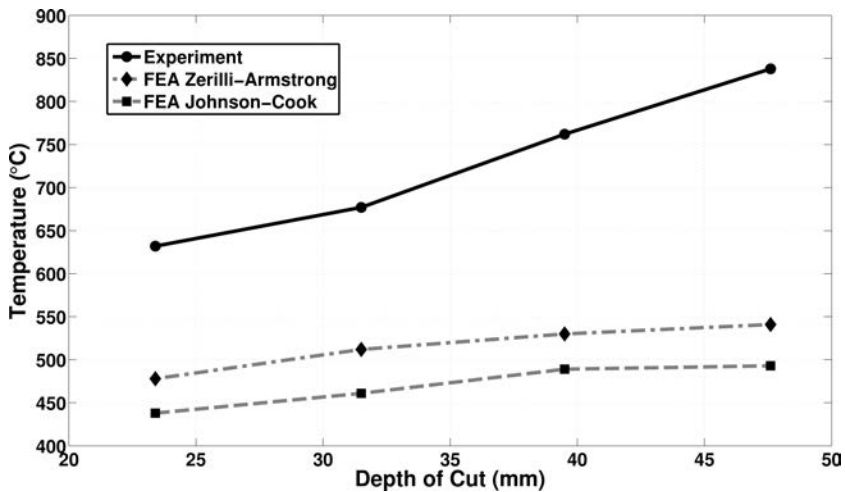


FIG. 2. Experimentally measured peak tool-chip interface temperatures compared with predictions of these temperatures by means of finite-element analysis.

3. TLUSTY'S ADVECTION-DIFFUSION MODEL

The finite-difference model for the tool-work material interface temperature, as presented by TLUSTY [13], assumes that there are two heat sources, and that heat is transported by conduction in the direction normal to the tool-chip interface, and by mass transfer along with the work material in the direction of chip flow along the tool face. The first source of heating is represented by the

shearing power, P_s , which arises from rapid dissipation by plastic deformation in the primary shear zone; this zone is modelled as a planar surface. This surface is assumed to be at a constant, uniform temperature, T_s . This temperature can be calculated using the following expression,

$$(3.1) \quad hbv_c\rho c(T_s - T_r) = P_s = F_s v_s.$$

Here, h and b are the depth of cut and chip width, respectively, as already specified in the preceding section; v_c is the cutting speed; $\rho = 7800 \text{ kg/m}^3$ and $c = 474 \text{ J/(kg-K)}$ are, respectively, the density and specific heat of the workpiece material; $T_r = 20^\circ\text{C}$ is the reference temperature; F_s is the shearing force; and v_s is the shearing speed. The second source is the friction power, P_f , which is generated by friction along the chip-tool interface in the secondary shear zone, which is also modelled as a planar surface. The model for P_f is based on experimental tool pressure measurements [4]. Assuming that the orthogonal cutting parameters are known, including the friction angle β , the friction power P_f can be determined once F_s is known. Following TLUSTY [13], in [6] it was assumed that the friction angle $\beta = 16.7^\circ$ (i.e., $\tan\beta = 0.3$). Thus, Thusty's model predicts the tool-chip interface temperature by using the conditions on the primary shear plane, together with a model for the pressure along the tool chip interface. Furthermore, Thusty's model predicts a shear plane temperature of approximately 600°C in AISI 1045 steel, and to a first approximation, this is independent of h , b , and v_c .

Now, suppose that the specific cutting energy for the material, K_s , is unknown. Then another method to calculate the shear force on the primary shear plane is to use the shear flow stress,

$$(3.2) \quad F_s = \tau_s L_s b.$$

In Eq. (3.2), τ_s is the shear stress on the primary shear plane, L_s is the length of the primary shear plane, and b is the chip width. Thus, given the orthogonal cutting parameters, if there is a good constitutive response model available for the stress in the work material, the cutting forces and temperatures of interest can be predicted using this simple model. Suppose that the constitutive response model for the effective true stress is given by the Johnson-Cook model, Eq. (1.1). Then, according to the von Mises criterion (see, e.g., CHILDS *et al.* [5]),

$$(3.3) \quad \tau_s = \bar{\sigma}(\bar{\epsilon}, \dot{\bar{\epsilon}}, T) / \sqrt{3}.$$

One way to interpret the results obtained in [6] using Thusty's model is that the value of the temperature that should be used in Eq. (3.3) is approximately 600°C . A new experimental measurement of τ_s for AISI 1045, at a temperature that is close to 600°C , is discussed in the next section.

4. NIST PULSE-HEATED KOLSKY BAR DATA

The split-Hopkinson pressure bar (SHPB), which is also called the Kolsky bar, is an experimental system that is widely used to determine the constitutive response of materials under conditions of rapid plastic deformation. A number of techniques have been developed for preheating a sample prior to impact testing in a Kolsky bar. The parameters for the Johnson-Cook constitutive model for AISI 1045 steel (Eqs. (1.1) and (1.2)), that was fit in the paper of JASPERS and DAUTZENBERG [9], were determined in part using data from a Kolsky bar apparatus, in which the samples were pre-heated in situ using a gas furnace, for a time on the order of a hundred seconds, to a temperature of up to 600°C, prior to loading in compression. At the National Institute of Standards and Technology, a unique SHPB facility has been in operation for several years. This laboratory combines a precision-engineered Kolsky bar and a controlled DC electrical pulse-heating system. The flow stress can be measured in samples that have been rapidly pre-heated to temperatures on the order of 1000°C, in a time on the order of one second, at heating rates of up to 6,000°C s⁻¹, and then rapidly loaded in compression at strain rates up to 10⁴ s⁻¹ [12].

4.1. AISI 1075

In recent work [3], pulse-heated compression test results on AISI 1075 steel were reported. The purpose of the experimental study was to investigate the magnitude of the difference in material strength that occurs in a carbon steel due to a transformation from the stronger bcc pearlitic structure to a structure that includes the less-strong fcc austenitic structure. The test samples had been carefully heat treated prior to testing, so that they had a uniform pearlitic microstructure. The particular alloy AISI 1075 was chosen for this study because it has the lowest austenization temperature, 723°C, among the carbon steels. In these tests, which were performed at a nominal strain rate of 3500 s⁻¹, each sample was pulse-heated to the test temperature within 2 s, held at temperature for a further 2.5 s, and then mechanically deformed to a true strain of approximately 0.25 to 0.35 within the next 100 μs. At temperatures above the austenization temperature (723°C) of the material, a nonequilibrium phase transformation from pearlite to austenite was observed to take place. At temperatures below the transformation temperature in this material, it was found that the material exhibited a stiffer response than is typically found in carbon steels. By fixing the value of the strain at 0.1, and the strain rate at 3500 s⁻¹ in the Johnson-Cook model, Eq. (1.1), it was shown that the experimental results could conveniently be summarized by the following expression for the effective true stress vs. the temperature,

$$(4.1) \quad \bar{\sigma}(T) = 1140 \times (1 - T^{*m}) \text{ [MPa]}.$$

What is interesting about these data is that, for experiments in which the material had been preheated to a temperature below the eutectoid temperature, a value of $m = 1.6$ was found to provide a good fit of the model in Eq. (4.1) to the data. This contrasts with the fact that typically, for carbon steels, SHPB tests in which the sample has been preheated more slowly prior to loading in compression, it is found that $m = 1.0$ (see, e.g., [9, 10]). Furthermore, for experiments in which the sample had been preheated to a temperature above the eutectoid, a value of $m = 0.7$ was found to provide a good fit of the model in Eq. (4.1) to the data. Thus, a Johnson-Cook type of model was found to be too simplistic to provide an overall good fit to the data. In addition, for the data on tests which were performed with preheating to a temperature below the eutectoid, a value of the thermal-softening parameter m greater than one is very interesting, because it supports the hypothesis that thermal-softening effects are less than would be expected to be found in experiments performed with a slower method of preheating the sample. This raises the question, does AISI 1045 steel exhibit a similar behaviour when it is pulse-heated, and then loaded in compression?

4.2. AISI 1045

Iron alloys with a smaller percentage of carbon, such as AISI 1045 steel, are used much more frequently than a spring steel like AISI 1075 in manufacturing processes that involve high-speed machining operations. As discussed in Sec. 3, Thusty's model predicts a shear plane temperature of approximately 600°C in AISI 1045, which is below the lowest eutectoid temperature for an iron-carbon system. Could it be that one of the reasons that Thusty's model outperformed the finite-element simulations in [7], in particular using the Jaspers-Dautzenberg fit to the Johnson-Cook model for AISI 1045, is that the actual material has a stiffer response, when it is rapidly heated to a temperature below the eutectoid, than was measured by Jaspers and Dautzenberg using their SHPB system? In other words, just as was described for AISI 1075 in the preceding section, does a value of the thermal-softening parameter m in the Johnson-Cook model that is greater than one provide a better fit to the pulse-heated experimental data than the value $m = 1$ reported in [9]? (Recall that a *larger* value of m corresponds to *less* thermal softening in Eq. (1.1)).

Figure 3 gives a plot of the true shear stress vs. true strain data from a pulse-heated Kolsky bar test that was performed at a nominal strain rate of 3600 s^{-1} . In this test, the sample was heated to a temperature of 640°C (with $\pm 2\sigma$ uncertainty of $\pm 20^{\circ}\text{C}$) in approximately one second, and then it was held at that temperature for approximately 6.2 seconds prior to compressive loading. Also shown in the figure are the uncertainty bounds ($\pm 2\sigma$) on the measurements

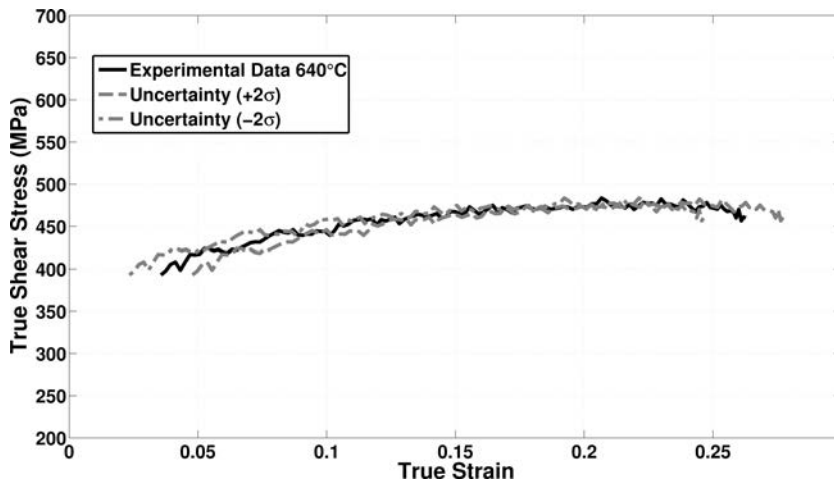


FIG. 3. Data (solid curve) from compression test of a AISI 1045 steel sample that had been pulse-heated to 640°C, and then plastically deformed, at a true strain rate of 3600 s^{-1} ; uncertainty bounds ($\pm 2\sigma$) on true shear stress vs. true strain measurements are also plotted.

(see [12]). The same experimental data are plotted again in Fig. 4, along with two fits to the data, both obtained using the model of Jaspers and Dautzenberg at the same strain rate and temperature, but with $m = 1$ in the lower curve, and $m = 1.7$ in the upper curve. It is clear that the case with $m = 1.7$ provides a better fit to the experimental data, which means that the material exhibits

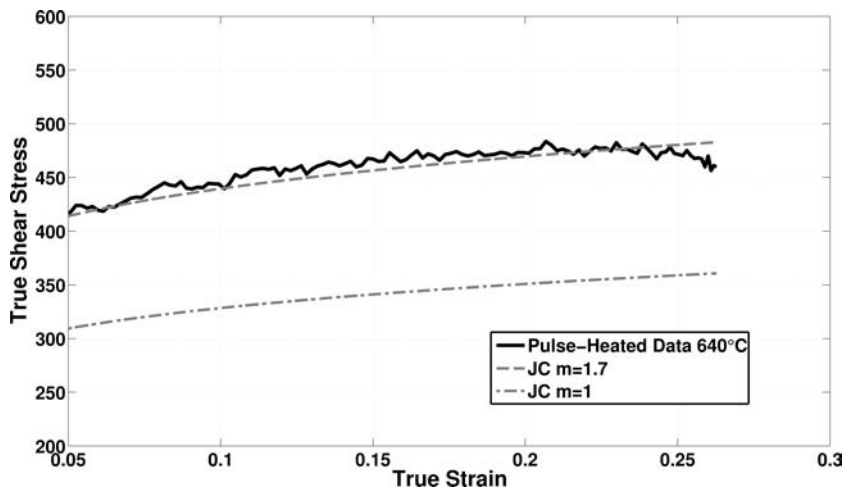


FIG. 4. Same data (solid curve) as in Fig. 3 are plotted, together with corresponding true shear stress vs. true strain values of the Johnson-Cook model for AISI 1045 of Jaspers and Dautzenberg; in the upper (dashed), and lower (dot-dashed) curves, $m = 1.7$ and $m = 1$, respectively.

a stiffer response to loading after it has been rapidly pulse-heated. Thus, this may provide at least a partial explanation for why Thusty's method performed so much better in predicting the peak temperature along the tool-chip interface for the experiments that were reported in [6].

5. DISCUSSION AND CONCLUSIONS

Experimental data on AISI 1045 steel have been presented, which show that the material exhibits a stiffer response when it has been pulse-heated, instead of preheated by a slower method, to a temperature below the eutectoid, prior to a dynamic SHPB compression test. These new data, together with the discussion of Thusty's model in Sec. 3, imply that, for machining simulations, a value of $m = 1.7$, instead of $m = 1$, and a value of the temperature on the order of 600°C , are preferable for the Johnson-Cook model, Eq. (1.1), for FEA simulations of high-speed machining of AISI 1045. The work presented here supports the hypothesis that there is insufficient time for many significant microstructural changes to occur in the material during a high-speed machining operation. Thus, this may help to explain why the finite-element simulations of orthogonal cutting tests on this material were found to underpredict the peak temperatures measured in corresponding orthogonal cutting experiments [7].

As a final observation, the true shear stress vs. true shear strain data from Fig. 3 are plotted again in Fig. 5, along with the two plots of the Johnson-Cook model for AISI 1045 of Jaspers and Dautzenberg, where the maximum

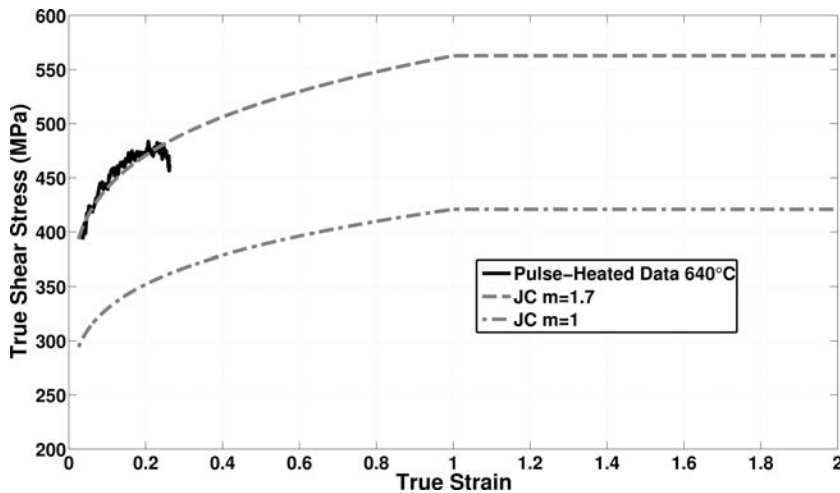


FIG. 5. Same data (solid curve) as in Fig. 3, plotted with values of the Johnson-Cook model for AISI 1045 of Jaspers and Dautzenberg, for true shear strains up to 2.0; it is assumed that $n=0$ for effective true plastic strains greater than 1.0.

strain is extended to 2.0, which is of the correct order for machining. For effective true strains greater than 1.0, it is assumed that there is no additional strain-hardening, i.e., $n = 0$; see CHILDS *et al.* [5]. This figure emphasizes that modelling of high-speed machining operations usually requires large extrapolations from data that have been obtained using currently available experimental methods, which typically means Kolsky bar (SHPB) tests. Ideally, constitutive data for machining simulations ought to be determined by means of some carefully designed cutting experiments.

ACKNOWLEDGMENT

This paper is an official contribution of the National Institute of Standards and Technology and is not subject to copyright in the United States. Commercial products are identified in order to adequately specify certain procedures. In no case does such identification imply recommendation or endorsement by the National Institute of Standards and Technology, nor does it imply that the identified products are necessarily the best available for the purpose.

REFERENCES

1. *ABAQUS/Explicit Users' Manual*, Hibbit, Karlsson & Sorenson, Inc., Rising Sun Mills, 166 Valley Street, Providence, RI 02909-2499, 2003.
2. BOOTHROYD G., *Temperatures in orthogonal metal cutting*, Proc. IME, **177**, 29, 789–802, 1963.
3. BURNS T.J., MATES S.P., RHORER R.L., WHITENTON E.P., BASAK D., *Dynamic properties for modeling and simulation of machining: effect of pearlite to austenite phase transition on flow stress in AISI 1075 steel*, Mach. Sci. and Tech., **15**, 1–20, 2011.
4. BURYTA D., SOWERBY R., YELLOWLEY I., *Stress distributions on the rake face during orthogonal machining*, Int. J. Mach. Tools Manufact., **345**, 721–739, 1994.
5. CHILDS T.H.C., MAEKAWA K., OBIKAWA T., YAMANE Y., *Metal Machining: Theory and Applications*, Arnold Publishers, London, 2000.
6. DAVIES M.A., YOON H., SCHMITZ T.L., BURNS T.J., KENNEDY M.D., *Calibrated thermal microscopy of the tool-chip interface in machining*, Mach. Sci. and Tech., **7**, 2, 166–190, 2003.
7. DAVIES M.A., CAO Q., COOKE A.L., IVESTER R., *On the measurement and prediction of temperature fields in machining AISI 1045 steel*, CIRP Ann., **52**, 1, 77–80, 2003.
8. JASPERS S.P.F.C., *Metal Cutting Mechanics and Material Behaviour*, Ph.D. Thesis, Eindhoven: Technische Universiteit Eindhoven, 1999.
9. JASPERS S.P.F.C., DAUTZENBERG J.H., *Material behaviour in conditions similar to metal cutting: flow stress in the primary shear zone*, J. Mater Proc. Tech., **122**, 322–330, 2002.

10. JOHNSON G.R., COOK W.H., *A constitutive model and data for metals subjected to large strains, high strain rates and high temperatures*, 7th International Symposium on Ballistics, 541–547; The Hague, Netherlands, 1983.
11. KALUBA W.J., TAILLARD R., FOCT J., *The bainitic mechanism of austenite formation during rapid heating*, *Acta Mater.*, **46**, 16, 5917–5927, 1998.
12. MATES S.P., RHORER R.L., WHITENTON E.P., BURNS T.J., BASAK D., *A pulse-heated Kolsky bar technique for measuring flow stress of metals subjected to high loading and heating rates*, *Exp. Mech.*, **48**, 799–807, 2008.
13. TLUSTY J., *Manufacturing Processes and Equipment*, Prentice-Hall, Upper Saddle River, NJ, 2000.

Received June 1, 2011; revised version May 25, 2012.

Limit Condition for Anisotropic Materials with Asymmetric Elastic Range

Janina OSTROWSKA–MACIEJEWSKA¹⁾,
Ryszard Bolesław PECHERSKI^{1),2)}, Paweł SZEPTYŃSKI²⁾

¹⁾ *Institute of Fundamental Technological Research
Polish Academy of Sciences*

Pawińskiego 5B, 02-106 Warszawa, Poland
e-mail: rpecher@ippt.pan.pl

²⁾ *AGH University of Science and Technology
Faculty of Mechanical Engineering and Robotics
Department of Strength, Fatigue of Materials and Structures
Al. A. Mickiewicza 30, 30-059 Kraków, Poland*

In the paper a new proposition of an energy-based hypothesis of material effort is introduced. It is based on the concept of influence functions introduced by BURZYŃSKI [3] and on the concept of decomposition of elastic energy density introduced by RYCHLEWSKI [18]. A new proposition enables description of a wide class of linearly elastic materials of arbitrary symmetry exhibiting strength differential effect.

Key words: linear elasticity, anisotropy, material effort hypotheses, limit state criteria.

1. INTRODUCTION

The aim of the paper is to introduce a new proposition of a limit condition for anisotropic bodies. In Sec. 2 the foundations of the energy-based hypothesis of material effort proposed by Rychlewski is briefly discussed, while the further parts of the paper are devoted to presentation of the own proposition of the authors. In Sec. 3 a new proposition of the energy-based hypothesis of material effort is presented. The introduction of the influence functions plays essential role by accounting for the assymetry of elastic range. Then the detail discussion of failure criteria specified for some chosen elastic symmetries is provided. The important from practical point of view case of plane orthotropy is studied and the possibilities of specification of the yield criterion in this case are discussed.

Finally, the case of isotropic solid is studied. The specification of influence functions reveals that the earlier discussed case of the criterion accounting for the influence of the Lode angle or in particular the classical Burzyński criterion can be obtained.

Our approach to the problem of the formulation of a limit condition yields from the energy-based concepts of BURZYŃSKI [3] and RYCHLEWSKI [18]. It distinguishes, however in accounting for the asymmetry of the elastic range, which manifests itself in the difference of the values of yield strength in tension and compression performed with use of the specimen cut out of anisotropic material in any direction. This is the so-called strength differential effect, discussed e.g. by DRUCKER [4] or SPITZIG, SOBER and RICHMOND [20]. Among other earlier formulations of the limit criteria accounting for anisotropy (MISES [11], HILL [7]), strength differential effect (DRUCKER-PRAGER [5], BIGONI-PICCOLROAZ [2]) or both of those features (HOFFMAN [8], TSAI-WU [24], THEOCARIS [23]) the criteria derived from the hypothesis that the measure of material effort is the density of elastic energy accumulated in an anisotropic solid have the following advantages:

- physical interpretation as a combination of energy densities connected with certain energetically independent stress states,
- general treatment of the linear elastic anisotropy due to application of the spectral decomposition of elasticity tensors.

2. THEORETICAL FOUNDATIONS OF ENERGY-BASED APPROACH

In the linear theory of elasticity an important role is played by certain fourth order tensors, namely compliance tensor \mathbf{C} , stiffness tensor \mathbf{S} and limit state tensor \mathbf{H} . First two tensors appear in the generalized Hooke's law as a linear operators mapping the space of symmetric second order tensors into itself $\mathcal{S} \rightarrow \mathcal{S}$

$$(2.1) \quad \begin{cases} \boldsymbol{\sigma} = \mathbf{S} \cdot \boldsymbol{\varepsilon} \\ \boldsymbol{\varepsilon} = \mathbf{C} \cdot \boldsymbol{\sigma} \\ \mathbf{C} : \mathbf{S} = \mathbf{S} : \mathbf{C} = \mathbf{I}^S \end{cases} \Rightarrow \begin{cases} \sigma_{ij} = S_{ijkl} \varepsilon_{kl} \\ \varepsilon_{ij} = C_{ijkl} \sigma_{kl} \\ C_{ijkl} S_{klmn} = S_{ijkl} C_{klmn} = \frac{1}{2} (\delta_{im} \delta_{jn} + \delta_{in} \delta_{jm}), \end{cases}$$

where $\boldsymbol{\sigma}$ is the Cauchy stress tensor, $\boldsymbol{\varepsilon}$ is the symmetric part of the gradient of small displacements (infinitesimal strain tensor) and \mathbf{I}^S is an identity operator in the space of symmetric second order tensors. The limit state tensor \mathbf{H} appears in the quadratic form of a limit state condition, which constitutes a constraint on the range of stresses for which the Hooke's law is valid

$$(2.2) \quad \boldsymbol{\sigma} \cdot \mathbf{H} \cdot \boldsymbol{\sigma} \leq 1.$$

If we consider Levy-Mises flow rule associated with the limit condition of the type as shown above then the constitutive relations between an increment of plastic strain and stress state is expressed by the limit state tensor \mathbf{H} which acts as an linear operator on \mathcal{S} :

$$(2.3) \quad \dot{\boldsymbol{\varepsilon}}^p = \dot{\lambda} \mathbf{H} \cdot \boldsymbol{\sigma}.$$

Finally the stiffness and compliance tensors appear in the expression for the elastic energy density as a quadratic forms

$$(2.4) \quad \Phi = \frac{1}{2} \boldsymbol{\sigma} \cdot \mathbf{C} \cdot \boldsymbol{\sigma} = \frac{1}{2} \boldsymbol{\varepsilon} \cdot \mathbf{S} \cdot \boldsymbol{\varepsilon}.$$

One can see that each of these three tensors \mathbf{C} , \mathbf{S} and \mathbf{H} can be treated both as a linear operator and a quadratic form. Unless none of the so-called “locked” stress or strain states as well as the safe stress states are taken into consideration all quadratic forms $\boldsymbol{\sigma} \cdot \mathbf{C} \cdot \boldsymbol{\sigma}$, $\boldsymbol{\varepsilon} \cdot \mathbf{S} \cdot \boldsymbol{\varepsilon}$, $\boldsymbol{\sigma} \cdot \mathbf{H} \cdot \boldsymbol{\sigma}$ are positive definite and symmetric.

Tensors \mathbf{C} , \mathbf{S} and \mathbf{H} have internal symmetries characterized by the symmetry group

$$(2.5) \quad \tilde{\sigma}_4 = \{\langle 1, 2, 3, 4 \rangle, \langle 2, 1, 3, 4 \rangle, \langle 1, 2, 4, 3 \rangle, \langle 3, 4, 1, 2 \rangle\}.$$

which ensures existence of real eigenvalues of those operators. According to the classical theorem on the spectral decomposition of a linear operator each of the considered fourth rank tensors can be represented in the following form [17, 19]:

$$(2.6) \quad \begin{aligned} \mathbf{S} &= \lambda_1 \mathbf{P}_1 + \lambda_2 \mathbf{P}_2 + \dots + \lambda_\rho \mathbf{P}_\rho = \lambda_I (\boldsymbol{\omega}_I \otimes \boldsymbol{\omega}_I) + \dots + \lambda_{VI} (\boldsymbol{\omega}_{VI} \otimes \boldsymbol{\omega}_{VI}), \\ \mathbf{C} &= \frac{1}{\lambda_1} \mathbf{P}_1 + \frac{1}{\lambda_2} \mathbf{P}_2 + \dots + \frac{1}{\lambda_\rho} \mathbf{P}_\rho = \frac{1}{\lambda_I} (\boldsymbol{\omega}_I \otimes \boldsymbol{\omega}_I) + \dots + \frac{1}{\lambda_{VI}} (\boldsymbol{\omega}_{VI} \otimes \boldsymbol{\omega}_{VI}), \\ \mathbf{H} &= \frac{1}{h_1} \mathbf{R}_1 + \frac{1}{h_2} \mathbf{R}_2 + \dots + \frac{1}{h_\chi} \mathbf{R}_\chi = \frac{1}{h_I} (\mathbf{h}_I \otimes \mathbf{h}_I) + \dots + \frac{1}{h_{VI}} (\mathbf{h}_{VI} \otimes \mathbf{h}_{VI}), \\ &\quad \rho, \chi \leq 6, \end{aligned}$$

where $\boldsymbol{\omega}_K$ and \mathbf{h}_K are the second order tensors representating the eigenstates corresponding with the K -th eigenvalue of the considered operators and \mathbf{P}_K and \mathbf{R}_K are orthogonal projectors on the corresponding eigensubspaces. The expression of the linear operators \mathbf{C} , \mathbf{S} , \mathbf{H} as a linear combination of orthogonal projectors is unique. It is not so in case of the decomposition into the scaled sum of dyads of the eigenstates. In case of multidimensional eigensubspaces the basis of the eigenstates in such subspace can be done arbitrary in an infinite number of ways.

If the elasticity tensors and the limit state tensor are coaxial then they have the same eigensubspaces and thus the same orthogonal projectors, however even then they may still have different eigenvalues. If any eigensubspace of one of those tensors is not an eigensubspace of the other one but it is still a direct sum of eigenspaces of this second tensor then we call those tensors as being compatible. Even in case when elasticity tensors and limit state tensor are not coaxial but they are still compatible, there exists such a basis in which each of those tensors can be expressed as a linear combination of dyads of the same set of eigenstates. It can be also shown that if two tensors are compatible and all of their eigensubspaces are one-dimensional, then they are coaxial.

According to the theorems of algebra for any quadratic form, there exists a bilinear form which is polar to the considered quadratic form [6]. The linear space of the symmetric second order tensors becomes an euclidean space when a scalar product is defined in it. RYCHLEWSKI [18] has used the theorem on the simultaneous reduction of two quadratic forms $\boldsymbol{\sigma} \cdot \mathbf{C} \cdot \boldsymbol{\sigma}$ and $\boldsymbol{\sigma} \cdot \mathbf{H} \cdot \boldsymbol{\sigma}$ to their canonical forms, assuming that the scalar product is defined as:

$$(2.7) \quad \begin{aligned} \boldsymbol{\sigma}_1 \bullet \boldsymbol{\sigma}_2 &= \boldsymbol{\sigma}_1 \cdot \mathbf{C} \cdot \boldsymbol{\sigma}_2 = \boldsymbol{\sigma}_2 \cdot \mathbf{C} \cdot \boldsymbol{\sigma}_1 \\ \boldsymbol{\sigma}_1 \perp \boldsymbol{\sigma}_2 &\Leftrightarrow \boldsymbol{\sigma}_1 \bullet \boldsymbol{\sigma}_2 = 0 \end{aligned}$$

to formulate the following theorem:

THEOREM 1: Rychlewski's theorem [18].

For every elastic material defined by its compliance tensor \mathbf{C} and limit state tensor \mathbf{H} , there exist exactly one energetically orthogonal decomposition of the linear space of symmetric second order tensors \mathcal{S} :

$$(2.8) \quad \begin{aligned} \mathcal{S} &= \mathcal{H}_1 \oplus \dots \oplus \mathcal{H}_\chi, \quad \chi \leq 6, \\ \mathcal{H}_\alpha &\perp \mathcal{H}_\beta \quad \text{for } \alpha \neq \beta \end{aligned}$$

and exactly one set of pairwise unequal constants

$$(2.9) \quad h_1, \dots, h_\chi, \quad h_\alpha \neq h_\beta \quad \text{for } \alpha \neq \beta$$

such that, for an arbitrary stress state $\boldsymbol{\sigma}$

$$(2.10) \quad \boldsymbol{\sigma} = \boldsymbol{\sigma}_1 + \dots + \boldsymbol{\sigma}_\chi, \quad \boldsymbol{\sigma}_\alpha \in \mathcal{H}_\alpha$$

the measure of material effort given by formula (2.2) is equal

$$(2.11) \quad \boldsymbol{\sigma} \mathbf{H} \boldsymbol{\sigma} = \frac{1}{h_1} \Phi(\boldsymbol{\sigma}_1) + \dots + \frac{1}{h_\chi} \Phi(\boldsymbol{\sigma}_\chi)$$

where

$$(2.12) \quad \Phi(\boldsymbol{\sigma}_1) + \dots + \Phi(\boldsymbol{\sigma}_\chi) = \Phi(\boldsymbol{\sigma}) = \frac{1}{2} \boldsymbol{\sigma} \cdot \mathbf{C} \cdot \boldsymbol{\sigma}$$

is the total elastic energy density.

Let us remind that none of the so-called “locked” stress or strain states (corresponding with the zero Kelvin modulus) are allowed in this case since the operator used for the definition of the scalar product must be positive definite. We will call the limit condition of form (2.11) the *Rychlewski limit condition*. If only a single stress state component $\boldsymbol{\sigma}_\alpha$ (from the decomposition (2.10)) occurs in the limit condition (2.11) then it can be rewritten in the following form:

$$(2.13) \quad \Phi(\boldsymbol{\sigma}_\alpha) = h_\alpha.$$

The quantity h_α can be interpreted as a limit value of the energy density corresponding to the specified stress state $\boldsymbol{\sigma}_\alpha$.

Rychlewski has interpreted the scalar product defined in (2.7) in terms of energy - one can note that in case of any two stress states which are orthogonal in the sense of the considered scalar product, the work performed by one of the stress state through strains respective for the other one are equal zero:

$$(2.14) \quad \boldsymbol{\sigma}_1 \bullet \boldsymbol{\sigma}_2 = \boldsymbol{\sigma}_1 \cdot \underbrace{\mathbf{C} \cdot \boldsymbol{\sigma}_2}_{\boldsymbol{\varepsilon}_2} = 0 \quad \Rightarrow \quad \mathcal{L} = \frac{1}{2} \boldsymbol{\varepsilon}_1 \cdot \boldsymbol{\sigma}_2 = \frac{1}{2} \boldsymbol{\sigma}_1 \cdot \boldsymbol{\varepsilon}_2 = 0.$$

In general, tensors \mathbf{C} and \mathbf{H} are independent – in [9] an energy-based limit condition for solids of cubic elasticity and orthotropic limit state is discussed. If \mathbf{C} and \mathbf{H} are coaxial (they have the same eigensubspaces) then the decomposition of \mathcal{S} into eigensubspaces of each of those tensors is the same in both cases and the stress states $\boldsymbol{\sigma}_\alpha$ are the eigenstates of the stiffness and compliance tensors as well as of the limit state tensor. Then decomposition of elastic energy density (2.12) takes the following form:

$$(2.15) \quad \Phi(\boldsymbol{\sigma}) = \Phi(\boldsymbol{\sigma}_1) + \dots + \Phi(\boldsymbol{\sigma}_\rho) \quad \rho \leq 6,$$

where stress states $\boldsymbol{\sigma}_1, \dots, \boldsymbol{\sigma}_\rho$ are both orthogonal and energetically orthogonal. It is the only such decomposition of the energy density in which mutually energetically orthogonal states are also mutually orthogonal in sense of classical definition of the scalar product. We call it the *main decomposition* of the elastic energy density. Examples of the limit criteria based on the main decomposition of elastic energy density for cubic symmetry and transversal isotropy can be found in [12].

3. NEW PROPOSITION OF AN ENERGY-BASED HYPOTHESIS OF MATERIAL EFFORT

Authors' proposition of a limit condition for pressure-sensitive materials of arbitrary symmetry, exhibiting strength differential effect will be now introduced. Making use of the innovative idea of Burzyński we can modify Rychlewski's yield condition (2.11) in a way similar to the one in which Burzyński modified classical yield condition by MAXWELL–HUBER [18], namely by taking into account only parts of the specified energy densities, defining their contribution to the total measure of material effort by multiplying their values by a proper functions of the stress state in the corresponding subspace – let's call them *influence functions* η_α

$$(3.1) \quad \eta_1 \Phi(\boldsymbol{\sigma}_1) + \dots + \eta_\chi \Phi(\boldsymbol{\sigma}_\chi) = 1, \quad \boldsymbol{\sigma}_\alpha \in \mathcal{H}_\alpha, \quad \chi \leq 6,$$

where

$$(3.2) \quad \Phi(\boldsymbol{\sigma}_1) + \dots + \Phi(\boldsymbol{\sigma}_\chi) = \Phi$$

is the total elastic energy density and

$$(3.3) \quad \boldsymbol{\sigma}_1 + \dots + \boldsymbol{\sigma}_\chi = \boldsymbol{\sigma}, \quad \boldsymbol{\sigma}_\alpha \in \mathcal{H}_\alpha, \\ \mathcal{H}_1 \oplus \dots \oplus \mathcal{H}_\chi = \mathcal{S}$$

is any decomposition of the strain and stress state space \mathcal{S} into direct sum of mutually energetically orthogonal tensor subspaces \mathcal{H}_α . The introduced influence functions should be interpreted as a scaling parameters (weights) describing the contribution of each term of energy density into the measure of material effort according to the current stress state. The clue difference between the newly introduced proposition and the Rychlewski's criterion (2.11) is that ***the coefficients of the linear combination of the energy densities are not constant (only material dependent) parameters but they are also functions of the current stress state.*** In this way they take into account various modes of the stress states belonging to the corresponding subspace. The influence functions play then the role of the *stress mode indicators*.

In particular one can consider a special case in which the decomposition (3.3) coincide with the decomposition of \mathcal{S} into eigensubspaces of the elasticity tensors. If the influence functions are constant scalar parameters then the proposed limit condition is equivalent to the generalized quadratic limit condition (2.2) and the special case mentioned above occurs when the limit tensor \mathbf{H} is coaxial with the elasticity tensors. Such choice of the decomposition of \mathcal{S} seems to be the most natural one of all possible energetically orthogonal decompositions of \mathcal{S} since it is the only one which is both energetically orthogonal and orthogonal.

3.1. Assumptions on influence functions

Following assumptions are made for the influence functions.

Interpretation of the value of influence functions at the limit state

If, under certain load, only a single term of energy occurs in the limit condition, then the influence function defines the limit value of the elastic energy density corresponding with the considered stress and strain state:

$$(3.4) \quad \Phi_{\alpha}^{\text{lim}} = \frac{1}{\eta_{\alpha}}$$

Domain of the influence functions

It seems natural that, to keep mutual independence of all terms of the condition, each influence function η_{α} should depend only on the projection of a stress state $\boldsymbol{\sigma}$ on the tensor subspace \mathcal{H}_{α} , this means on $\boldsymbol{\sigma}_{\alpha}$.

$$(3.5) \quad \eta_{\alpha} = \eta_{\alpha}(\boldsymbol{\sigma}_{\alpha}) \quad (\text{no summation!})$$

Isotropy of the influence functions in their domains

Since η_{α} is a scalar function of a tensor argument one should expect that in practical calculations it is expressed in terms of components or invariants of $\boldsymbol{\sigma}_{\alpha}$. To define it by components of $\boldsymbol{\sigma}_{\alpha}$ one should chose certain basis in the corresponding subspace which in case of multidimensional subspaces can be done arbitrary in the infinite number of ways. This purely mathematical operation distinguishes certain stress states (basis states) among an infinite number of eigenstates belonging to that subspace and it has no physical sense. This is why functions η_{α} are assumed to be isotropic in the subspace in which they are defined – according to the theorem on the representation of the scalar isotropic functions, they can be expressed in terms of invariants of corresponding stress projection

$$(3.6) \quad \eta_{\alpha}(\boldsymbol{\sigma}_{\alpha}) = \eta_{\alpha}(I_1(\boldsymbol{\sigma}_{\alpha}); I_2(\boldsymbol{\sigma}_{\alpha}); I_3(\boldsymbol{\sigma}_{\alpha})).$$

The arguments of influence functions could be also any other invariants of $\boldsymbol{\sigma}_{\alpha}$ – i.e. its principal values, its norm etc. If the considered space is one-dimensional then each invariant is proportional to the measure of projection (or its power) of the stress state onto the considered space – thus this measure should be the only argument of the influence function.

Influence functions in subspaces of deviators

If the considered eigensubspace is a space of deviators then $I_1(\boldsymbol{\sigma}_{\alpha}) = 0$ and $I_2(\boldsymbol{\sigma}_{\alpha})$ is proportional to the corresponding energy density. This indicates that in fact it is the third invariant of stress tensor deviator which makes the qualitative distinction between various deviators belonging to the same subspace.

It is strictly connected with abstract angles in multidimensional subspace of deviators – a kind of curvilinear coordinates in the considered subspace. Lode angle is an example of such parameter in case of isotropy. In case of one-dimensional deviatoric subspaces influence function is a constant parameter which is equal the inversion of the limit value of the energy density respective for this state.

3.2. Failure criterion specification for chosen elastic symmetries

Let us now present a few examples of the general specification of the discussed proposition of a limit condition. It is assumed that the considered energetically orthogonal decomposition of the linear space of symmetric second order tensors is the one respective for the spectral decomposition of the stiffness and compliance tensor – then the proposed limit condition is a combination of terms of the main decomposition of the elastic energy density with unequal, stress state dependent weights.

3.2.1. Plane orthotropy. Energetic character of the considered hypothesis makes it easy to formulate the failure criterion in case of plane stress/strain state. Omitting description of a total plane anisotropy (lack of any symmetry) we will now discuss general plane orthotropy. Spectral decomposition of the plane orthotropic elasticity tensors gives us three orthogonal eigensubspaces:

- one-dimensional subspace of the states with non-zero hydrostatic component

$$\lambda_1 = \frac{2E_x E_y}{(E_x + E_y) + \sqrt{(E_x - E_y)^2 + 4\nu^2 E_x^2}}, \quad \boldsymbol{\omega}_1 \cong \begin{bmatrix} \cos \aleph & 0 \\ 0 & \sin \aleph \end{bmatrix},$$

- one-dimensional subspace of the states with non-zero hydrostatic component

$$\lambda_2 = \frac{2E_x E_y}{(E_x + E_y) - \sqrt{(E_x - E_y)^2 + 4\nu^2 E_x^2}}, \quad \boldsymbol{\omega}_2 \cong \begin{bmatrix} -\sin \aleph & 0 \\ 0 & \cos \aleph \end{bmatrix},$$

where

$$\tan \aleph = -\frac{E_x}{2\nu} \left[\frac{1}{E_y} - \frac{1}{E_x} + \sqrt{\left(\frac{1}{E_y} - \frac{1}{E_x}\right)^2 + 4\left(\frac{\nu}{E_x}\right)^2} \right],$$

- one dimensional subspace of pure shears

$$\lambda_3 = 2G_{xy}, \quad \boldsymbol{\omega}_3 \cong \frac{1}{\sqrt{2}} \begin{bmatrix} 0 & 1 \\ 1 & 0 \end{bmatrix},$$

where E_x E_y are the Young moduli and G_{xy} is the Kirchhoff modulus, each measured in the directions of the plane orthotropy, and ν is the Poisson's ratio at tension/compression along the x direction. Failure criterion (3.1) takes form

$$(3.7) \quad \Phi_1 \tilde{\eta}_1 + \Phi_2 \tilde{\eta}_2 + \Phi_3 \frac{1}{h_3} = 1,$$

where h_3 is the limit value of the elastic energy density corresponding with the shearing eigenstate. Since all eigensubspaces of the plane orthotropic elasticity tensor are one-dimensional all invariants of each projection of the stress state onto every subspace are proportional to the measure of this projection or its power. The limit condition may be thus rewritten in the following form

$$(3.8) \quad \eta_1(\sigma_1) \cdot \sigma_1^2 + \eta_2(\sigma_2) \cdot \sigma_2^2 + \frac{\sigma_3^2}{2k_s} = 1,$$

where projections on proper eigensubspaces (not to be mistaken with principal stresses):

$$\begin{aligned} \sigma_1 &= \sigma_{xx} \cos \aleph + \sigma_{yy} \sin \aleph, \\ \sigma_2 &= -\sigma_{xx} \sin \aleph + \sigma_{yy} \cos \aleph, \\ \sigma_3 &= \sqrt{2} \tau_{xy}. \end{aligned}$$

The parameters η_1 and η_2 are unknown influence functions and k_s is the limit shear stress in the directions parallel and perpendicular to the symmetry axes of the material. The proposed general limit condition in a very special case of plane stress state together with its specification for chosen plane symmetries is discussed in details in [22].

3.2.2. Plane symmetry of square. Special case of orthotropy in which elastic properties of the material are identical in two perpendicular directions and different than in any other pair of perpendicular directions is called the symmetry of square. It can be considered as the plane orthotropy for which $E_x = E_y = E$ what corresponds with the value of the parameter $\tan \aleph = -1$. Spectral decomposition of the plane elasticity tensors characterized by the symmetry of square gives us three orthogonal eigensubspaces:

- one-dimensional subspace of plane hydrostatic stress states

$$\lambda_1 = \frac{E}{1-\nu}, \quad \omega_1 \cong \frac{1}{\sqrt{2}} \begin{bmatrix} 1 & 0 \\ 0 & 1 \end{bmatrix},$$

- one-dimensional subspace of pure shears in directions at angle 45° referring to the symmetry axes

$$\lambda_2 = \frac{E}{1 + \nu}, \quad \boldsymbol{\omega}_2 \cong \frac{1}{\sqrt{2}} \begin{bmatrix} 1 & 0 \\ 0 & -1 \end{bmatrix},$$

- one dimensional subspace of pure shears in directions parallel and perpendicular to the symmetry axes

$$\lambda_3 = 2G_{xy}, \quad \boldsymbol{\omega}_3 \cong \frac{1}{\sqrt{2}} \begin{bmatrix} 0 & 1 \\ 1 & 0 \end{bmatrix},$$

The limit condition can be rewritten in the following form:

$$(3.9) \quad \eta_v(p) \cdot p^2 + \frac{\tau_{45}^2}{k_{s45}^2} + \frac{\tau^2}{2k_s^2} = 1$$

where $p = \frac{1}{2}(\sigma_{xx} + \sigma_{yy})$, $\tau_{45} = \frac{1}{\sqrt{2}}(\sigma_{yy} - \sigma_{xx})$, $\tau = \sqrt{2}\tau_{xy}$ and k_s and k_{s45} are the limit shear stresses at pure shear along symmetry axes and at angle 45° to the symmetry axes respectively. Parameters k_s and k_{s45} can be found during shearing properly oriented samples. It is worth noting that the sole term in the limit condition which is still unknown is only pressure dependent. Since uniaxial stress state has non-zero hydrostatic component, which in turn changes as the orientation of the uniaxial load referring to the symmetry axes changes, so the values of the pressure influence function can be explicitly found during simple tension/compression test at various orientations of the specimen:

$$(3.10) \quad \eta_v \left(\frac{1}{2}k_\varphi \right) = \frac{4}{k_\varphi^2} \cdot \left[1 - \left(\frac{(\tau_{45}(\varphi))^2}{k_{s45}^2} + \frac{(\tau(\varphi))^2}{2k_s^2} \right) \right],$$

where k_φ is the limit normal stress at tension / compression in direction at angle φ referring to the symmetry axes and

$$(3.11) \quad \begin{aligned} \tau_{45}(\varphi) &= \frac{k_\varphi}{\sqrt{2}} (\cos^2 \varphi - \sin^2 \varphi), \\ \tau(\varphi) &= k_\varphi \sqrt{2} \cos \varphi \sin \varphi. \end{aligned}$$

If the Burzyński's [3] pressure influence function is assumed then $\eta_p(p)$ takes the following form:

$$(3.12) \quad \eta_p(p) = \left[\frac{4}{k_c k_r} - \frac{1}{k_{s45}^2} \right] + \frac{2}{p} \cdot \frac{(k_c - k_r)}{k_c k_r},$$

where k_c and k_r denote limit uniaxial stress along the symmetry axes at compression and at tension respectively.

3.2.3. *Case of isotropy.* In case of isotropy criterion (3.1) can be written as follows:

$$(3.13) \quad \tilde{\eta}_f(J_2, J_3)\Phi_f + \tilde{\eta}_v(I_1)\Phi_v = 1,$$

where I_1 is the first stress tensor invariant, and J_2, J_3 are second and third stress deviator invariants respectively. Using principal stresses (which is allowed in case of isotropy without further assumptions on the orientation of coordinate system) it can be rewritten in the following form:

$$(3.14) \quad \eta_f(\theta)q^2 + \eta_p(p) = 1,$$

where

$$\begin{aligned} p &= \frac{1}{3}I_1 = \frac{1}{3}(\sigma_1 + \sigma_2 + \sigma_3) = \frac{1}{3}(\sigma_{xx} + \sigma_{yy} + \sigma_{zz}), \\ q &= \sqrt{2J_2} = \sqrt{\frac{1}{3}[(\sigma_2 - \sigma_3)^2 + (\sigma_3 - \sigma_1)^2 + (\sigma_1 - \sigma_2)^2]} \\ &= \sqrt{\frac{1}{3}[(\sigma_{yy} - \sigma_{zz})^2 + (\sigma_{zz} - \sigma_{xx})^2 + (\sigma_{xx} - \sigma_{yy})^2 + 6(\tau_{yz}^2 + \tau_{zx}^2 + \tau_{xy}^2)]}, \\ \theta &= \frac{1}{3} \arccos \left(\frac{3\sqrt{3}}{2} \frac{J_3}{J_2^{3/2}} \right) - \text{Lode angle.} \end{aligned}$$

The only limitation for the form of the Lode angle influence function is that it has to be periodic with the period equal 120° . It is often assumed that the function describing the influence of the Lode angle is in fact a function of a variable $y = \cos(3\theta)$. Specific form of the Lode angle influence function can be chosen among many propositions available in the literature [1], e.g.:

- two-parameter power function by RANIECKI and MRÓZ [16]

$$\eta_f(\theta) = [1 + \alpha y]^\beta,$$

- two-parameter exponential function by RANIECKI and MRÓZ [16]

$$\eta_f(\theta) = 1 + \alpha \left[1 - e^{-\beta(1+y)} \right],$$

- one-parameter trigonometric function by LEXCELLENT *et al.* [10]

$$\eta_f(\theta) = \cos \left[\frac{1}{3} \arccos [1 - \alpha(1 - y)] \right],$$

- two-parameter trigonometric function by PODGÓRSKI [15] (see also BIGONI and PICCOLROAZ [2])

$$\eta_f(\theta) = \frac{1}{\cos(30^\circ - \beta)} \cos \left[\frac{1}{3} \arccos(\alpha \cdot y) - \beta \right].$$

Isotropic case of the presented proposition was discussed in details in [13] and [21]. Its specification according to the experimental data available in the literature was presented in [14].

It is worth mentioning that after substituting:

$$(3.15) \quad \tilde{\eta}_v(I_1) = \begin{cases} -\frac{2K}{p^2} \cdot Mp_c \sqrt{(F - F^m) [2(1 - \alpha)F + \alpha]} & \text{if } F \in [0, 1], \\ +\infty & \text{if } F \notin [0, 1], \end{cases}$$

$$(3.16) \quad \tilde{\eta}_f(J_2, J_3) = \frac{2\sqrt{6}G}{q} \cos \left[\beta \frac{\pi}{6} - \frac{1}{3} \arccos(\gamma \cos(3\theta)) \right],$$

where K is the bulk modulus, G is the shear modulus, F is defined as:

$$(3.17) \quad F = \frac{-p + c}{p_c + c}$$

and p_c , c , m , M , α , β , γ are certain constant material parameters, then the presented general limit condition for isotropy (3.13) is equivalent to the one proposed and precisely analyzed in various aspects by BIGONI and PICCOLROAZ in [2].

4. SUMMARY AND CONCLUSIONS

The new proposition of an energy-based hypothesis of material effort for anisotropic materials exhibiting strength differential effect was introduced. General statement derived from Burzyński's idea of influence functions and Rychlewski's theorems on the orthogonal and energetically orthogonal decompositions of the space of symmetric second rank tensors was presented. Particular assumptions on the form and properties of the influence functions were formulated.

It was stated in the second section that the studied limit condition should be applied only in case of proportionality limit state due to assumption of validity of Hooke's law used in its derivation. However it seems that the mathematical form of this condition could be well used also in case of e.g. yield limit. It also seems reasonable to use it as a plastic potential in an associated flow rule,

however it might need some modifications e.g. due to requirement of material's incompressibility. Some applications of the newly introduced limit condition for Inconel 718 alloy according to the experimental results available in the literature are presented in [14].

ACKNOWLEDGMENT

The paper has been prepared within the framework of the two research projects N N501 1215 36 and N N507 2311 40 (Subsec. 3.2) of the Ministry of Science and Higher Education of Poland.

REFERENCES

1. BARDET J.P., *Lode dependences for isotropic pressure sensitive materials*, J. Appl. Mech., **57**, 498–506, 1990.
2. BIGONI D., PICCOLROAZ A., *Yield criteria for quasibrittle and frictional materials*, Int. J. Solids Structures, **41**, 2855–2878, 2004.
3. BURZYŃSKI W., *Studium nad hipotezami wytrzymałości*, Akademia Nauk Technicznych, Lwów, 1928; see also: *Selected passages from Włodzimierz Burzyński's doctoral dissertation "Study on material effort hypotheses"*, Engng. Trans., **57**, 3–4, 185–215, 2009.
4. DRUCKER D.C., *Plasticity Theory, Strength-Differential (SD) Phenomenon, and Volume Expansion in Metals and Plastics*, Metall. Trans., **4**, 667–673, 1973.
5. DRUCKER D.C., PRAGER W., *Soil mechanics and plastic analysis for limit design*, Quart. Appl. Math., **10**, 2, 157–165, 1952.
6. GELFAND I.M., *Lectures on Linear Algebra* [in Russian: *Lekhtsii po linyeynoy algebre*], Nauka, Moscow, 1966.
7. HILL R., *A theory of the yielding and plastic flow of anisotropic metals*, Proc. Roy. Soc. London, **193**, 281–297, 1948.
8. HOFFMAN O., *The brittle strength of orthotropic materials*, J. Comp. Mater., **1**, 200–206, 1967.
9. KOWALCZYK K., OSTROWSKA-MACIEJEWSKA J., PEŁCHERSKI R.B., *An energy-based yield criterion for solids of cubic elasticity and orthotropic limit state*, Arch. Mech., **55**, 5–6, 431–448, 2003.
10. LEXCELLENT C., VIVET A., BOUVET C., CALLOCH S., BLANC P., *Experimental and numerical determinations of the initial surface of phase transformation under biaxial loading in some polycrystalline shape-memory alloys*, J. Mech. Phys. Sol., **50**, 2717–2735, 2002.
11. MISES R. VON, *Mechanik der plastischen Formänderung von Kristallen*, Z. Angew. Math. u. Mech., **8**, 161–185, 1928.
12. OSTROWSKA-MACIEJEWSKA J., RYCHLEWSKI J., *Plane elastic and limit states in anisotropic solids*, Arch. Mech., **40**, 4, 379–386, 1988.

13. NOWAK M., OSTROWSKA-MACIEJEWSKA J., PEŁCHERSKI R.B., SZEPTYŃSKI P., *Yield criterion accounting for the third invariant of stress tensor deviator. Part I. Derivation of the yield condition basing on the concepts of energy-based hypotheses of Rychlewski and Burzyński.*, Engng. Trans., **59**, 4, 273–281, 2011.
14. PEŁCHERSKI R.B., SZEPTYŃSKI P., NOWAK M., *An extension of Burzyński hypothesis of material effort accounting for the third invariant of stress tensor*, Arch. Metall. Mat., **56**, 2, 503–508, 2011.
15. PODGÓRSKI J., *Limit state condition and the dissipation function for isotropic materials*, Arch. Mech., **36**, 3, 323–342, 1984.
16. RANIECKI B., MRÓZ Z., *Yield or martensitic phase transformation conditions and dissipation functions for isotropic, pressure-insensitive alloys exhibiting SD effect*, Acta. Mech., **195**, 81–102, 2008.
17. RYCHLEWSKI J., „*CEIHNOSSTTUV*” *Mathematical structure of elastic bodies* [in Russian], Preprint 217, IPM AN SSSR, IPPT PAN, Moscow 1983.
18. RYCHLEWSKI J., *Elastic energy decomposition and limit criteria* [in Russian], Advances in Mechanics (Uspekhi mekhaniki), 7, 51–80, 1984; see also: *Elastic energy decomposition and limit criteria*, Engng. Trans., **59**, 1, 31–63, 2011.
19. RYCHLEWSKI J., *On Hooke’s law* [in Russian], Prikl. Mat. Mekh., 48, 420–435, 1984; see also: J. Appl. Math. Mech., **48**, 303–314, 1984.
20. SPITZIG W.A., SOBER R.J., RICHMOND O., *The effect of hydrostatic pressure on the deformation behavior of maraging and HY-80 steels and its implications for plasticity theory*, Metall. Trans. A, 7A, 1703–1710, 1976.
21. SZEPTYŃSKI P., *Yield criterion accounting for the influence of the third invariant of stress tensor deviator. Part II: Analysis of convexity condition of the yield surface*, Engng. Trans., **59**, 4, 283–297, 2011.
22. SZEPTYŃSKI P., PEŁCHERSKI R.B., *Proposition of a new yield criterion for orthotropic metal sheets accounting for asymmetry of elastic range* [in Polish], Rudy i Metale Niezależne, **57**, 4, 243–250, 2012.
23. THEOCARIS P.S., *The elliptic paraboloid failure criterion for cellular solids and brittle foams*, Acta Mech., **89**, 93–121, 1991.
24. TSAI S.W., WU E.M., *A general theory of strength for anisotropic materials*, J. Comp. Mater., **5**, 58–80, 1971.

Received July 1, 2011; revised version May 5, 2012.

Velocity and Temperature Distributions Between Parallel Porous Plates with the Hall Effect and Variable Properties Under Exponential Decaying Pressure Gradient

Hazem Ali ATTIA¹⁾, Mostafa A.M. ABDEEN²⁾

¹⁾ *Fayoum University, Faculty of Engineering
Department of Engineering Mathematics and Physics
El-Fayoum-63514, Egypt
e-mail: ah1113@yahoo.com*

²⁾ *Cairo University, Faculty of Engineering
Department of Engineering Mathematics and Physics
Giza 12211, Egypt
e-mail: mostafa_a_m_abdeen@hotmail.com*

The time varying hydromagnetic flow between two infinite parallel porous plates is studied with heat transfer considering the Hall effect and temperature dependent physical properties. An exponential decaying pressure gradient is imposed in the axial direction and an external uniform magnetic field as well as a uniform suction and injection are applied perpendicular to the horizontal plates. A numerical solution for the governing non-linear coupled set of equations of motion and the energy equation is adopted. The effects of the Hall current and the temperature dependent viscosity and thermal conductivity on both the velocity and temperature distributions are investigated.

Key words: flow between parallel plates, variable properties, hydromagnetics, heat transfer, numerical solution.

1. INTRODUCTION

The flow of an electrically conducting fluid between infinite horizontal parallel plates, known as Hartmann flow, has interesting applications in magnetohydrodynamic (MHD) power generators and pumps etc. HARTMANN and LAZARUS [1] investigated the effect of a transverse uniform magnetic field on the flow of a viscous incompressible electrically conducting fluid between two infinite parallel plates. Exact solutions for the velocity fields were developed [2–5] under different physical effects. Some exact and numerical solutions for the heat transfer problem are derived in [6]. SOUNDALGEKAR *et al.* [7, 8] examined the

effect of Hall currents on the steady MHD Couette flow with heat transfer. The temperatures of the two plates were assumed constant [7] or varying along the plates in the direction of the flow [8]. ATTIA [9] examined the effect of Hall current on the velocity and temperature fields of an unsteady Hartmann flow with uniform suction and injection applied perpendicular to the plates.

In these studies the physical properties are assumed to be constant, however it is known that some physical properties are functions of temperature and assuming constant properties is a good approximation as long as small differences in temperature are involved. More accurate prediction for the flow and heat transfer can be achieved by considering the variation of the physical properties with temperature [10]. KLEMP *et al.* [11] studied the effect of temperature dependent viscosity on the entrance flow in a channel in the hydrodynamic case. ATTIA and KOTB [12] solved the steady MHD fully developed flow and heat transfer between two parallel plates with temperature dependent viscosity which has been extended to the transient state by ATTIA [13]. The influence of the dependence of the physical properties on temperature in the MHD Couette flow between parallel plates was studied [14, 15].

In this work, the unsteady Hartmann flow of a viscous incompressible electrically conducting fluid is investigated with heat transfer. The viscosity and thermal conductivity of the fluid are assumed to vary with temperature and the Hall current is considered. The fluid is flowing between two electrically insulating porous plates and is acted upon by an exponential decaying pressure gradient. A uniform suction and injection and an external uniform magnetic field are applied normal the surface of the plates. The two plates are kept at two constant but different temperatures and the viscous and Joule dissipations terms are included in the energy equation. This configuration is a good approximation of some practical situations such as heat exchangers, flow meters, and pipes that connect system components. The flow and temperature distributions of both the fluid and dust particles are governed by the coupled set of the momentum and energy equations. The coupled set of non-linear equations of motion and the energy equation are solved numerically using finite differences to determine the velocity and temperature fields.

2. FORMULATION OF THE PROBLEM

The fluid flow is between two infinite horizontal parallel plates located at the $y = \pm h$ planes. The two plates are porous, insulating and kept at two constant but different temperatures T_1 for the lower plate and T_2 for the upper one with $T_2 > T_1$. An exponential decaying pressure gradient is imposed in the axial x -direction and a uniform suction from above and injection from below, with velocity v_0 , are applied impulsively at $t = 0$. A uniform magnetic field B_0 ,

assumed unaltered, is applied perpendicular to the plates in the positive y -direction. The Hall effect is considered and accordingly, a z -component of the velocity is initiated. The viscosity and thermal conductivity of the fluid depend on temperature exponentially and linearly, respectively while the viscous and Joule dissipations are not neglected in the energy equation. The fluid motion starts from rest at $t = 0$, and the no-slip condition at the plates implies that the fluid velocity has neither a z - nor an x -component at $y = \pm h$. The initial temperature of the fluid is assumed to be equal to T_1 as the temperature of the lower plate. Since the plates are infinite in the x - and z -directions, the physical quantities do not change in these directions which leads to one-dimensional problem.

The flow of the fluid is governed by the Navier–Stokes equation

$$(2.1) \quad \rho \frac{D\mathbf{v}}{Dt} = -\nabla p + \nabla \cdot (\mu \nabla \mathbf{v}) + \mathbf{J} \wedge \mathbf{B}_0,$$

where ρ is the density of the fluid, μ is the viscosity of the fluid, \mathbf{J} is the current density, and \mathbf{v} is the velocity vector of the fluid, which is given by

$$\mathbf{v} = u(y, t)\mathbf{i} + v_0\mathbf{j} + w(y, t)\mathbf{k}.$$

If the Hall term is retained, the current density \mathbf{J} is given by the generalized Ohm's law [4]

$$(2.2) \quad \mathbf{J} = \sigma(\mathbf{v} \wedge \mathbf{B}_0 - \beta(\mathbf{J} \wedge \mathbf{B}_0)),$$

where σ is the electric conductivity of the fluid and β is the Hall factor [4]. Equation (2.2) may be solved in \mathbf{J} to yield

$$(2.3) \quad \mathbf{J} \wedge \mathbf{B}_0 = -\frac{\sigma B_0^2}{1+m^2}((u+mw)\mathbf{i} + (w-mu)\mathbf{k}),$$

where m is the Hall parameter and $m = \sigma\beta B_0$. Thus, the two components of the momentum equation (2.1) read

$$(2.4) \quad \rho \frac{\partial u}{\partial t} + \rho v_0 \frac{\partial u}{\partial y} = Ge^{-\alpha t} + \mu \frac{\partial^2 u}{\partial y^2} + \frac{\partial \mu}{\partial y} \frac{\partial u}{\partial y} - \frac{\sigma B_0^2}{1+m^2}(u+mw),$$

$$(2.5) \quad \rho \frac{\partial w}{\partial t} + \rho v_0 \frac{\partial w}{\partial y} = \mu \frac{\partial^2 w}{\partial y^2} + \frac{\partial \mu}{\partial y} \frac{\partial w}{\partial y} - \frac{\sigma B_0^2}{1+m^2}(w-mu).$$

It is assumed that the pressure gradient is applied at $t = 0$ and the fluid starts its motion from rest. Thus

$$(2.6)_1 \quad t = 0: u = w = 0.$$

For $t > 0$, the no-slip condition at the plates implies that

$$(2.6)_2 \quad y = -h: u = w = 0,$$

$$(2.6)_3 \quad y = h: u = w = 0.$$

The energy equation describing the temperature distribution for the fluid is given by [15]

$$(2.7) \quad \rho c_p \frac{\partial T}{\partial t} + \rho c_p v_0 \frac{\partial T}{\partial y} = \frac{\partial}{\partial y} \left(k \frac{\partial T}{\partial y} \right) + \mu \left[\left(\frac{\partial u}{\partial y} \right)^2 + \left(\frac{\partial w}{\partial y} \right)^2 \right] + \frac{\sigma B_0^2}{1 + m^2} (u^2 + w^2),$$

where T is the temperature of the fluid, c_p is the specific heat at constant pressure of the fluid, and k is thermal conductivity of the fluid. The last two terms in the right side of Eq. (2.7) represent the viscous and Joule dissipations respectively.

The temperature of the fluid must satisfy the initial and boundary conditions,

$$(2.8) \quad \begin{aligned} t = 0: T &= T_1, \\ t > 0: T &= T_1, \quad y = -h, \\ t > 0: T &= T_2, \quad y = h. \end{aligned}$$

The viscosity of the fluid is assumed to vary with temperature and is defined as, $\mu = \mu_0 f_1(T)$. By assuming the viscosity to vary exponentially with temperature, the function $f_1(T)$ takes the form [7], $f_1(T) = \exp(-a_1(T - T_1))$. In some cases a_1 may be negative, i.e. the coefficient of viscosity increases with temperature [7, 15]. Also the thermal conductivity of the fluid is varying with temperature as $k = k_0 f_2(T)$. We assume linear dependence for the thermal conductivity upon the temperature in the form $k = k_0[1 + b_1(T - T_1)]$ [16], where the parameter b_1 may be positive or negative [16].

Introducing the following non-dimensional quantities,

$$\begin{aligned} (\hat{x}, \hat{y}, \hat{z}) &= \frac{(x, y, z)}{h}, & \hat{t} &= \frac{t \mu_0}{\rho h^2}, \\ \hat{G} &= \frac{\rho G}{h^2 \mu_0^2}, & (\hat{u}, \hat{w}) &= \frac{(u, w) \rho h}{\mu_0}, \\ \theta &= \frac{T - T_1}{T_2 - T_1}, \end{aligned}$$

where

$$\widehat{f}_1(\theta) = e^{-a_1(T_2-T_1)\theta} = e^{-a\theta}, \quad a \text{ is the viscosity variation parameter,}$$

$$\widehat{f}_2(\theta) = 1 + b_1(T_2 - T_1)\theta = 1 + b\theta, \quad b \text{ is the thermal conductivity variation parameter,}$$

$$S = \rho v_0 h / \mu_0 \text{ is the suction parameter,}$$

$$\text{Ha}^2 = \sigma B_0^2 h^2 / \mu_0, \text{ Ha is the Hartmann number,}$$

$$\text{Pr} = \mu_0 c_p / k_0 \text{ is the Prandtl number,}$$

$$\text{Ec} = \mu_0^2 / h^2 c_p \rho^2 (T_2 - T_1) \text{ is the Eckert number.}$$

Equations (2.4) to (2.8) read (the hats are dropped for simplicity)

$$(2.9) \quad \frac{\partial u}{\partial t} + S \frac{\partial u}{\partial y} = Ge^{-\alpha t} + f_1(\theta) \frac{\partial^2 u}{\partial y^2} + \frac{\partial f_1(\theta)}{\partial y} \frac{\partial u}{\partial y} - \frac{\text{Ha}^2}{1+m^2}(u+mw),$$

$$(2.10) \quad \frac{\partial w}{\partial t} + S \frac{\partial w}{\partial y} = f_1(\theta) \frac{\partial^2 w}{\partial y^2} + \frac{\partial f_1(\theta)}{\partial y} \frac{\partial w}{\partial y} - \frac{\text{Ha}^2}{1+m^2}(w-mu),$$

$$t = 0: \quad u = w = 0,$$

$$(2.11) \quad t > 0: \quad y = -1, \quad u = w = 0,$$

$$t > 0: \quad y = 1, \quad u = w = 0,$$

$$(2.12) \quad \frac{\partial \theta}{\partial t} + S \frac{\partial \theta}{\partial y} = \frac{1}{\text{Pr}} f_2(\theta) \frac{\partial^2 \theta}{\partial y^2} + \frac{1}{\text{Pr}} \frac{\partial f_2(\theta)}{\partial y} \frac{\partial \theta}{\partial y} \\ + \text{Ec} f_1(\theta) \left[\left(\frac{\partial u}{\partial y} \right)^2 + \left(\frac{\partial w}{\partial y} \right)^2 \right] + \frac{\text{Ec} \text{Ha}^2}{1+m^2}(u^2+w^2),$$

$$t = 0: \quad \theta = 0,$$

$$(2.13) \quad t > 0: \quad \theta = 0, \quad y = -1,$$

$$t > 0: \quad \theta = 1, \quad y = 1.$$

Equations (2.9), (2.10), and (2.12) represent a system of coupled non-linear partial differential equations which are solved numerically under the initial and boundary conditions (2.11) and (2.13) using the method of finite differences. A linearization technique is first applied to replace the nonlinear terms at a linear stage, with the corrections incorporated in subsequent iterative steps until convergence is reached. Then the Crank–Nicolson implicit method is used at two successive time levels [17]. An iterative scheme is used to solve the linearized system of difference equations. The solution at a certain time step is chosen as an initial guess for next time step and the iterations are continued till convergence,

within a prescribed accuracy. Finally, the resulting block tridiagonal system is solved using the generalized Thomas-algorithm [17]. Finite difference equations relating the variables are obtained by writing the equations at the mid point of the computational cell and then replacing the different terms by their second order central difference approximations in the y -direction. The diffusion terms are replaced by the average of the central differences at two successive time-levels. The computational domain is divided into meshes each of dimension Δt and Δy in time and space, respectively. We define the variables $A = \partial u / \partial y$, $B = \partial w / \partial y$ and $H = \partial \theta / \partial y$ to reduce the second order differential equations (2.9), (2.10) and (2.12) to first-order differential equations which take the form

$$\begin{aligned}
 (2.14) \quad & \left(\frac{u_{i+1,j+1} - u_{i,j+1} + u_{i+1,j} - u_{i,j}}{2} \right) + S \left(\frac{A_{i+1,j+1} + A_{i,j+1} + A_{i+1,j} + A_{i,j}}{4} \right) \\
 & = G \exp \left[-\alpha \left(\frac{t_{i+1} + t_i}{2} \right) \right] + \left(\frac{\bar{f}_1(\theta)_{i,j+1} + \bar{f}_1(\theta)_{i,j}}{2} \right) \\
 & \cdot \left(\frac{(A_{i+1,j+1} + A_{i,j+1}) - (A_{i+1,j} + A_{i,j})}{2\Delta y} \right) + \left(\frac{\bar{f}_1(\theta)_{i,j+1} - \bar{f}_1(\theta)_{i,j}}{\Delta y} \right) \\
 & \cdot \left(\frac{A_{i+1,j+1} + A_{i,j+1} + A_{i+1,j} + A_{i,j}}{4} \right) \\
 & - \frac{\text{Ha}^2}{1+m^2} \left(\frac{u_{i+1,j+1} + u_{i,j+1} + u_{i+1,j} + u_{i,j}}{4} \right) \\
 & - \frac{m\text{Ha}^2}{1+m^2} \left(\frac{w_{i+1,j+1} + w_{i,j+1} + w_{i+1,j} + w_{i,j}}{4} \right),
 \end{aligned}$$

$$\begin{aligned}
 (2.15) \quad & \left(\frac{w_{i+1,j+1} - w_{i,j+1} + w_{i+1,j} - w_{i,j}}{2} \right) + S \left(\frac{B_{i+1,j+1} + B_{i,j+1} + B_{i+1,j} + B_{i,j}}{4} \right) \\
 & = \left(\frac{\bar{f}_1(\theta)_{i,j+1} + \bar{f}_1(\theta)_{i,j}}{2} \right) \left(\frac{(B_{i+1,j+1} + B_{i,j+1}) - (B_{i+1,j} + B_{i,j})}{2\Delta y} \right) \\
 & + \left(\frac{\bar{f}_1(\theta)_{i,j+1} - \bar{f}_1(\theta)_{i,j}}{\Delta y} \right) \left(\frac{B_{i+1,j+1} + B_{i,j+1} + B_{i+1,j} + B_{i,j}}{4} \right) \\
 & - \frac{\text{Ha}^2}{1+m^2} \left(\frac{w_{i+1,j+1} + w_{i,j+1} + w_{i+1,j} + w_{i,j}}{4} \right) \\
 & + \frac{m\text{Ha}^2}{1+m^2} \left(\frac{u_{i+1,j+1} + u_{i,j+1} + u_{i+1,j} + u_{i,j}}{4} \right),
 \end{aligned}$$

$$\begin{aligned}
(2.16) \quad & \left(\frac{\theta_{i+1,j+1} - \theta_{i,j+1} + \theta_{i+1,j} - \theta_{i,j}}{2\Delta t} \right) + S \left(\frac{H_{i+1,j+1} + H_{i,j+1} + H_{i+1,j} + H_{i,j}}{4} \right) \\
& = \left(\frac{\bar{f}_2(\theta)_{i,j+1} + \bar{f}_2(\theta)_{i,j}}{2\text{Pr}} \right) \left(\frac{(H_{i+1,j+1} + H_{i,j+1}) - (H_{i+1,j} + H_{i,j})}{2\Delta y} \right) \\
& \quad + \left(\frac{\bar{f}_2(\theta)_{i,j+1} - \bar{f}_2(\theta)_{i,j}}{\Delta y} \right) \left(\frac{H_{i+1,j+1} + H_{i,j+1} + H_{i+1,j} + H_{i,j}}{4\text{Pr}} \right) \\
& - \text{Ec} \left(\frac{\bar{f}_1(\theta)_{i,j+1} + \bar{f}_1(\theta)_{i,j}}{2} \right) \left(\frac{(\bar{A}_{i+1,j+1} + \bar{A}_{i,j+1} + \bar{A}_{i+1,j} + \bar{A}_{i,j})}{2} \right) \\
& \quad \cdot \left(\frac{A_{i+1,j+1} + A_{i,j+1} + A_{i+1,j} + A_{i,j}}{2} \right) \\
& + \text{Ec} \left(\frac{\bar{f}_1(\theta)_{i,j+1} + \bar{f}_1(\theta)_{i,j}}{2} \right) \left(\frac{(\bar{B}_{i+1,j+1} + \bar{B}_{i,j+1} + \bar{B}_{i+1,j} + \bar{B}_{i,j})}{2} \right) \\
& \quad \cdot \left(\frac{B_{i+1,j+1} + B_{i,j+1} + B_{i+1,j} + B_{i,j}}{2} \right) \\
& \quad + \frac{\text{Ec Ha}^2}{1+m^2} \left(\frac{\bar{u}_{i+1,j+1} + \bar{u}_{i,j+1} + \bar{u}_{i+1,j} + \bar{u}_{i,j}}{2} \right) \\
& \quad \cdot \left(\frac{u_{i+1,j+1} + u_{i,j+1} + u_{i+1,j} + u_{i,j}}{2} \right) \\
& \quad + \frac{\text{Ec Ha}^2}{1+m^2} \left(\frac{\bar{w}_{i+1,j+1} + \bar{w}_{i,j+1} + \bar{w}_{i+1,j} + \bar{w}_{i,j}}{2} \right) \\
& \quad \cdot \left(\frac{w_{i+1,j+1} + w_{i,j+1} + w_{i+1,j} + w_{i,j}}{2} \right).
\end{aligned}$$

The variables with bars are given initial guesses from the previous time steps and an iterative scheme is used at every time to solve the linearized system of difference equations. All calculations have been carried out for the non-dimensional variables and parameters given by: $G = 5$, $\alpha = 1$, $\text{Pr} = 1$, and $\text{Ec} = 0.2$. Grid-independence studies show that the computational domain $0 < t < \infty$ and $-1 < y < 1$ can be divided into intervals with step sizes $\Delta t = 0.0001$ and $\Delta y = 0.005$ for time and space respectively. Smaller step sizes do not show any significant change in the results. Convergence of the scheme is assumed when all of the unknowns u , w , A , B , θ and H for the last two approximations differ from unity by less than 10^{-6} for all values of y in $-1 < y < 1$ at every time step. Less than 7 approximations are required to satisfy this convergence criteria for all ranges of the parameters studied here.

3. RESULTS AND DISCUSSION

Figure 1 show the time development of the profiles of the velocity and temperature for $Ha = 1$, $m = 3$, $S = 0$, $a = 0.5$ and $b = 0.5$. The velocity and temperature distributions do not reach steady state monotonically as shown in figure. They increase with time up till a maximum value and then decrease up to the steady state under the effect of the decaying pressure gradient. The velocity component u reaches steady state faster than w which, in turn, reaches steady state faster than θ . This is expected as u is the source of w , while both u and w are sources of θ .

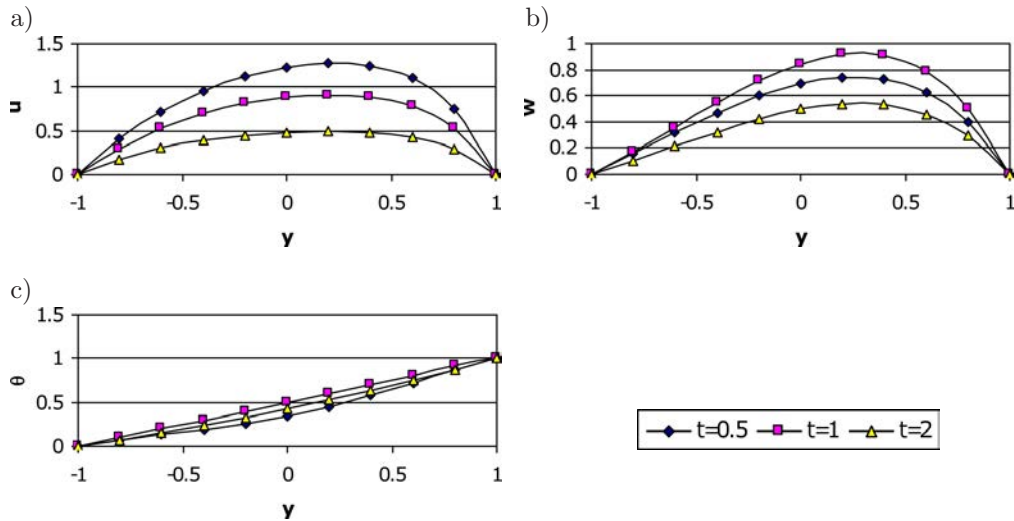


FIG. 1. The evolution of the profile of: a) u ; b) w ; c) θ ($Ha = 3$, $m = 3$, $S = 1$, $a = 0.5$, $b = 0.5$).

Figure 2 presents the time progression of the velocity component u at the centre of the channel ($y = 0$) for different values of m and a and for $b = 0$, $S = 0$ and $Ha = 3$. The figure indicates that u increases with m for all values of a which can be attributed to the fact that an increment in m decreases the effective conductivity ($\sigma/(1 + m^2)$) and then decreases the magnetic resistive force. The figure depicts also that the effect of a on u depends on the parameter m and becomes more clear for higher m .

Figure 3 shows the time progression of the velocity component w at the centre of the channel ($y = 0$) for different values of m and a and for $b = 0$, $S = 0$ and $Ha = 3$. The figure indicates that w increases with increasing m for all values of a as w is a result of the Hall effect. Although the Hall current is the source for w , Fig. 3 shows that, at small times, for large values of m , an increase in m produces a decrease in w . This can be understood by discussing the term

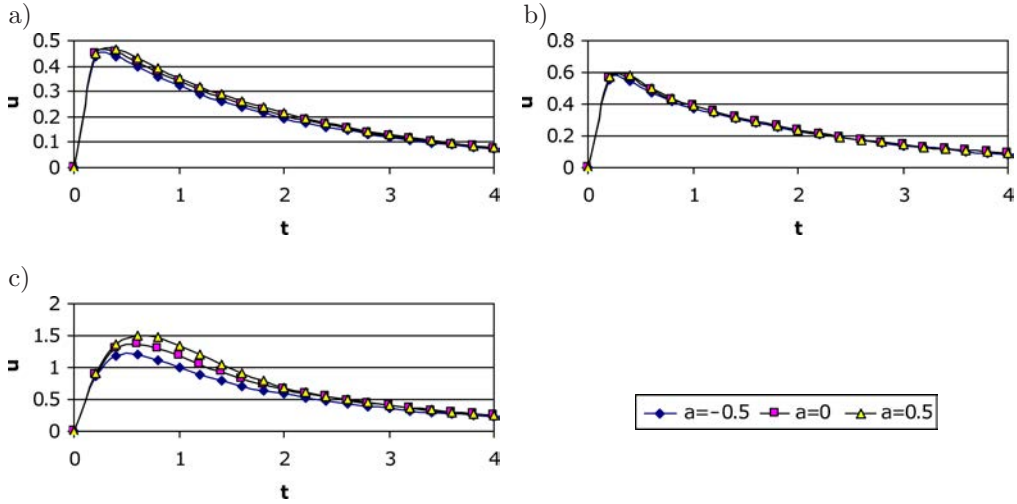


FIG. 2. The evolution of u at $y = 0$ for various values of a and m :
 a) $m = 0$; b) $m = 1$; c) $m = 5$ ($Ha = 3, S = 0, b = 0$).

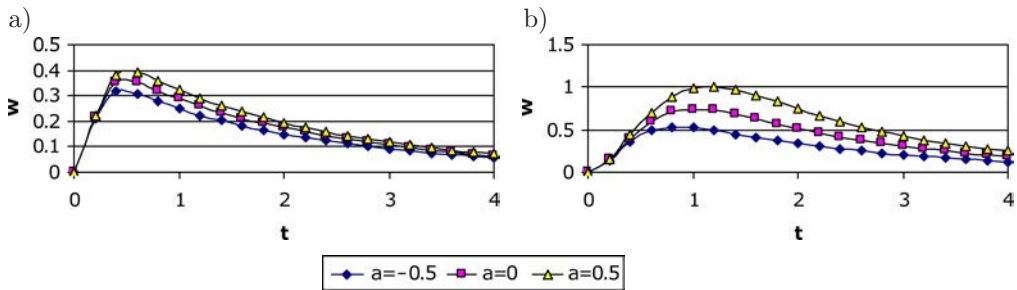


FIG. 3. The evolution of w at $y=0$ for various values of a and m :
 a) $m = 1$; b) $m = 5$ ($Ha = 3, S = 0, b = 0$).

$(-(w - mu)/(1 + m^2))$ in Eq. (2.10), which is the source term of w . At small times w is very small and this term may be approximated to $(mu/(1 + m^2))$, which decreases with increasing m if $m > 1$. Figure 3 presents also that the time required for w to reach its steady state value increases with increasing m and that w and its steady state time increase as a result of increasing a .

Figure 4 shows the time progression of the temperature θ at the centre of the channel for different values of m and a when $b = 0$ and $Ha = 3$. The variation of θ with m is shown to depend on t . When $m > 1$, increasing m decreases θ slightly at small times but increases θ at large times. This is because when t is small, u and w are small and an increment in m results in an increase in u but a decrease in w , so the Joule dissipation which is proportional also to $(1/(1 + m^2))$ decreases. When t is large, u and w increase with increasing m

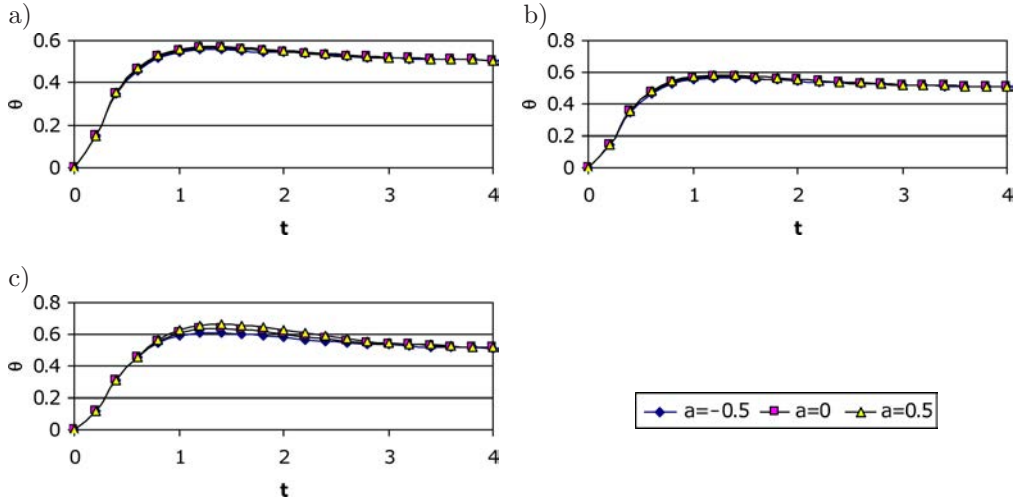


FIG. 4. The evolution of θ at $y = 0$ for various values of a and m :
 a) $m = 0$; b) $m = 1$; c) $m = 5$ ($Ha = 3, S = 0, b = 0$).

and so do the Joule and viscous dissipations. It is difficult to predict the effect of a on θ , because while increasing a increases the velocities and the velocity gradients, it decreases the function f_1 . All the same, Fig. 4 shows that increasing a increases θ and its effect is more apparent for higher values of m .

Figure 5 shows the time progression of θ at the centre of the channel for different values of m and b when $a = 0, S = 0$ and $Ha = 3$. The figure indicates that increasing b increases θ and its steady state time for all m . This occurs as

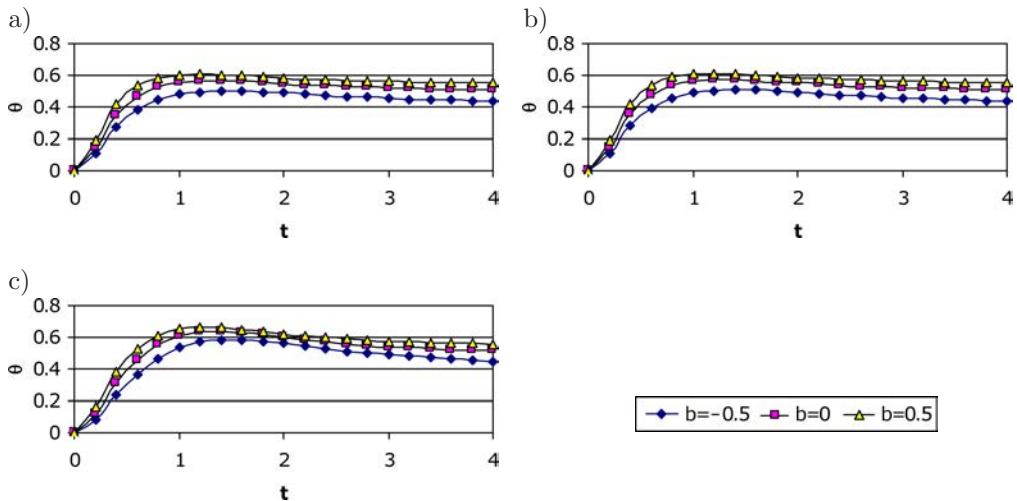


FIG. 5. The evolution of θ at $y = 0$ for various values of b and m :
 a) $m = 0$; b) $m = 1$; c) $m = 5$ ($Ha = 3, S = 0, a = 0$).

the centre of the channel acquires heat by conduction from the upper hot plate. The parameter b has no significant effect on u or w in spite of the coupling between the momentum and energy equations as depicted in figure.

Table 1 shows the dependence of the steady state temperature at the centre of the channel on a and m for $b = 0$ and $S = 0$. It is observed that θ increases with increasing m or a , as increasing m decreases damping forces and increasing a decreases viscosity. Both effects increase u , w and their gradients and hence the dissipations. Table 2 shows the variation of θ at the centre of the channel with m and b for $a = 0$, $S = 0$ and $Ha = 1$. The dependence of θ on m is explained by the same argument used in discussing Table 1. Table 2 indicates that increasing b increases θ since the centre acquires temperature by conduction from the upper hot plate. Table 3 presents the variation of θ with a and b for

Table 1. Variation of the steady state temperature θ at $y = 0$ for various values of m and a ($Ha = 1$, $b = 0$).

θ	$m = 0.0$	$m = 0.5$	$m = 1.0$	$m = 3.0$	$m = 5.0$
$a = -0.5$	0.5142	0.5144	0.5146	0.5152	0.5153
$a = -0.1$	0.5179	0.5183	0.5189	0.5201	0.5204
$A = 0.0$	0.5191	0.5195	0.5201	0.5271	0.5221
$A = 0.1$	0.5203	0.5207	0.5216	0.5235	0.5239
$A = 0.5$	0.5261	0.5269	0.5286	0.5333	0.5345

Table 2. Variation of the steady state temperature θ at $y = 0$ for various values of m and b ($Ha = 1$, $a = 0$).

θ	$m = 0.0$	$m = 0.5$	$m = 1.0$	$m = 3.0$	$m = 5.0$
$b = -0.5$	0.4562	0.4568	0.4579	0.4605	0.4611
$b = -0.1$	0.5077	0.5081	0.5089	0.5106	0.5109
$B = 0.0$	0.5191	0.5195	0.5201	0.5217	0.5221
$B = 0.1$	0.5295	0.5298	0.5304	0.5319	0.5322
$B = 0.5$	0.5609	0.5611	0.5616	0.5626	0.5628

Table 3. Variation of the steady state temperature θ at $y = 0$ for various values of a and b ($Ha = 1$, $m = 3$).

θ	$a = -0.5$	$a = -0.1$	$a = 0.0$	$a = 0.1$	$a = 0.5$
$b = -0.5$	0.4593	0.4579	0.4605	0.4634	0.4792
$b = -0.1$	0.5035	0.5089	0.5106	0.5125	0.5232
$B = 0.0$	0.5152	0.5201	0.5217	0.5235	0.5333
$B = 0.1$	0.5258	0.5304	0.5319	0.5335	0.5426
$B = 0.5$	0.5580	0.5615	0.5626	0.5639	0.5707

large and small values of Ha and for large and small values of m and for $Ha = 1$ and $m = 3$. Increasing a or b increases θ as explained above.

Figures 6, 7, and 8 show the time progression of the velocity components u and w and the temperature θ , respectively, at the centre of the channel ($y = 0$) for different values of S and a when $Ha = 3$, $m = 3$, and $b = 0$. Figures 6 and 7 show that increasing S decreases both u and w for all a due to the convection of the fluid from regions in the lower half to the centre which has higher fluid

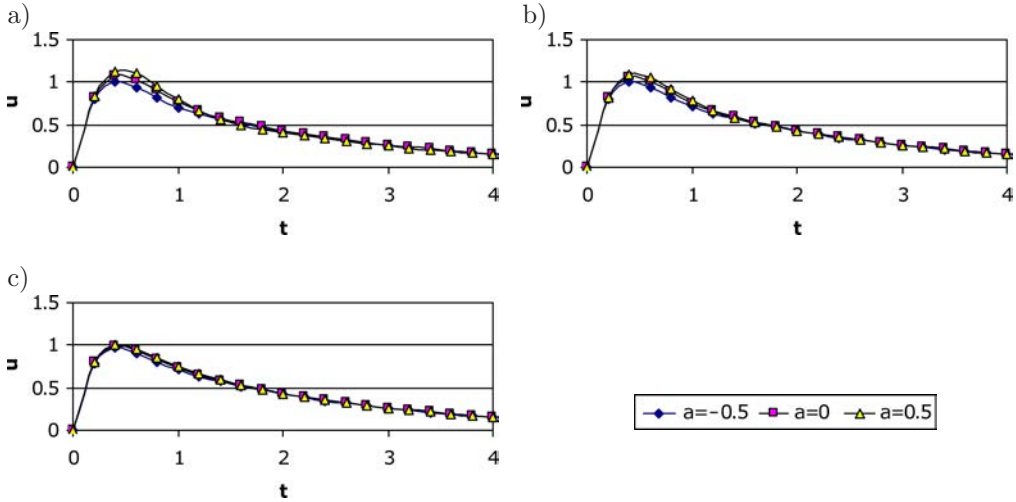


FIG. 6. The evolution of u at $y = 0$ for various values of a and S :
 a) $S = 0$; b) $S = 1$; c) $S = 2$ ($Ha = 3$, $m = 3$, $b = 0$).

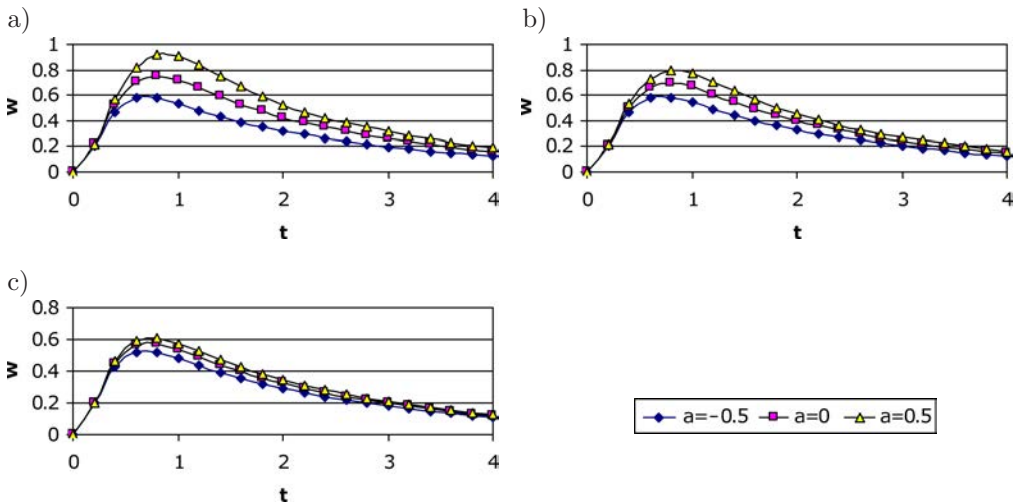


FIG. 7. The evolution of w at $y = 0$ for various values of a and S :
 a) $S = 0$; b) $S = 1$; c) $S = 2$ ($Ha = 3$, $m = 3$, $b = 0$).

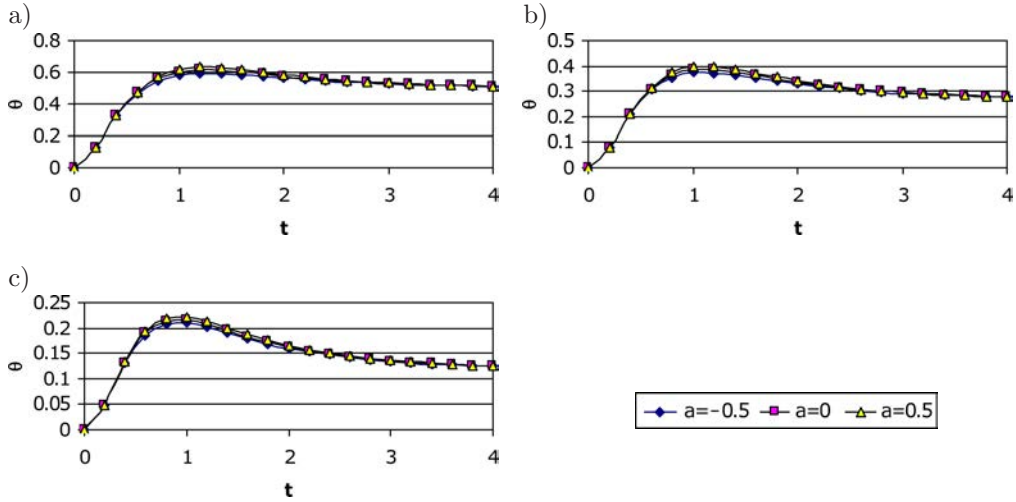


FIG. 8. The evolution of θ at $y = 0$ for various values of a and S :
 a) $S = 0$; b) $S = 1$; c) $S = 2$ ($Ha = 3$, $m = 3$, $b = 0$).

speed. It is also indicated that the influence of the parameter a on u and w becomes more apparent for lower values of the parameter S . Figure 8 indicates that increasing the suction parameter decreases the temperature θ for all a as a result of the influence of convection in pumping the fluid from the cold lower half towards the centre of the channel.

Figure 9 shows the evolution of the temperature θ at the centre of the channel ($y = 0$) for different values of S and b when $Ha = 3$, $m = 3$, and $a = 0$. The figure

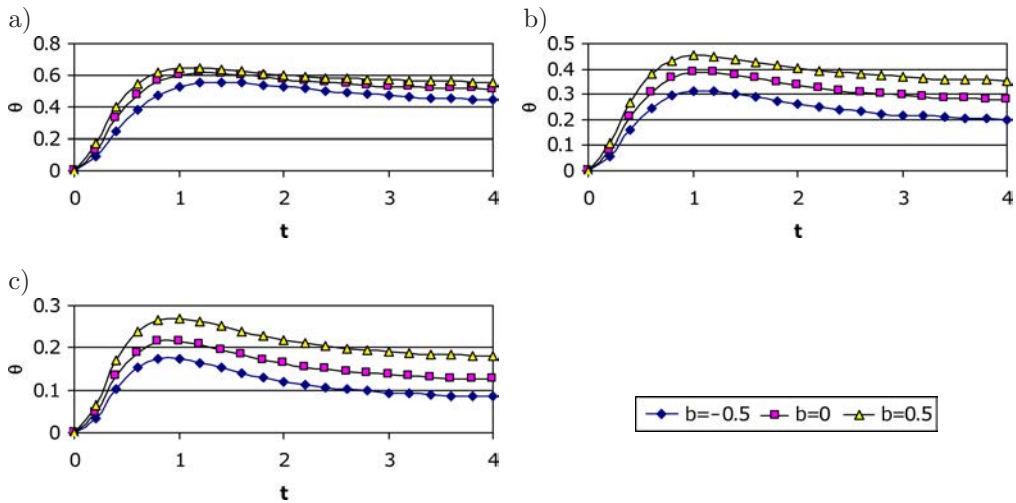


FIG. 9. The evolution of θ at $y = 0$ for various values of b and S :
 a) $S = 0$; b) $S = 1$; c) $S = 2$ ($Ha = 3$, $m = 3$, $a = 0$).

indicates that increasing S decreases θ for all b . Figure 9a shows that, for $S = 0$, the variation of θ with the parameter b depends on time as shown before in Fig. 5c for higher values of the Hall parameter m . Figures 9b and 9c present an interesting effect for the suction parameter in the suppression of the crossover points of the $\theta - t$ graph corresponding to various values of b . It is also seen that the effect of increasing the parameter b on θ is more pronounced for higher values of suction velocity.

4. CONCLUSIONS

The time varying MHD flow between two parallel plates was investigated considering the Hall current. The viscosity and thermal conductivity of the fluid are assumed to be temperature dependent. The effects of the Hartmann number Ha , the Hall parameter m , the viscosity variation parameter a and the thermal conductivity variation parameter b on the velocity and temperature fields at the centre of the channel are discussed. Introducing the Hall term gives rise to a velocity component w in the z -direction and affects the main velocity u in the x -direction. It is found that the parameter a has a marked effect on the velocity components u and w for all values of m . However, the parameter b has no significant effect on u or w . The results show that the effect of the parameter m on θ depends on t . For small time t , θ decreases with increasing m , but when t is large, or at steady state, θ increases with increasing m . The effect of the parameter m on the steady state time is ignored.

REFERENCES

1. HARTMANN J., LAZARUS F., *Kgl. Danske Videnskab. Selskab, Mat.-Fys. Medd.*, **15**, 6-7, 1937.
2. TAO L.N., *Magnetohydrodynamic effects on the formation of Couette flow*, *Journal of Aerospace Sci.*, **27**, 334, 1960.
3. ALPHER R.A., *Heat transfer in magnetohydrodynamic flow between parallel plates*, *International Journal of Heat and Mass Transfer*, **3**, 108, 1961.
4. SUTTON G.W., SHERMAN A., *Engineering Magnetohydrodynamics*, McGraw-Hill, 1965.
5. CRAMER K., PAI S., *Magnetofluid dynamics for engineers and applied physicists*, McGraw-Hill, 1973.
6. NIGAM S.D., SINGH S.N., *Heat transfer by laminar flow between parallel plates under the action of transverse magnetic field*, *Quart. J. Mech. Appl. Math.*, **13**, 85, 1960.
7. SOUNDALGEKAR V.M., VIGNHESAM N.V., TAKHAR H.S., *Hall and ion-slip effects in MHD Couette flow with heat transfer*, *IEEE Transactions on Plasma Sciences*, **PS-7**, 3, 1979.
8. SOUNDALGEKAR V.M., UPLEKAR A.G., *Hall effects in MHD Couette flow with heat transfer*, *IEEE Transactions on Plasma Science*, **PS-14**, 5, 1986.

9. ATTIA H.A., *Hall current effects on the velocity and temperature fields of an unsteady Hartmann flow*, Can. J. Phys., **76**, 739–746, 1998.
10. HERWIG H., WICKEN G., *The effect of variable properties on laminar boundary layer flow*, Wärme-und Stoffübertragung, **20**, 47–57, 1986.
11. KLEMP K., HERWIG H., SELMANN M., *Entrance flow in channel with temperature dependent viscosity including viscous dissipation effects*, Proceedings of the Third International Congress of Fluid Mechanics, Cairo, Egypt, **3**, 1257–1266, 1990.
12. ATTIA H.A., KOTB N.A., *MHD flow between two parallel plates with heat transfer*, Acta Mechanica, **117**, 215–220, 1996.
13. ATTIA H.A., *Transient MHD flow and heat transfer between two parallel plates with temperature dependent viscosity*, Mechanics Research Communications, **26**, 1, 115–121, 1999.
14. ZUECO J., EGUÍA P., GRANADA E., MÍGUEZ J.L., BEG O.A., *An electrical network for the numerical solution of transient MHD Couette flow of a dusty fluid: effects of variable properties and Hall current*, Int. Comm. Heat and Mass Trans., **37**, 10, 1432–1439, 2010.
15. EGUÍA P., ZUECO J., GRANADA E., PATIO D., *NSM solution for unsteady MHD Couette flow of a dusty conducting fluid with variable viscosity and electric conductivity*, Applied Mathematical Modelling, **35**, 303–316, 2011.
16. WHITE M.F., *Viscous fluid flow*, McGraw-Hill, 1991.
17. AMES W.F., *Numerical solutions of partial differential equations*, Second ED., Academic Press, New York, 1977.

Received September 12, 2011; revised version July 4, 2012.

Stress Analysis in Structural Components of the Koepe Pulley in Hoisting Installations

Stanisław WOLNY, Sławomir BADURA

*AGH University of Science and Technology
Faculty of Mechanical Engineering and Robotics*

Al. Mickiewicza 30, 30-059, Kraków, Poland
e-mail: {stwolny, sbadura}@agh.edu.pl

Hoisting installations in mines have been constructed and operated for many years, yet they still merit a rigorous research to identify all factors that would enable us to improve their performance parameters. A Koepe pulley in a winding system is a complex structural component, made of plates, shells, discs, membranes, radial or circumferential fin elements varying in their actual layout, depending on the design.

The strength analysis of a Koepe pulley in a hoisting system is carried out to get a better insight into the state of stress experienced by pulley components under the operational loads and to find the extreme values of the stress components, which underlies the fatigue endurance and life assessments.

Accordingly, the stress analysis of pulley elements is performed by the numerical methods, utilising the FEM approach. Models are developed using the program “FEMAP” and the stress analysis uses the package “NE”/“Nastran for Windows”.

The numerical data are then verified through strain (stress) measurements taken on a real object, under the typical operating conditions.

Key words: mine hoist, Koepe pulley, dynamics, stress.

1. INTRODUCTION

Koepe pulley and other assemblies of the hoisting installations (conveyances, suspensions of conveyances and hoisting ropes) are spatial structures incorporating various elements in the shape of beams, discs, panels or shell structures exhibiting an intricate outer edge configuration, and having apertures, mostly circular in shape, to fix ropes and the components of the guiding system [1, 2]. Finding the stress distribution and stress concentration factors in those elements becomes a complicated problem involving the theory of elasticity whilst under the mining laws currently in force these components are to be dimensioned by

the admissible stress method, taking into account the maximal static loads experienced when in service.

Stress values calculated in characteristic cross-sections of these constructions and based on fundamental formulas and calculation schemes (rods under tension, free-ends beams) are compared with admissible stress levels defined in line with safety factors as required by the relevant mining laws [1].

However, our knowledge of the actual state of stress generated in Koepe pulley components is far from complete and hence forecasting their service life seems problematic, if not wholly impossible.

That is why the endurance analysis is performed of Koepe pulley components using the numerical methods and taking into account the real service loads.

The results are verified by comparing the numerical data to measurements taken on a real object. Stress and strain is measured at the points that experienced the maximal effort, as revealed by the numerical results.

2. ENDURANCE ANALYSIS OF A KOEPE PULLEY IN A HOISTING SYSTEM

Endurance analysis is performed of a Koepe pulley in a hoisting installation shown schematically in Fig 1. The key operational parameters of the hoisting installation are summarised in Table 1.

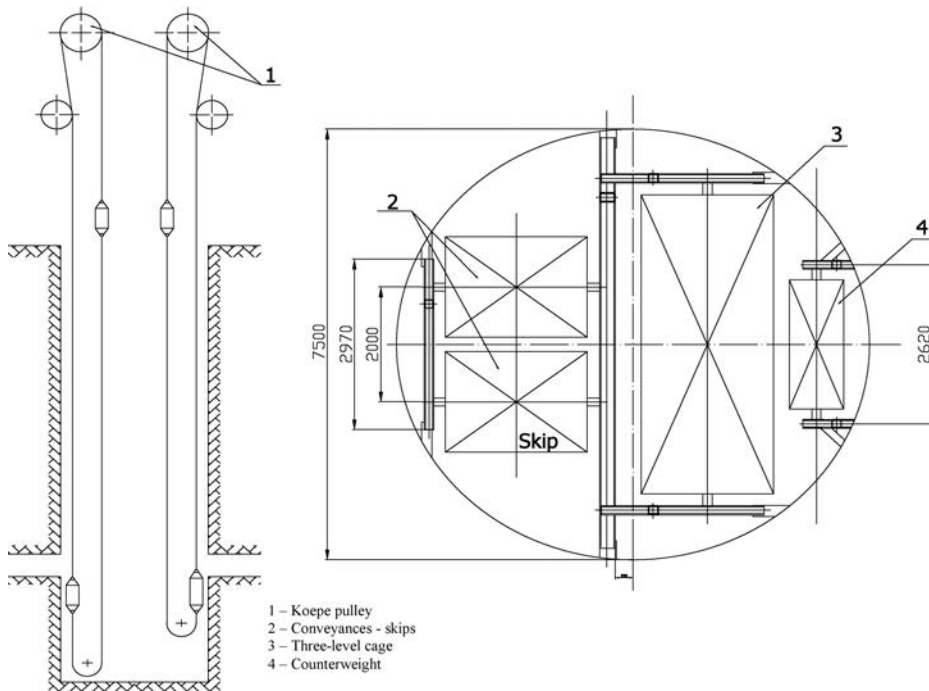


FIG. 1. Schematic diagram of the hoisting installation.

Table 1. Operational parameters of the hoisting installation used in the experiment.

Type	4L-4000/2900
Applied power /dc motor	2900 [kW]
Nominal rpm	77 rpm
Maximal skip velocity	$V = 16$ [m/s]
Conveyance and suspension	$mku = 16500$ [kg]
Payload	$\mu = 17000$ [kg]

The schematic diagram of the Koepe pulley is shown in Fig 2.

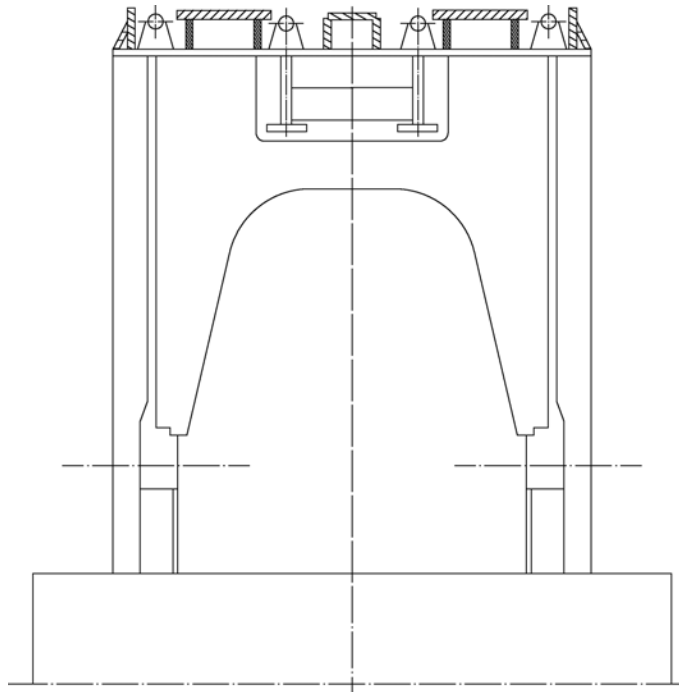


FIG. 2. Schematic diagram of the Koepe pulley.

The Koepe pulley has the major load-bearing elements (Fig. 3):

- a) short radial fins,
- b) side disc,
- c) hub,
- d) shaft,
- e) circumferential rings,
- f) mantle.

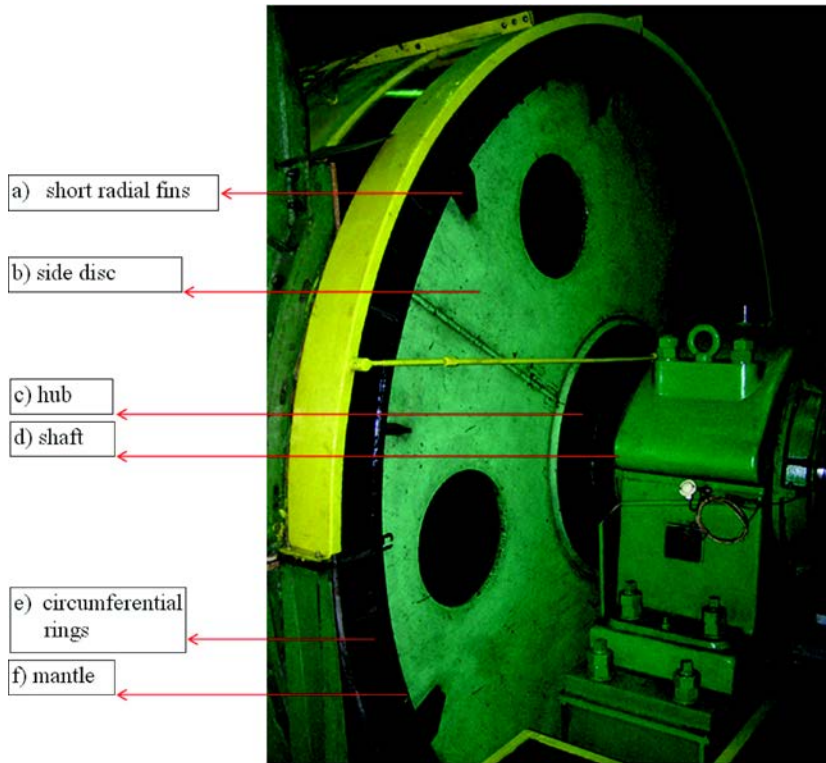


FIG. 3. Drum construction.

The Koepe pulley is a welded structure, made of steel grade St3S. The load is imposed by forces acting in hoisting ropes at the points they slid on and off the pulley during the normal duty cycle, derived from the dynamic analysis [3] verified by force measurements taken on a real object. Models are developed using the program “FEMAP” and the stress analysis uses the package “NE/Nastran for Windows”. The numerical model uses 2D and 3D elements.

2.1. Calculation model

To find the strain values and the state of stress in particular elements of the Koepe pulley, a numerical model is developed to capture the geometry of the tested structure (Fig. 4). The numerical model uses 2D and 3D (solid) elements.

The endurance analysis uses the package “NE/Nastran for Windows”. Models are developed using the program “FEMAP”. The model of the external part of the Koepe pulley (side discs, mantle, brake linings) is shown in Fig. 5, also revealing the shapes and layout of radial and circumferential fins. Figure 6 shows the positions of inspection opening reinforcements, the hub and the shaft.

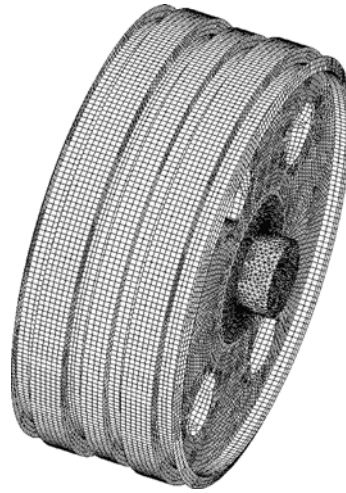


FIG. 4. Numerical model of the Koepe pulley.

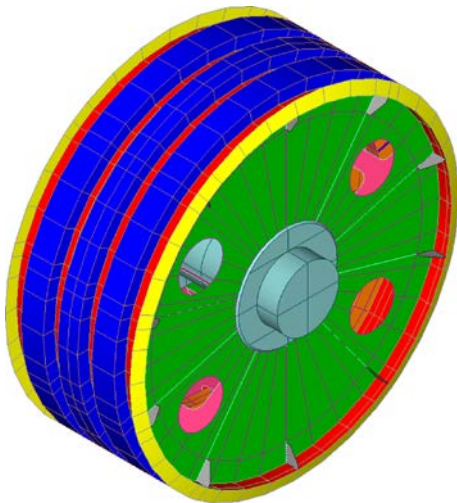


FIG. 5. Model of the drum 4L-4000/2900.

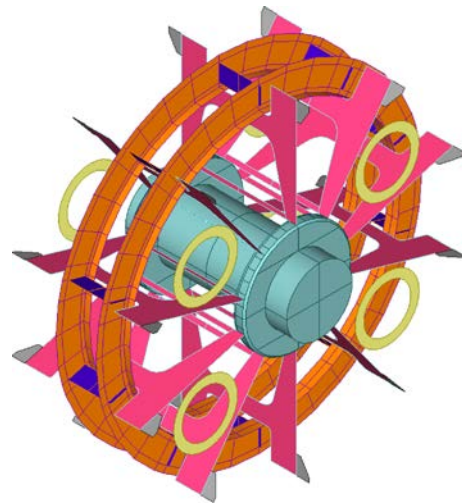
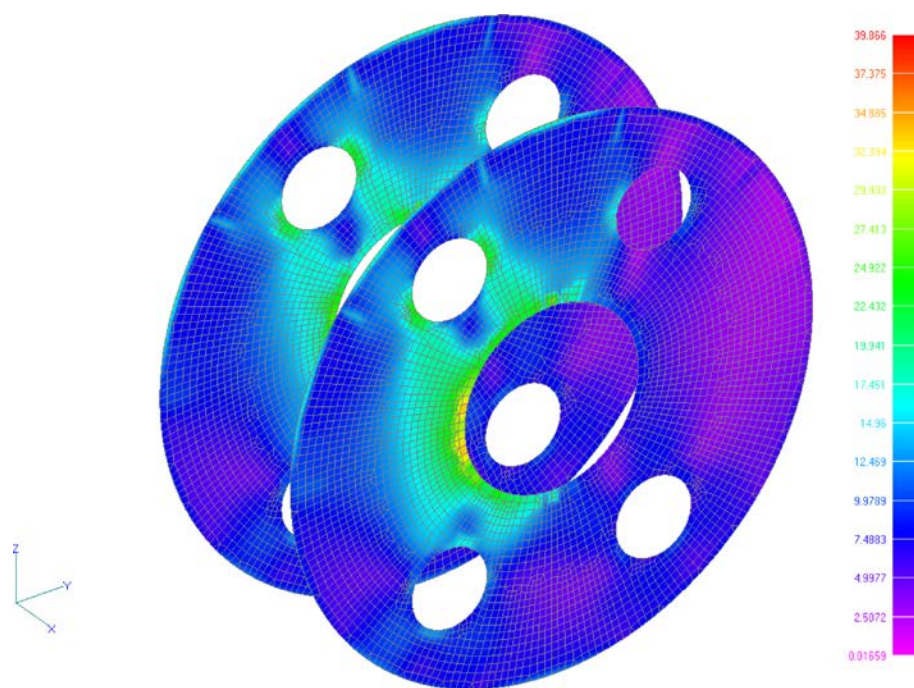
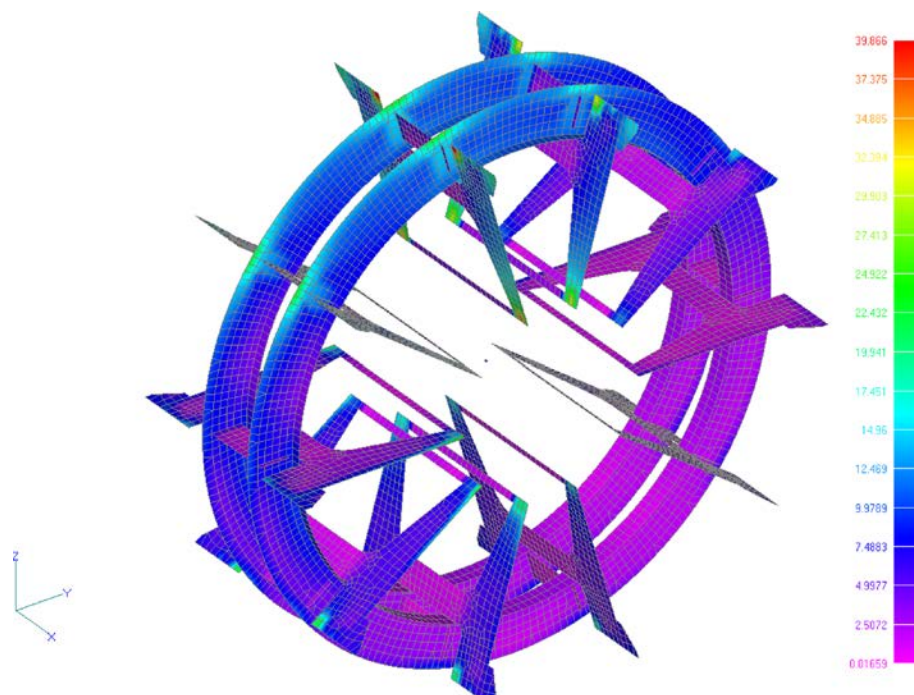


FIG. 6. Inside section of the Koepe pulley.

2.2. Results of strength analysis

Results of numerical analysis performed of the Koepe pulley components are shown in graphic form in Figs. 7–13. Figure 7 shows the distribution of reduced stress σ_z in side discs, based on the HMM hypothesis.

The largest reduced stresses in side discs, approaching 30 MPa are registered at points where they are connected to the rigid hub. Increased stress levels are also observed in the vicinity of inspection openings. Figure 8 shows the

FIG. 7. Reduced stress distribution σ_z on side discs.FIG. 8. Reduced stress distribution σ_z (Huber-von Mises) on radial and circumferential fins.

reduced stress distribution σ_z on radial and circumferential fins. The largest stress levels, approaching 40 MPa, are registered at points where they are welded to the mantle in the Koepe pulley. Further, the concentration of reduced stress (approaching 38 MPa, is registered at points where fins are connected to the hub. T-shaped circumferential fins exhibit a more uniform stress distribution over their entire area. Slight increase of stress is registered near the radial fins.

Rectangular supports fitted between the circumferential fins along the radius, just like radial fins, experience an increased stress at the point where they are welded to the circumferential fin. Figure 9 shows the reduced stress distribution on the surface of the mantle.

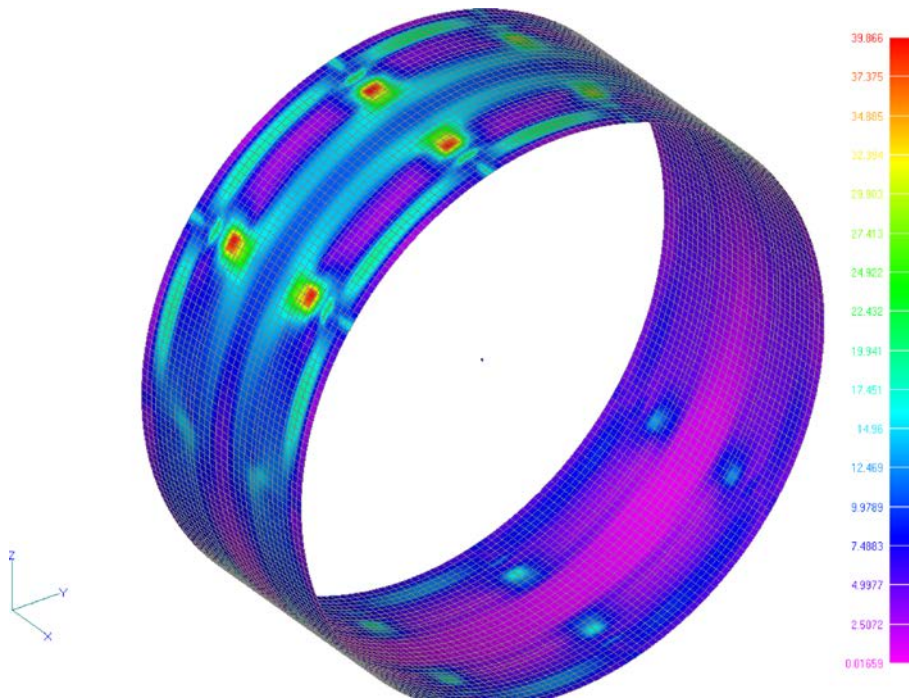


FIG. 9. Reduced stress distribution σ_z (Huber-von Mises) on the mantle's surface.

The largest stresses, approaching 40 MPa, occur at points where the mantle is connected to the radial fins. Figure 10 shows the reduced stress distribution at the point where the maximal material effort is registered on the mantle's surface during the full revolution of the Koepe pulley.

Cyclic stress increases are observed at the radial fin-mantle interface, which may cause the 'fatigue tester' effect, leading to endurance fatigue cracking.

Figure 11 shows the displacement of the pulley's mantle, the displacement pattern being re-scaled with respect to dimensions of the real construction for the sake of better visualisation. The maximal displacements, amounting to

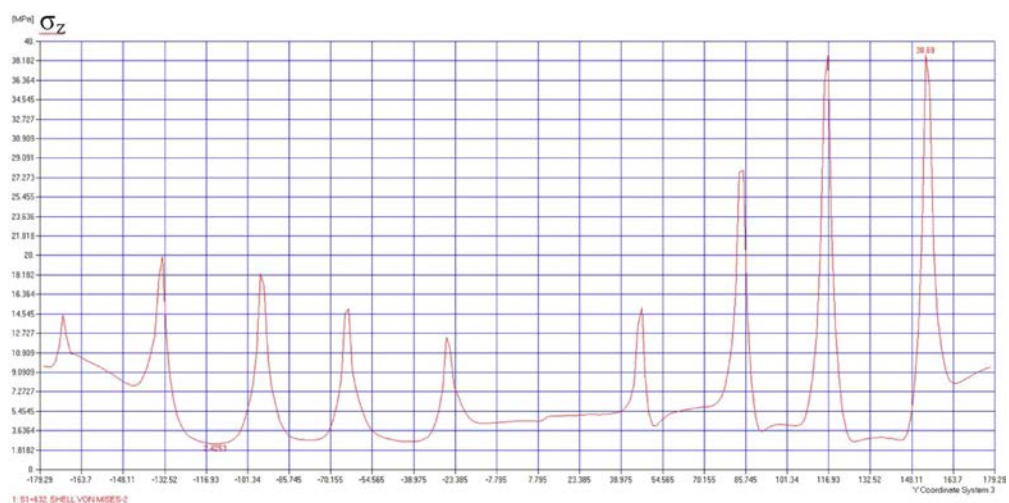


FIG. 10. Reduced stress distribution σ_z at the point where the maximal material effort is registered on the mantle's surface during the full revolution of the Koepe pulley.

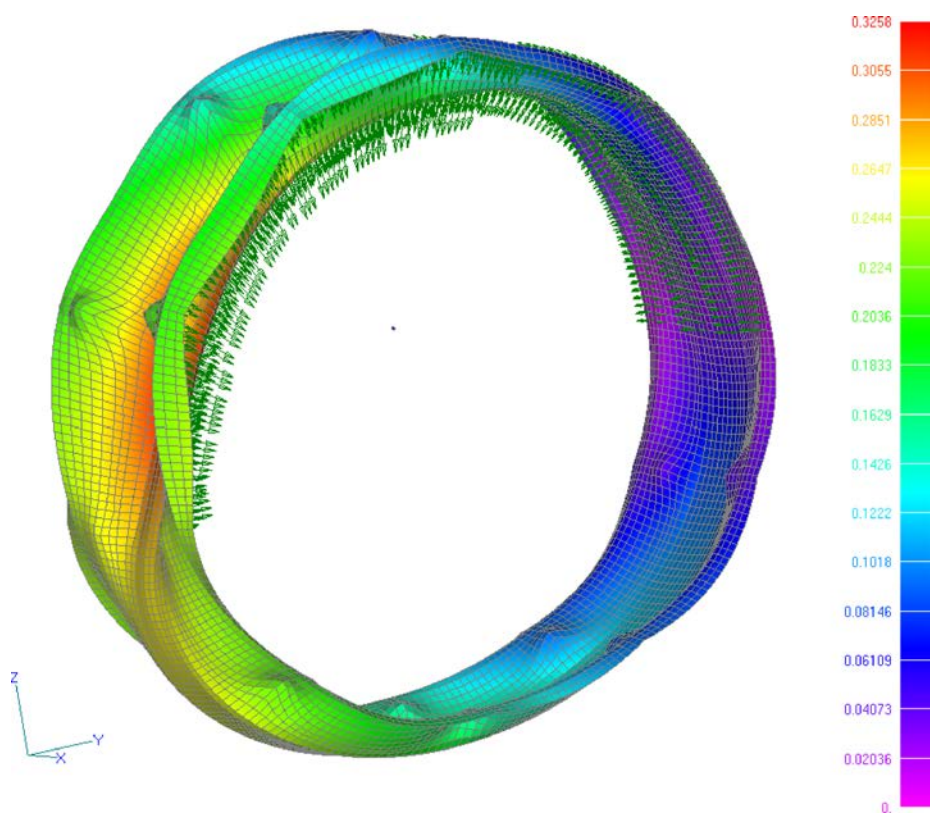


FIG. 11. Visualisation of the mantle's displacement.

0.3055 mm, are generated at points where hoisting ropes slid onto the pulley and the mantle is compressed (and pushed inwards) over the whole angle of lap. At points where no contact is maintained between the ropes and the pulley, the drum's mantle is under tension (and so it is pushed outwards the drum).

Figure 12 shows the reduced stress distribution on the hub and the drum's shaft.

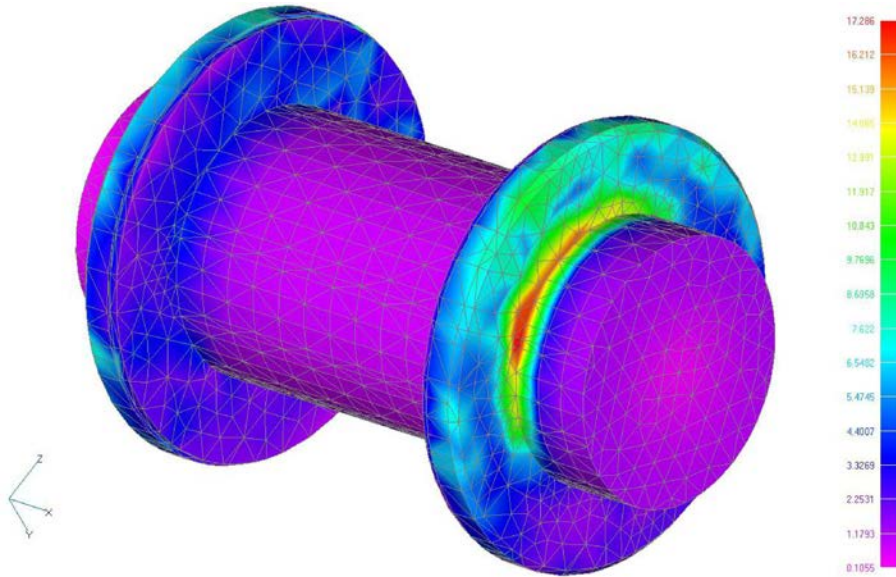


FIG. 12. Reduced stress distribution on the hub and the drum's shaft.

The maximal reduced stresses approach $\sigma_z = 17.2$ [MPa] in the shaft-hub interface region.

3. STRAIN (STRESS) MEASUREMENTS ON A REAL OBJECT

The state of strain (stress) at the points where the maximal material effort is registered in the Koepe pulley and found by the numerical methods are verified by measurements taken on a real object.

3.1. Measuring equipment

Measurements are taken with an amplifier HMB MGCplus utilising resistance or induction sensors. The bridge is supplied from gel batteries 12 V–12 Ah and the entire circuit is connected to a portable computer (laptop) supported by the professional programme “Catman” (HMB) to record the measurement data. The measurement equipment is shown in Fig. 13.



FIG. 13. Measuring equipment.

3.2. Measurement sensors (strain gauges)

Measurements are taken with two types of strain rosettes: TFxy-4/120 and TFr-8/120. Technical parameters of the strain rosette TFr-8/120 are summarised in Table 1. Strain rosettes TFxy-4/120 and TFr-8/120 are attached (glued) inside the Koepe pulley. The positions of control points (the spots where strain gauges are attached) are shown in Fig. 14.

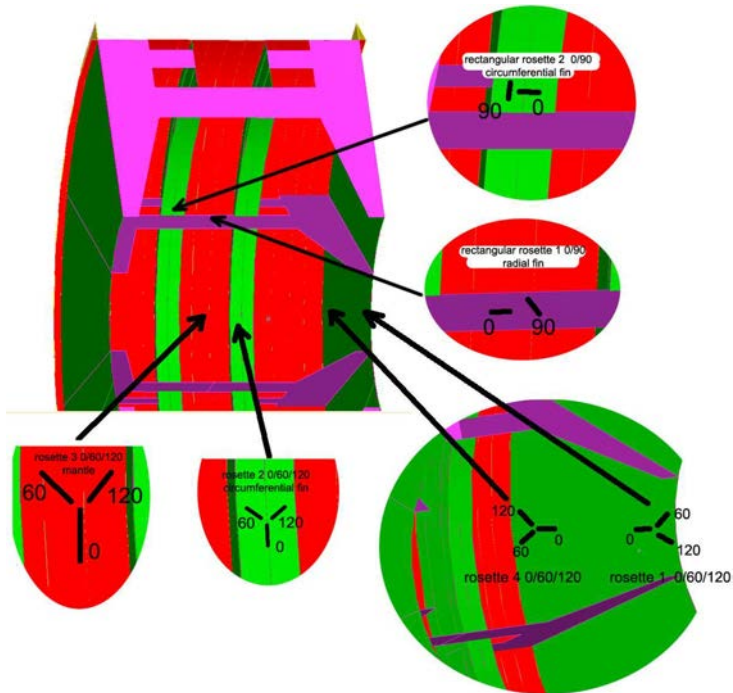


FIG. 14. Strain gauge attachment points inside the Koepe pulley.

The photo showing the location of strain sensors inside the construction of the Koepe pulley is shown in Fig. 15. The positions of strain gauges on radial and circumferential fins are shown in Fig. 16.

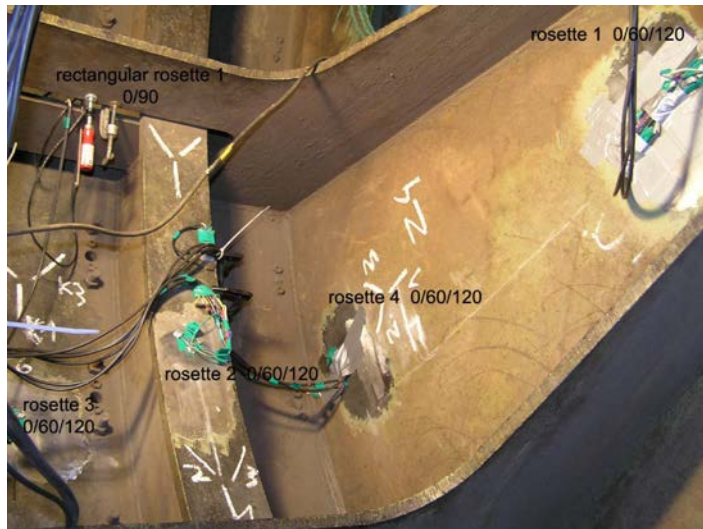


FIG. 15. Positions of strain gauges inside the Koepe pulley (photo).

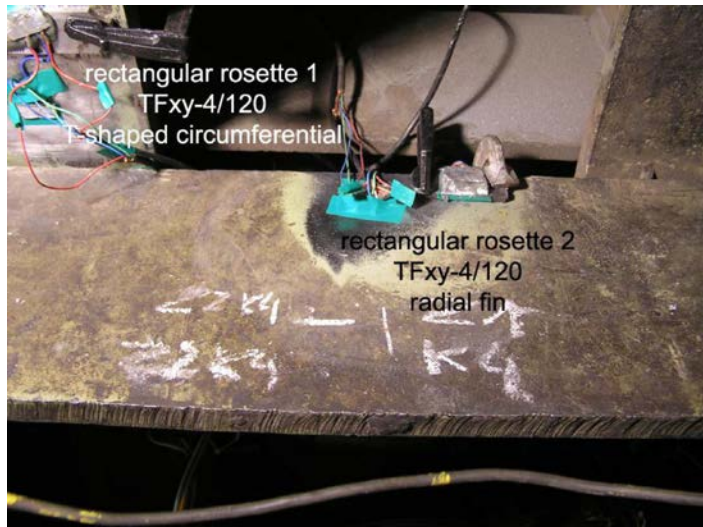


FIG. 16. Positions of strain gauges on radial and circumferential fins.

3.3. Measurement procedure

The measurement procedure uses 6 strain rosettes, including two rectangular rosettes TFxy-4/120. These rosettes have two active baselines perpendicular

to one another (0° , 90°). Each strain gauge is temperature-compensated by a compensating gauge, identical as the one used for measurements (Fig. 15 – compensating boards fixed with hand screws). The strain sensors are attached (with a glue) to:

- circumferential fins – rectangular rosette No. 1 at the distance of 5 cm from the radial fin;
- centre point of the radial fin – rectangular rosette No. 2.

Strain rosettes TFXy-4/120 register 4 measurement signals altogether.

The remaining sensors include four rosettes TFr-8/120 with baselines arranged at the angles 0° , 60° , 120° . Each strain gauge is temperature-compensated. The sensors are attached to:

- side disc – rosette No. 1 at the distance of 10 cm from the hub,
- circumferential fin – rosette No. 2 in between radial fins (the sensor is arranged such that the baseline ε_0 runs along the fin),
- the mantle in between the circumferential fins – rosette No. 3,
- side disc – at the distance of 10 cm from the drum's mantle – rosette No. 4.

Strain rosettes TFr-8/120 register 12 measurement signals altogether.

There are 16 channels from all strain gauges. The strain gauges are arranged such as to best capture the performance of vital pulley components, taking into account the variable duty cycles experienced in normal working conditions. The typical duty cycle of a hoisting installation is registered at the steady velocity $v = 16$ m/s and during the emergency braking at $v = 10$ m/s at the bottom level and half way up the shaft.

The measuring equipment is attached to the shaft inside the drum, in a special casing, to minimise the interactions of the centrifugal force. Data are recorded accordingly between particular measurement cycles, followed by assessment of the working condition of the connections and the equipment. Measurement data cover the full duty cycle of the hoisting installation, including ride down and ride up.

The strains ε_A , ε_B , ε_C along the directions $0^\circ/60^\circ/120^\circ$ being derived from the formula (3.1) [1], the directions of principal stresses σ_1 are obtained accordingly:

$$(3.1) \quad \sigma_1 = \frac{E}{3(1-\nu)} \left(\frac{\varepsilon_A + \varepsilon_B + \varepsilon_C}{3} \right) + \frac{3}{\sqrt{3}(1+\nu)} \sqrt{\frac{(2\varepsilon_A - \varepsilon_B - \varepsilon_C)^2}{3} + (\varepsilon_B + \varepsilon_C)^2}.$$

Figure 17 shows selected strain patterns registered by the strain rosette No. 2 during the full duty cycle of the hoisting installation (ride up and down), the skip travelling with the fixed velocity $v_0 = 16$ [m/s].

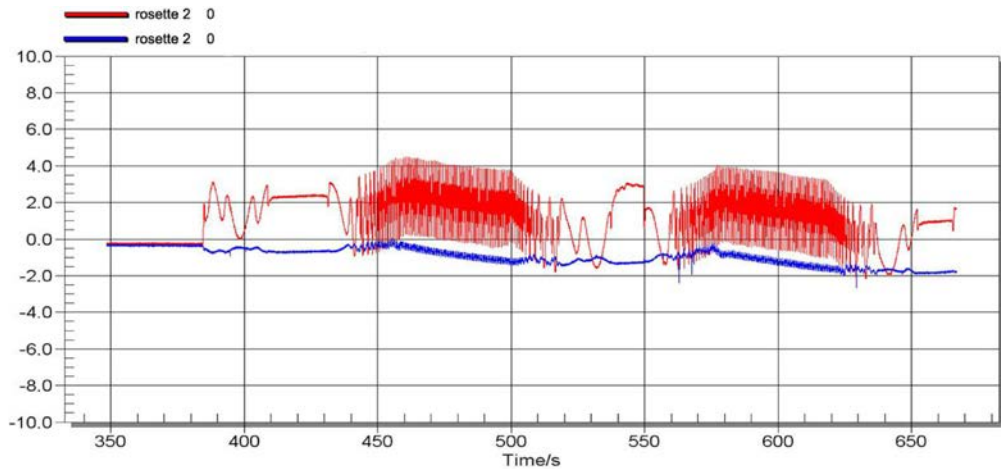


FIG. 17. Strains ε registered throughout the full duty cycle (ride down and up $v_0 = 16$ [m/s]) by the rosette No. 2 along the directions $\varepsilon_0, \varepsilon_{60}$.

Strains registered during the experiment by the strain rosette No. 1 along the directions $\varepsilon_0, \varepsilon_{60}, \varepsilon_{120}$ are shown in Fig. 18.

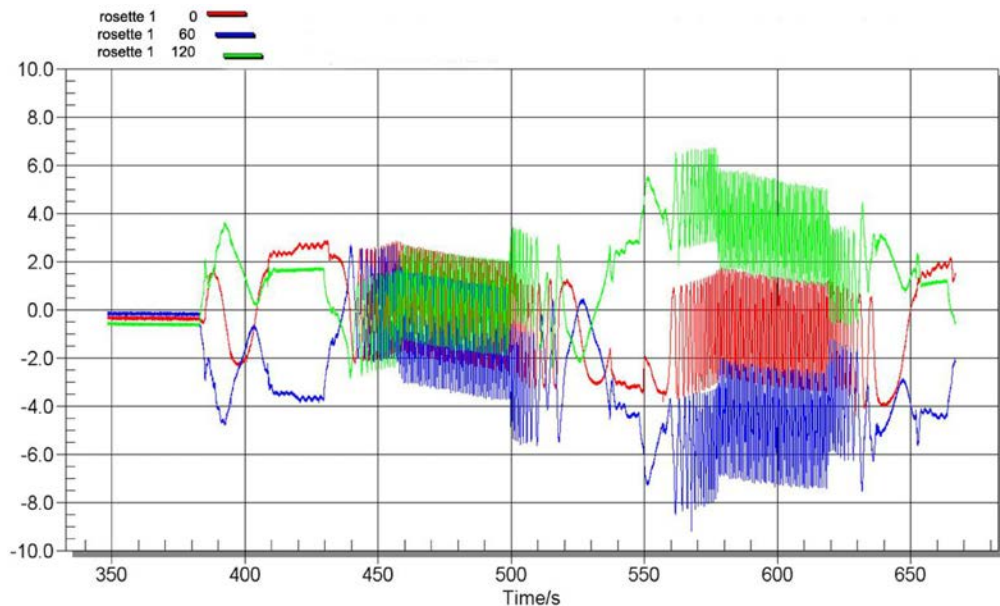


FIG. 18. Strains ε registered throughout the full duty cycle (ride down and up $v = 16$ [m/s]) by the rosette No. 1 along the directions $\varepsilon_0, \varepsilon_{60}, \varepsilon_{120}$.

Figures 19 and 20 show the measured variations of the reduced stress throughout the typical duty cycle of the hoisting installation, registered by the following strain rosettes:

- strain rosette R1 (Fig. 19),
- strain rosette Pr2 (Fig. 20).

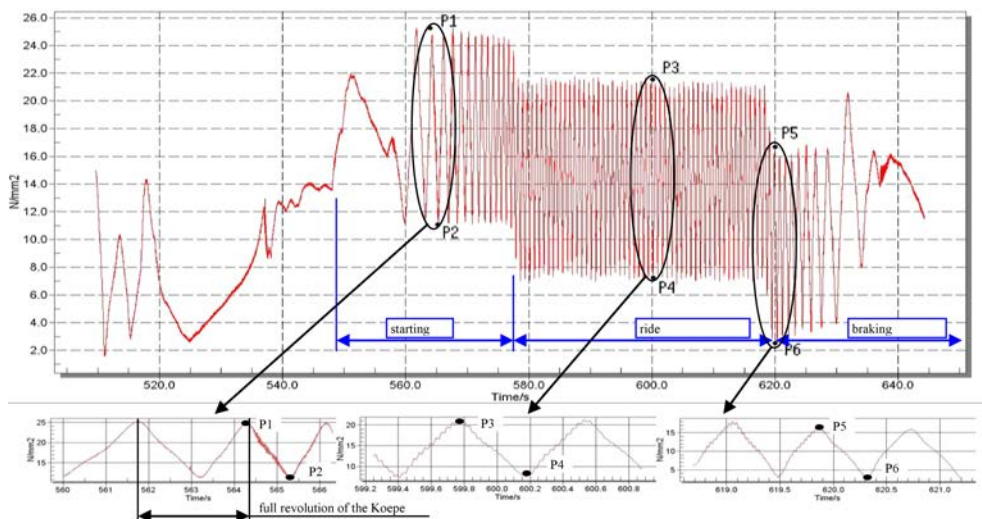


FIG. 19. Reduced stress σ_Z registered during the ride up of a fully loaded conveyance from the bottom station (strain rosette R1).

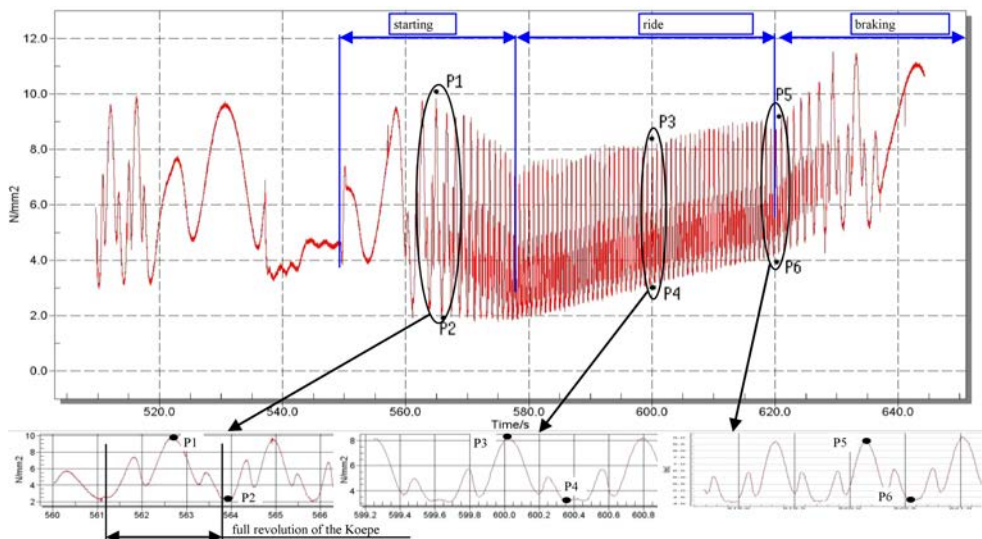


FIG. 20. Reduced stress σ_Z registered during the ride up of a fully loaded conveyance from the bottom station (strain rosette Pr2).

3.4. Numerical results and measurements taken on a real object

The adequacy of simplifying assumptions underlying the numerical analysis is verified through strain (stress) measurements taken on a real object. Reduced stresses σ_Z obtained from numerical analysis are compared with strain measurements taken on the real object, on the same points of the Koepe pulley construction (Fig. 21).

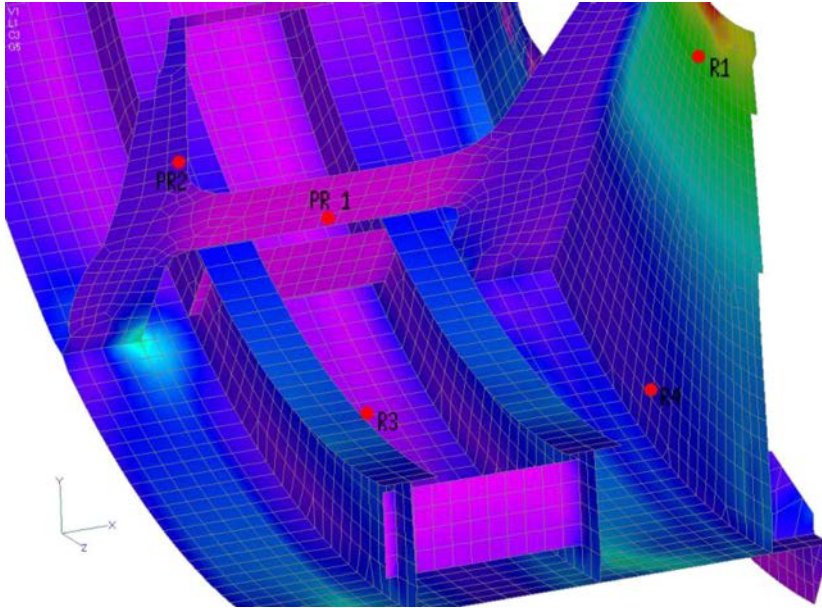


FIG. 21. Positions of readout points of reduced stress σ_Z in the numerical model (also the points where strain sensors are attached).

Amplitudes of reduced stresses obtained from the FEM analysis and from experiments on a real object are compared in Table 2. The data are registered during the ride-up of a fully loaded conveyance, moving from the bottom station with acceleration a_1 , at the selected points of the pulley construction (Fig. 21).

Table 2. Reduced stress amplitudes during the start-up of the conveyance.

Strain gauge designation	$\Delta\sigma_Z$ [MPa]	
	FEM	Experimental
R1	16	18
R3	11	12.5
R4	10	9.5
Pr1	11.82	12.0
Pr2	10.5	8.9

4. CONCLUSIONS

The numerical data agree well with measurement results, which on one hand confirms the adequacy of the assumptions underlying the strength analysis and on the other, proves the results to be reliable. Strength analyses have revealed that the stress values at nodes connecting the pulley components: circumferential fins to the mantle, the mantle with the side discs and the side discs with the hub determine the load-bearing capacity of the Koepe pulley.

Stress concentrations are mostly attributable to the presence of radial fins. If these were eliminated, those concentration points would disappear, however that cannot be done without a thorough stress analysis of Koepe pulley components to avoid the loss of stability.

REFERENCES

1. BADURA S., *Description of criterion of design of Koepe pulleys of winding gears*, AGH Kraków 2008.
2. WOLNY S., MATACHOWSKI F., *Analysis of loads and stresses in structural elements of hoisting installations in mines*, Engineering Transactions, **58**, 3–4, 153–174, 2010.
3. WOLNY S., *Dynamic loading of the pulley block in a hoisting installation in normal operating conditions*, Archives of Mining Sciences, ISSN 0860-7001, **54**, 2, 261–284, 2009.
4. WOLNY S., PŁACHNO M., *Experimental verification of bearing rope loading in typical operating conditions of the hoisting installation*, Archives of Mining Sciences, ISSN 0860-7001, **54**, 3, 531–542, 2009.

Received September 29, 2011.

Effect of Dialkyl Peroxide Blending on Tensile Properties of PLA/PBAT Polymer Alloys

Masahiro NISHIDA¹⁾, Hiroki ICHIHARA¹⁾, Hiroki WATANABE¹⁾,
Norio FUKUDA²⁾, Hiroaki ITO³⁾

¹⁾ *Nagoya Institute of Technology, Department of Mechanical Engineering*
Gokiso-cho, Showa-ku, Nagoya, Aichi, 466-8555, Japan
e-mail: nishida.masahiro@nitech.ac.jp

²⁾ *Headquarters, Aichi Center for Industry and Science Technology*
1267-1 Akiai, Yakusa-cho, Toyota-shi, Aichi, Japan

³⁾ *Industrial Research Center, Aichi Center for Industry and Science Technology*
1-157-1, Onda-cho, Kariya-shi, 448-0013 Japan

Poly(lactic acid) (PLA) and poly(butylene adipate/terephthalate) (PBAT) were used for polymer alloys, and the effects of the mixing ratio of PLA and PBAT and the addition of dialkyl peroxide (compatibilizing agent) were examined. The stress-strain curves of PLA/PBAT and PLA/PBAT/dialkyl peroxide specimens were measured using a tensile split Hopkinson bar (Kolsky Bar) method and a universal testing machine. The mixing ratio of PLA and PBAT and the dialkyl peroxide addition affected the shape of the stress-strain curve behavior. Regardless of the strain rate, the yield stress decreased and the elongation at break and strain energy increased with increasing PBAT content when the dialkyl peroxide was used. At high strain rate, the dialkyl peroxide addition increased the elongation at break and the strain energy, and changed the fracture surface to a whitened form that was markedly uneven. This result could explain the improvement in the Izod impact strength.

Key words: bioplastics, polymer alloys, strain rate effects, tensile split Hopkinson bar, fractography.

1. INTRODUCTION

The increasing use of plastic products worldwide is causing considerable damage to the environment; therefore, biodegradable plastics (plastics that can decompose in the natural environment) and bioplastics (plant-derived or recyclable-resource-based plastics) are being extensively investigated, and new biodegradable and bioplastics are continuously being developed.

Poly(lactic acid) (PLA) is a typical biodegradable bioplastic (plant-derived plastic). It has been recognized as a promising alternative material for petroleum-based plastics. In Japan, PLA is already being used to manufacture many indus-

trial products such as the interior parts of cars, parts of computer cases, and cell-phone cases. Many studies have been conducted to identify other industrial products that can be manufactured using PLA, but currently such applications are limited to machine parts that are subject to low loading. Polymer blends/alloys or natural fiber reinforcing have been required to overcome the low impact resistance and the brittleness of PLA. Because poly(butylene adipate/terephthalate) (PBAT) is a ductile and biodegradable polymer, polymer alloys of PLA and PBAT have great potential for high impact strength. For example, Fukuda, one of the authors, showed that the Izod impact strength of PLA and PBAT polymer alloys is increased when dialkyl peroxide is used [1]. Of particular note, when the mixing ratio of PLA : PBAT : dialkyl peroxide was 60 : 40 : 1, the Izod impact strength was 60 kJ/m², which is comparable to that of polycarbonate (PC).

Other than this, several attempts at the improvement of the low impact resistance and the brittleness have been conducted on PLA/PBAT blends. Jiang *et al.* investigated crystallization of the PLA component, phase morphology of the blend, mechanical properties and toughening mechanism of PLA/PBAT blends using dynamic mechanical analysis (DMA), differential scanning calorimetry (DSC), scanning electron microscopy (SEM) and an Izod impact test [2]. COLTELLI *et al.* examined the addition of acetyl tributyl citrate (ATBC) and PBAT to PLAT in order to improve tensile properties at low strain rate [3]. JIANG *et al.* studied the effects of addition of rigid nanoparticles on the tensile properties of PLA and PBAT blends [4]. YUAN *et al.* improved the compatibility of PLA with PBAT using maleic anhydride (MAH) and 2,5-dimethyl-2,5-di-(*tert*-butylperoxy) hexane (L101) [5]. SIGNORI *et al.* studied the effect of processing at high temperature on the molecular weight distribution, the morphology and the thermo-mechanical properties of PLA and PBAT polymer alloys [6]. However, there has been less work reported on the basic mechanical properties of such plastics at high strain rates.

In the present study, the stress-strain curves of PLA and PBAT polymer alloys were measured at high strain rates (600–900 s⁻¹) using a tensile split Hopkinson bar (Kolsky bar), and at low strain rate (10⁻³ s⁻¹) using a universal testing machine (A&D Co., Ltd., RTM-500). The effects of the addition of dialkyl peroxide (compatibilizing agent) and the mixing ratio of PLA and PBAT on the Young's modulus, the yield stress, the elongation at break, and fracture morphology were also examined.

2. EXPERIMENTAL METHODS

2.1. Materials

PLA and PBAT alloys were prepared using PLA from Toyota Motor Corporation (Eco-plastic S-17) and PBAT from BASF SE (Ecoflex). The mixing

S-3000NA). In the case of specimens without a compatibilizing agent, a two-phase structure consisting of the PLA matrix and PBAT particles of the same size (domain) can be observed. PBAT spherical particles of 1–3 μm diameter for PLA:PBAT = 80:20, 1–4 μm for 70:30 and 2–5 μm for 60:40 were dispersed in the PLA matrix. When the compatibilizing agent was used, PBAT particles and phase separation were not observed.

2.2. Tensile test specimens and experimental setup

Tensile test specimens were produced from the 5-mm-thick plates using a milling machine. In the case of static tests, a gage mark area of approximately 5 mm \times 5 mm and a gage length of 10 mm as shown in Fig. 3a were used. Dynamic tensile test specimens with a gage mark area of approximately 2 mm \times 2 mm and a gage length of 4 mm as shown in Fig. 3b were used. The quasi-static tests were conducted with a strain rate of 10^{-3} s^{-1} using a universal testing machine (A&D Company, Ltd., RTM-500). At high strain rates of 600 to 900 s^{-1} , the dynamic properties of the specimens were examined by the tensile split Hopkinson (Kolsky) bar test [7], as shown in Fig. 4. The input and output bars were made of stainless steel (SUS304), and their diameters and lengths were 12 mm and 2000 mm. Strain gages were applied to both sides of the input and output bars at distances of 1750 mm and 350 mm from the specimen, respectively. Because the stress histories were almost the same on both ends of the specimens, the strain and stress on the specimens were calculated

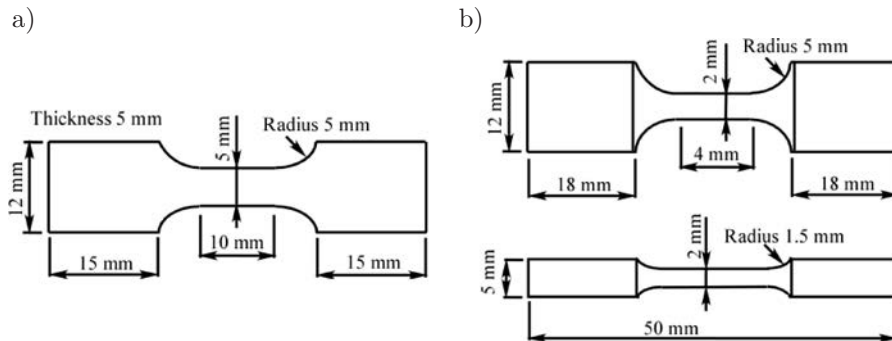


FIG. 3. Specimen shape of tensile tests: a) static tests, b) dynamic tests.

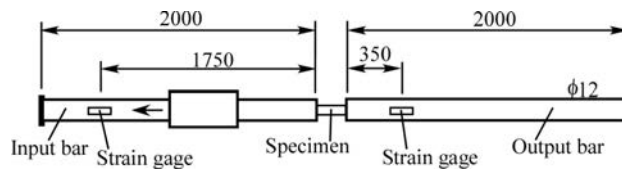


FIG. 4. Experimental set up for dynamic tensile tests.

from the strain of the bars, as measured by the strain gages, using the following equations [8, 9]:

$$(2.1) \quad \varepsilon(t) = \frac{2c_3}{L} \int_0^t [\varepsilon_I(t) - \varepsilon_T(t)] dt,$$

$$(2.2) \quad \sigma(t) = \frac{AE}{A_S} \varepsilon_T(t).$$

Here ε_I and ε_T are the axial strains induced in the input bar by the incident wave, and in the output bar by the transmitted wave, respectively. E and c_3 are Young's modulus and elastic wave velocity, respectively, of both the input and the output bars. L is the gage length. A and A_S are the cross-sectional areas of the input/output bars and specimens, respectively. Because the strain rate changed slightly during tensile loadings, it was determined using the averaged value of the strain rate-strain curve [10]. The material constants of the stainless steel (SUS304) bars used in the calculations are listed in Table 1. The specimens were preserved in a desiccator at a humidity of 30–40% until just before use in order to prevent them being affected by moisture absorption. The specimens were maintained at a temperature of $23 \pm 2^\circ\text{C}$.

Table 1. Material constants of input and output bars.

Density	$8.0 \times 10^3 \text{ kg/m}^3$
Velocity of bar wave, c_3	4970 m/s
Young's modulus, E	200 GPa

3. RESULTS AND DISCUSSION

3.1. Static tests

Figures 5a and b show the effects of PBAT content on the nominal stress-nominal strain curves at a strain rate of 10^{-3} s^{-1} using the universal testing machine. After tensile loading, the stress increased linearly with increasing strain. After showing the maximum stress, the stress decreased gradually. Cracks were observed and finally the specimens broke at the fracture point. Regardless of dialkyl peroxide addition, the maximum stress and Young's modulus decreased and the elongation at break increased with increasing PBAT content. It seems that PBAT improved the brittleness and fracture toughness of PLA. When PLA:PBAT:dialkyl peroxide = 60:40:1, the stress remained steady at approximately 25 MPa in a strain range of 0.04 to 0.11. After that, it decreased gradually.

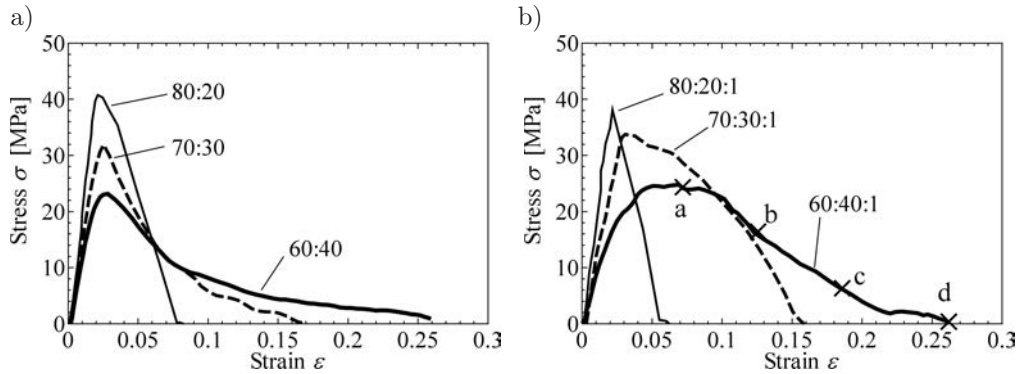


FIG. 5. Effect of PBAT content on stress-strain curve at a strain rate of 10^{-3} s^{-1} : a) without dialkyl peroxide, b) dialkyl peroxide addition.

Figure 6 shows photographs taken during deformation of the specimen when PLA:PBAT:dialkyl peroxide = 60:40:1 in Fig. 5b. The specimens of the dialkylperoxide addition continued to deform uniformly below a strain of 0.10 as shown in Fig. 6a. Necking started at a strain of 0.125, and a clear crack was observed at a strain of 0.185. After that, the specimens broke. It is a little difficult to see from this photograph, but whitened regions were observed near the cracks.

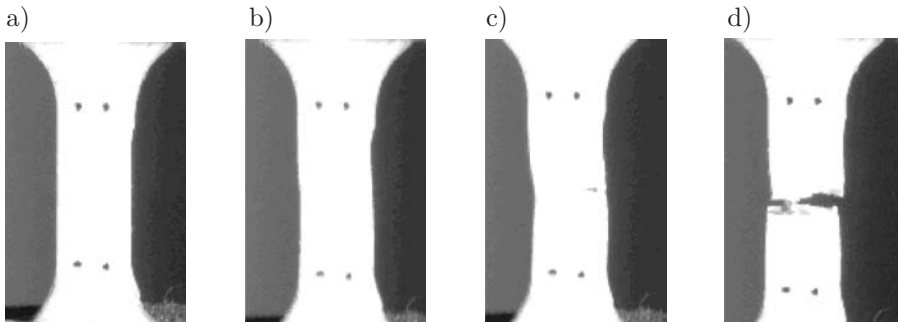


FIG. 6. Photographs of specimens when PLA:PBAT:dialkyl peroxide = 60:40:1 at a strain rate of 10^{-3} s^{-1} : a) $\varepsilon = 0.07$, b) $\varepsilon = 0.125$, c) $\varepsilon = 0.185$, d) $\varepsilon = 0.26$.

Figure 7 shows the effect of the dialkyl peroxide addition on the stress-strain curves at low strain rate. When PLA:PBAT = 70:30 and 60:40, the dialkyl peroxide addition affected the shape of the stress-strain curve, and after the maximum stress, the stress did not decrease rapidly, whereas when PLA:PBAT = 80:20, the dialkyl peroxide addition did not affect the shape of the stress-strain curve. In all cases, the dialkyl peroxide addition did not affect the Young's modulus, maximum stress or the elongation at break.

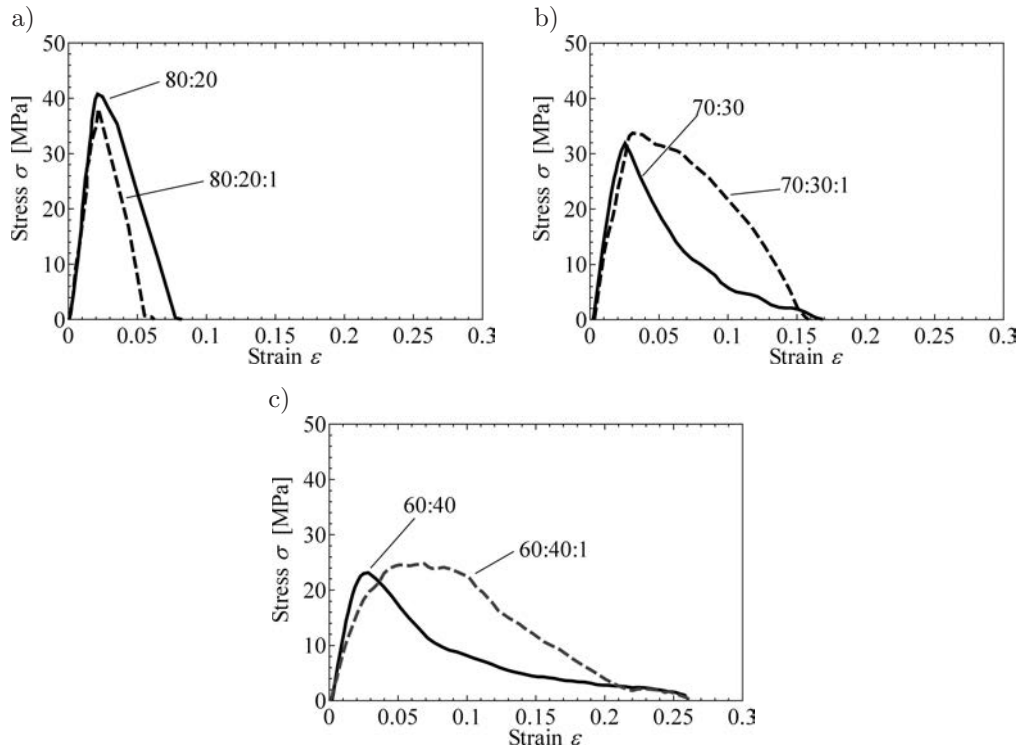


FIG. 7. Effect of dialkyl peroxide addition on stress-strain curve at low strain rate: a) 80:20 and 80:20:1, b) 70:30 and 70:30:1, c) 60:40 and 60:40:1.

3.2. Dynamic tests

Figure 8 shows the effects of PBAT content on the stress-strain curves of polymer alloy specimens obtained from the strain history and stress history using Eqs. (2.1), (2.2). When dialkyl peroxide addition was not used, the maximum

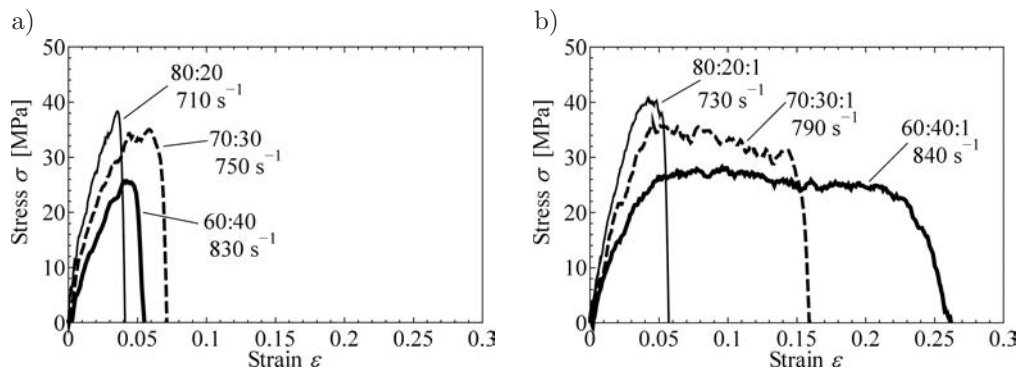


FIG. 8. Effect of PBAT content on stress-strain curve at a strain rate of 710–840 s^{-1} : a) without compatibilizing agent, b) compatibilizing agent addition.

stress and Young's modulus decreased with increasing PBAT content. However, a clear tendency for the elongation at break to occur was not observed. When dialkyl peroxide was added, the maximum stress and Young's modulus decreased and the elongation at break clearly increased with increasing PBAT content. It seems that PBAT improved the brittleness and fracture toughness of PLA only when dialkyl peroxide addition was used.

In Fig. 9, the effect of the dialkyl peroxide addition on the stress-strain curves were examined at high strain rate. When PLA:PBAT = 80:20, the dialkyl peroxide addition did not significantly affect the shape of the stress-strain curve behavior. The Young's modulus, maximum stress and elongation at break of PLA:PBAT = 80:20, were almost the same as that of PLA:PBAT:dialkyl peroxide = 80:20:1, as shown in Fig. 9a. When PLA:PBAT = 70:30, the dialkyl peroxide addition slightly increased the elongation at break. When PLA:PBAT = 60:40 as shown in Fig. 9c, the dialkyl peroxide addition significantly affected the elongation at break. As a result, when PLA:PBAT = 70:30 and 60:40, the dialkyl peroxide addition increased the strain energy, i.e. the areas under stress-strain curve before the breaking point.

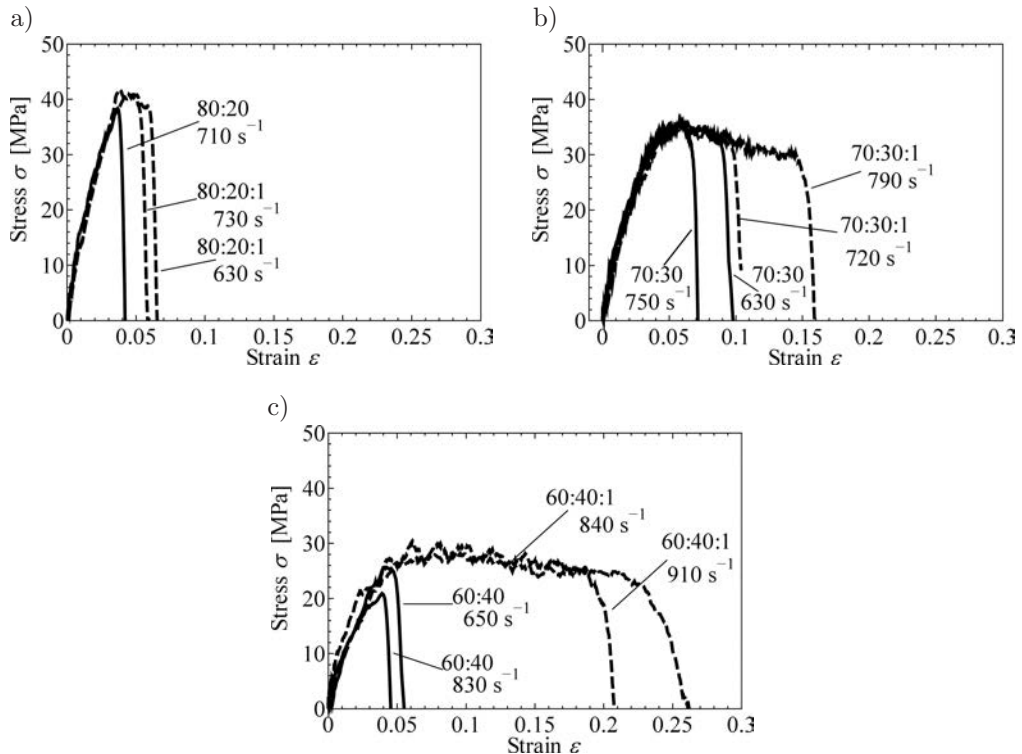


FIG. 9. Effect of dialkyl peroxide addition on stress-strain curve at high strain rate:

a) 80:20 and 80:20:1, b) 70:30 and 70:30:1, c) 60:40 and 60:40:1.

The averaged values of all results at high strain rate are shown in Fig. 10 using bar charts. The dialkyl peroxide addition did not affect the maximum stress. The dialkyl peroxide addition increased the elongation at break for each mixing ratio as discussed in the previous paragraph. The dialkyl peroxide addition increased the strain energy. The above results could explain the improvement in the Izod impact strength as shown in Fig. 11 [11]. For comparison with the re-

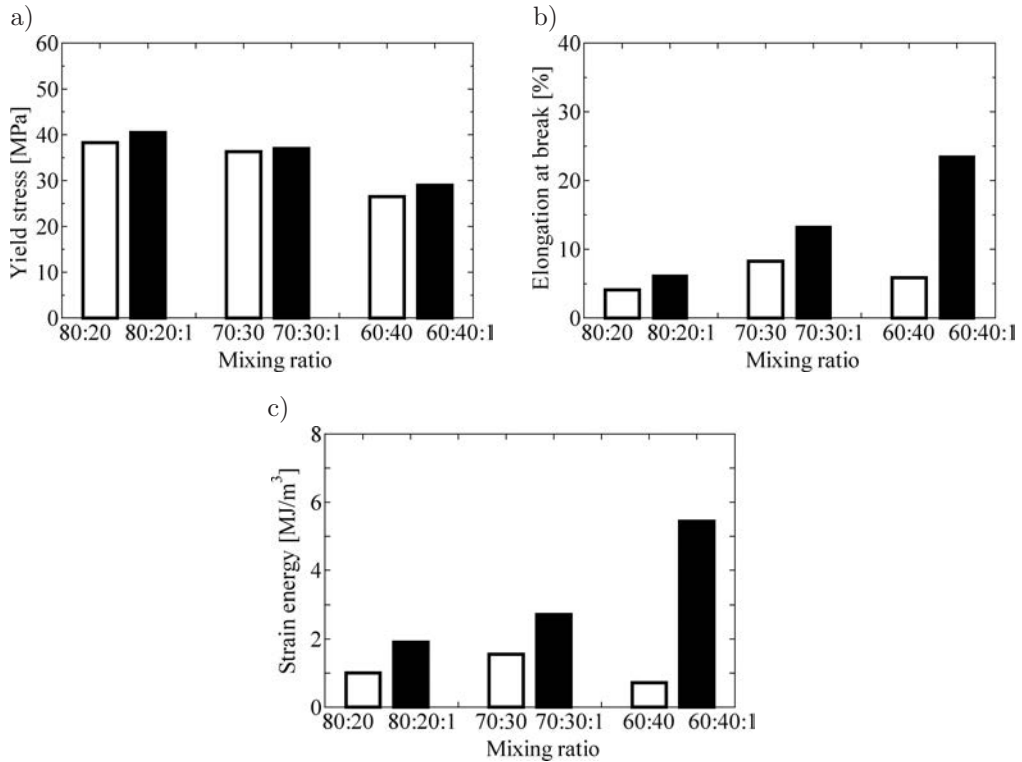


FIG. 10. Effect of PBAT content on yield stress, elongation at break and strain energy at high strain rate: a) yield stress, b) elongation at break, c) strain energy.

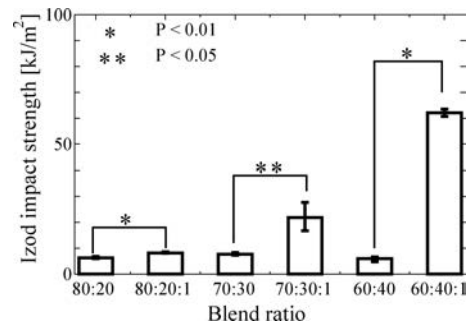


FIG. 11. Izod impact strength of PLA/PBAT alloys [11].

sults at high strain rate, the results of low strain rate are shown in Fig. 12 using bar charts. At low strain rate, the dialkyl peroxide addition did not affect the yield stress or the elongation at break. The dialkyl peroxide addition certainly increased the strain energy when $\text{PLA}:\text{PBAT} = 70:30$. However, the increased amount at low strain rate was not smaller than that at high strain rate. From these results, it was found that the dialkyl peroxide addition was effective in increasing the Izod impact strength.

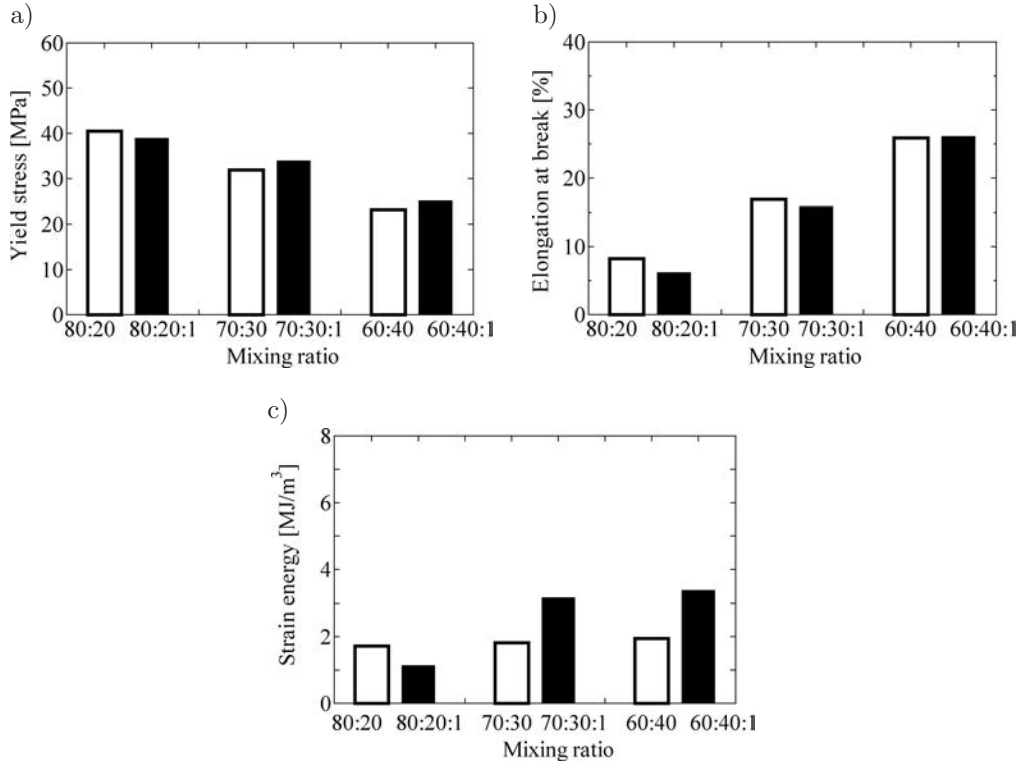


FIG. 12. Effect of PBAT content on yield stress, elongation at break and strain energy at low strain rate: a) yield stress, b) elongation at break, c) strain energy.

3.3. Observation of fracture surfaces

Because the effect of dialkyl peroxide addition on the dynamic properties of polymer blends was pronounced when $\text{PLA}:\text{PBAT} = 60:40$, the fracture surfaces of specimens were observed when $\text{PLA}:\text{PBAT} = 60:40$ and $\text{PLA}:\text{PBAT}:\text{dialkyl peroxide} = 60:40:1$. Figure 13 shows photographs of the fracture surface after dynamic tensile tests. When $\text{PLA}:\text{PBAT} = 60:40$, the fracture surface was flat and smooth, and was perpendicular to the applied stress. It appeared that a brittle fracture had occurred. When $\text{PLA}:\text{PBAT}:\text{dialkyl peroxide} = 60:40:1$,

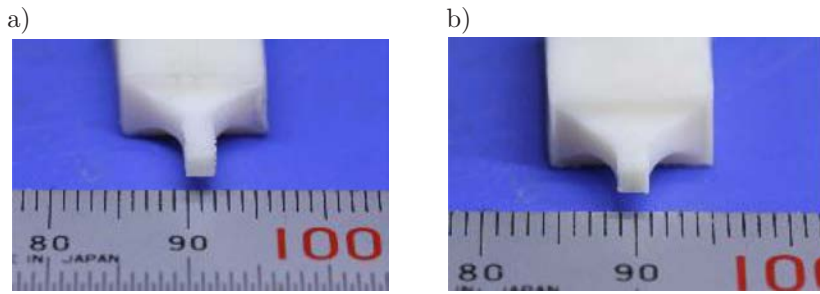


FIG. 13. Fracture surface after dynamic tensile test: a) PLA : PBAT = 60 : 40,
b) PLA : PBAT : dialkyl peroxide = 60 : 40 : 1.

a slightly whitened and markedly uneven fracture surface was observed. The dialkyl peroxide addition caused a ductile fracture surface.

Figure 14 shows magnified images of the fracture surfaces in Fig. 13. Many holes of several hundred micrometers in diameter could be observed on the fracture surface of the specimens without the dialkyl peroxide. When the dialkyl peroxide was used, such holes were not observed. The formation mechanism for these holes is still unclear, and more detailed investigation is required. Figure 15

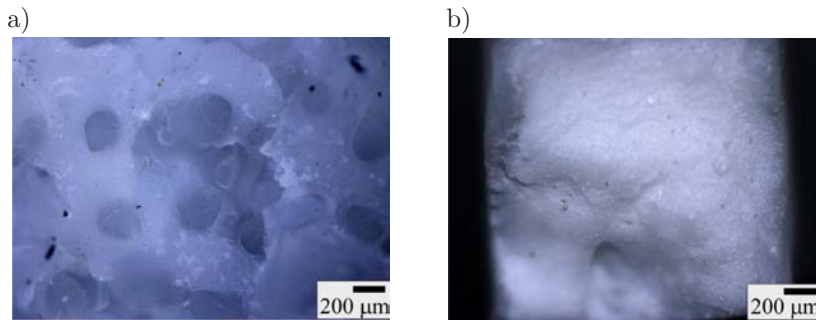


FIG. 14. Enlarged images of Fig. 13: a) PLA : PBAT = 60 : 40,
b) PLA : PBAT : dialkyl peroxide = 60 : 40 : 1.

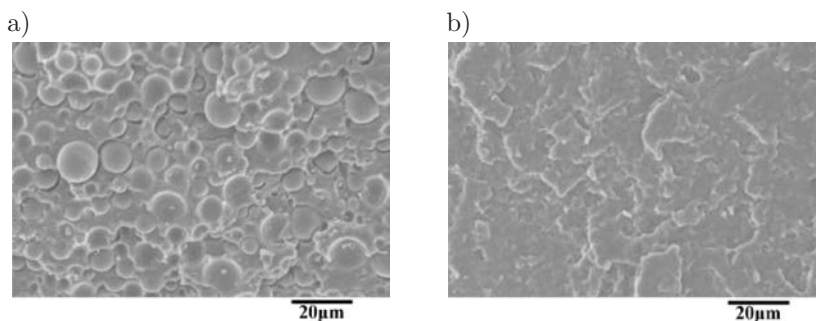


FIG. 15. Fracture surfaces captured by SEM: a) PLA : PBAT = 60 : 40,
b) PLA : PBAT : dialkyl peroxide = 60 : 40 : 1.

shows photographs of the fracture surfaces captured by the SEM. The tensile fracture surfaces at high strain rates were almost the same as the fracture surfaces after cooling using liquid nitrogen, as seen in Fig. 2. On this level, the fracture surfaces had no distinctive features. Distinctive fracture surfaces could be observed at the optical microscope level.

Figure 16 shows the fracture surface of specimens after the Izod impact tests shown in Fig. 11 [11]. Figures 16(a-1) and (b-1) show that the fracture surface

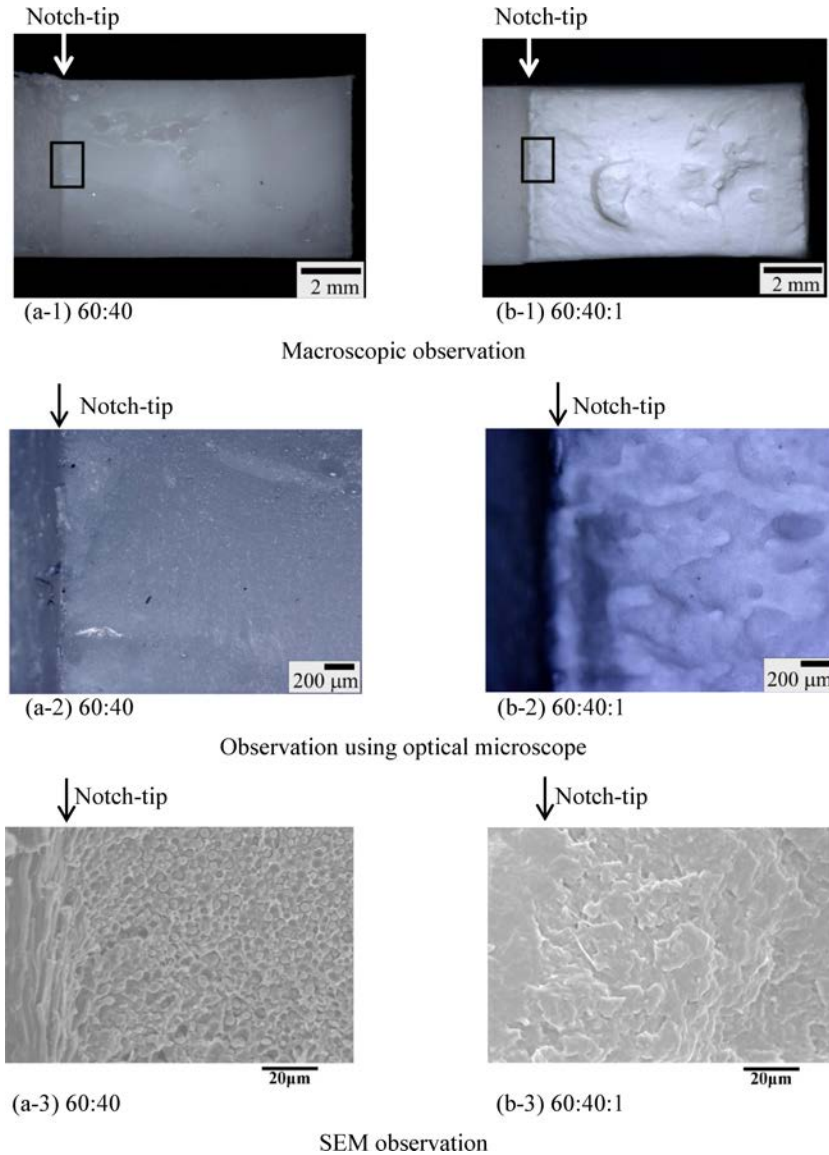


FIG. 16. Fracture surfaces after Izod impact test.

was flat and smooth when PLA:PBAT = 60:40, whereas a slightly whitened and markedly uneven fracture surface was observed when PLA:PBAT:dialkyl peroxide = 60:40:1. Optical microscope photographs in Fig. 16(a-2) and (b-2) show that there are no holes even when PLA:PBAT = 60:40, unlike the fracture surface of the dynamic tensile test sample, which has many holes. SEM photographs show that the fracture surfaces were almost the same as the fracture surfaces after cooling using liquid nitrogen as seen in Fig. 2, similar to the results of the tensile fracture surfaces at high strain rate.

4. CONCLUSIONS

The stress-strain curves of PLA/PBAT and PLA/PBAT/dialkyl peroxide specimens were measured using a tensile split Hopkinson bar method and a universal testing machine. Only in the dynamic tensile test did the dialkyl peroxide addition increase the elongation at break and change the fracture surface to a whitened form that was markedly uneven. When dialkyl peroxide was added, the elongation at break increased with increasing PBAT content. When PLA:PBAT = 70:30 and 60:40, the dialkyl peroxide increased the areas under stress-strain curve before the breaking point. It seems that the dialkyl peroxide addition caused a ductile fracture surface. This result could explain the improvement in the Izod impact strength. In order to clarify the main reason for this the degree of cross-linking should be measured.

ACKNOWLEDGMENT

The authors are greatly indebted to Dr. K. Ogawa of the Space Dynamics Laboratory in Japan for his valuable advice with respect to the tensile split Hopkinson bar.

REFERENCES

1. FUKUDA N., MATSUBARA H., KITAGAWA R., *The crystallization behaviors and mechanical properties of poly(lactic acid)/poly(butylenes adipate terephthalate) alloys* [in Japanese], Proceedings of 59th Symposium on Macromolecules, 5657–5658, 2007.
2. JIANG L., WOLCOTT M.P., ZHANG J., *Study of biodegradable polylactide/poly(butylenes adipate-co-terephthalate) blends*, *Biomacromolecules*, **7**, 199–207, 2006.
3. COLTELLI M.-B., MAGGIORE I.D., BERTOLDO M., SIGNORI F., BRONCO S., CIARDELLI F., *Poly(lactic acid) properties as a consequence of poly(butylene adipate-co-terephthalate) blending and acetyl tributyl citrate plasticization*, *Journal of Applied Polymer Science*, **110**, 1250–1262, 2008.

4. JIANG L., LIU B., ZHANG J., *Properties of poly(lactic acid)/poly(butylene adipate-co-terephthalate)/nanoparticle ternary composites*, Ind. Eng. Chem. Res., **48**, 7594–7602, 2009.
5. YUAN H., LIU Z., REN J., *Preparation, characterization, and foaming behavior of poly(lactic acid)/poly(butylene adipate-co-butylene terephthalate) blend*, Polymer Engineering & Science, **49**, 5, 1004–1012, 2009.
6. SIGNORI F., COLTELLI M.-B., BRONCO S., *Thermal degradation of poly(lactic acid) (PLA) and poly (butylenes adipate-co-terephthalate) (PBAT) and their blends upon melt processing*, Polymer Degradation and Stability, **94**, 1, 74–82, 2009.
7. OGAWA K., *Impact tensile characteristics of 6061-T6 aluminum alloy* [in Japanese], Journal of Japan Institute of Light Metals, **51**, 175–181, 2001.
8. GRAY III G.T., *Classic split Hopkinson pressure bar testing*, ASM Handbook, Vol. 8, Mechanical Testing and Evaluation, 462–476, 2000.
9. CHEN W., SONG B., *Split Hopkinson (Kolsky) Bar: Design, Testing and Applications*, Springer, 2010.
10. NAKAI K., YOKOYAMA T., *Strain rate dependence of compressive stress-strain loops of several polymers*, Journal of Solid Mechanics and Materials Engineering, **2**, 4, 557–566, 2008.
11. NISHIDA M., ICHIHARA H., FUKUDA N., *Evaluation of dynamic compressive properties of PLA/PBAT polymer alloys using split Hopkinson pressure bar method*, Engineering Transactions, **59**, 1, 23–30, 2011.

Received October 5, 2011.

DIRECTIONS FOR THE AUTHORS

The periodical *ENGINEERING TRANSACTIONS (ROZPRAWY INŻYNIERSKIE)* presents original papers which should not be published elsewhere.

As a rule, the volume of a paper should not exceed 40 000 typographic signs. The following directions are particularly important:

1. **The paper submitted for publication should be written in English.**
2. The title of the paper should be as short as possible. The text should be preceded by a brief introduction; it is also desirable that a list of notations used in the paper should be given.
3. Short papers should be divided into section and subsection, long papers into sections, subsections and points. Each section, subsection or point must bear a title.
4. The formula number consists of two figures: the first represents the section number and the other the formula number in that section. Thus the division into subsections does not influence the numbering of formulae. Only such formulae should be numbered to which the author refers throughout the paper. This also applies to the resulting formulae. The formula number should be written on the left-hand side of the formula; round brackets are necessary to avoid any misunderstanding. For instance, if the author refers to the third formula of the set (2.1), a subscript should be added to denote the formula, viz. (2.1)₃.
5. All the notations should be written very distinctly. Special care must be taken to distinguish between small and capital letters as precisely as possible. Semi-bold type must be underlined in black pencil. Explanations should be given on the margin of the manuscript in case of special type face.
6. Vectors are to be denoted by semi-bold type, transforms of the corresponding functions by tildes symbols. Trigonometric functions are denoted by sin, cos, tan and cot, inverse functions – by arcsin, arccos, arctan and arccot; hyperbolic functions are denoted by sh, ch, th and cth, inverse functions – by Arsh, Arch, Arth and Archth.
7. The figures in square brackets denote reference titles. Items appearing in the reference list should include the initials of the first name of the author and his surname, also the full of the paper (in the language of the original paper); moreover;
 - a) In the case of books, the publisher's name, the place and year of publication should be given, e.g., 5. ZIEMBA S., *Vibration analysis*, PWN, Warszawa 1970;
 - b) In the case of a periodical, the full title of the periodical, consecutive volume number, current issue number, pp. from ... to ..., year of publication should be mentioned; the annual volume number must be marked in semi-bold type as to distinguish it from the current issue number, e.g., 6. SOKOŁOWSKI M., *A thermoelastic problem for a strip with discontinuous boundary conditions*, Arch. Mech., **13**, 3, 337–354, 1961.
8. The authors should enclose a summary of the paper. The volume of the summary is to be about 100 words, also key words are requested.
9. The preferable format for the source file is TeX or LaTeX while MS Word is also acceptable. Separate files for the figures should be provided in one of the following formats: EPS or PostScript (preferable), PDF, TIFF, JPEG, BMP, of at least 300 DPI resolution. The figures should be in principle in gray-scale and only if necessary the color will be accepted.

Upon receipt of the paper, the Editorial Office forwards it to the reviewer. His opinion is the basis for the Editorial Committee to determine whether the paper can be accepted for publication or not.

Once the paper is printed, the issue of Engineering Transactions free of charge is sent to the author. Also the PDF file of the paper is forwarded by the e-mail to the authors.

Editorial Committee
ENGINEERING TRANSACTIONS